Master thesis

GAS HYDRATE STABILITY AND DISTRIBUTION IN THE FJORDS OF WESTERN SPITSBERGEN, SVALBARD ARCHIPELAGO

An assessment based on indirect hydrate indicators

Nil Rodés i Llorens

Master Program Polar and Marine Sciences (POMOR)

September 2021

pomor MASTER PROGRAM for polar and marine sciences

St. Petersburg University

Universität Hamburg
DER FORSCHUNG | DER LEHRE | DER BILDUNG

UNIS The University Centre in Svalbard

Universität Bremen

marum

Master thesis

GAS HYDRATE STABILITY AND DISTRIBUTION IN THE FJORDS OF WESTERN SPITSBERGEN, SVALBARD ARCHIPELAGO
An assessment based on indirect hydrate indicators

05.04.06 Ecology and environmental management
BM.5527.2019 Master Program for Polar and Marine Science (POMOR)

Saint Petersburg State University
Hamburg University

in collaboration with:
Bremen University
The University Centre in Svalbard

Nil Rodés i Llorens

Bremen, 3rd of September 2021

Table of contents

Abstract (in English)

GAS HYDRATE STABILITY AND DISTRIBUTION IN THE FJORDS OF WESTERN SPITSBERGEN, SVALBARD ARCHIPELAGO. An assessment based on indirect hydrate indicators

Nil Rodés i Llorens

Master Program Polar and Marine Sciences POMOR / 050406 Ecology and environmental management

Supervisors:
Prof. Dr. Gerhard Bohrmann, Universität Bremen
Dr. Miriam Römer, Universität Bremen; MARUM - Center for Marine Environmental Sciences
Dr. Kim Senger, The University Centre in Svalbard
Peter Betlem, The University Centre in Svalbard; University of Oslo
Dr. Alexey Krylov, Saint Petersburg State University; VNIIOOkeangeologia

This study evaluates the spatial and temporal variability of seepage detected in the main fjords of western Spitsbergen, Svalbard archipelago, as indirect hydrate indicators (geophysical attributes to the presence of gas or seepage) of the natural gas hydrate (NGH) distribution. While methane seepage and NGH distribution in the offshore provinces of Vestnesa Ridge on the continental slope west of Svalbard and Prins Karls Forland are extensively studied, their potential distribution in the Isfjorden and Van Mijenfjorden fjords is poorly constrained. 2D seismic interpretation enabled mapping the major stratigraphic units and structural elements of the fjords and further identifying the distribution of potential source rocks. We also recognized different migration pathways such as faults and igneous intrusions, presumably transporting the gas to the seabed. In addition, analysis of hydrographic datasets acquired in August 2015 and June 2021 allowed the quantification and description of gas flares in the fjords and the comparison of the gas system characteristics over the late spring and early autumn seasons. Overall, 796 flares (668 in Isfjorden and 115 in Van Mijenfjorden) have been identified in the echograms acquired in 2015, and 152 flares have been identified in Isfjorden in 2021. The observations revealed an active fluid flow system in the fjords with an evident spatio-temporal variability of the seepage. Furthermore, different morphologic expressions at the seafloor, such

as pockmarks, have been spatially correlated with the flares, unveiling no direct association with the present-day seepage. Despite the achievements of this work, further efforts are needed to finally prove the presence of NGH in the fjords of the Svalbard archipelago. Besides, more work is needed to understand the relation between high flare activity areas and the atmospheric methane concentration anomalies to assess potential methane efflux (diffusion between the surface waters and the atmosphere), contributing to the atmospheric carbon pool.

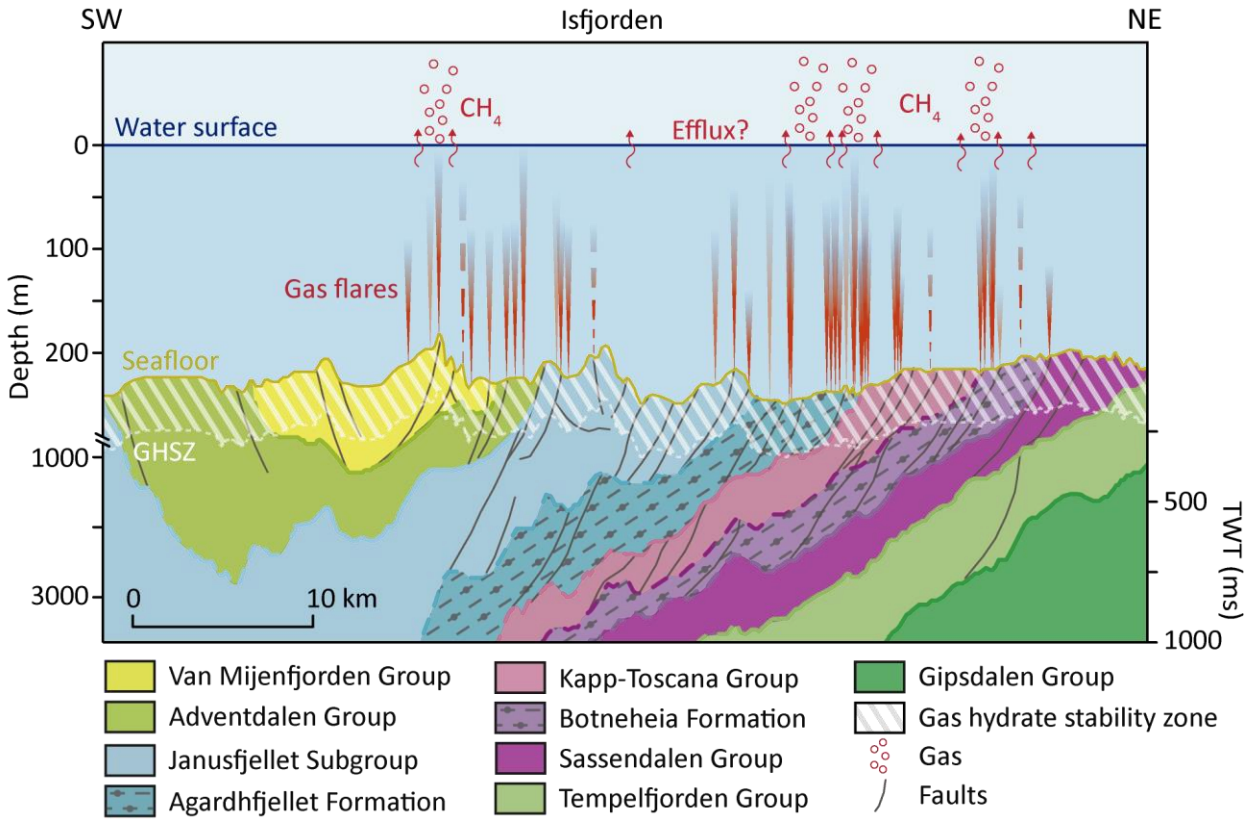

Graphical abstract. Conceptual model of the fluid flow system in Isfjorden from the source rocks to the atmosphere. It shows the major stratigraphical features presumably transporting the gas to the seafloor, which is further detected as acoustic flares in the water column. Potential efflux remains uncertain.

Keywords: Gas seepage, flares, hydrocarbon sources, hydroacoustic mapping, natural gas hydrates, Arctic fjord systems, Svalbard archipelago.

Abstract (in Russian)

Стабильность газовых гидратов и их распределение в фьордах Западного Шпицбергена: оценка по косвенным признакам.

Нил Родес и Льоренс

Магистерская программа «Полярные и морские исследования (ПОМОР)»/050406

«Экология и природопользование»

Научные руководители:

Профессор Герхард Борман, Бременский Университет

Д-р Мириам Ромер, Бременский Университет, МАРУМ – центр наук о морских обстановках

Д-р Ким Сенгер, Университетский центр Шпицбергена

Петер Бетлем, Университетский центр Шпицбергена; Университет Осло

Доцент, к.-г.м.н. Алексей Алексеевич Крылов, СПбГУ, Институт наук о Земле

В работе оценена пространственная и временная изменчивость сипинга, являющегося косвенным индикатором присутствия природных газовых гидратов (геофизические признаки присутствия газа или сипинга), в основных фьордах западного Шпицбергена,. Несмотря на то, что метановый сипинг и распространение субмаринных газовых гидратов в окрестностях хребта Вестнеса на континентальном склоне к западу от Шпицбергена и Земли Принца Карла активно изучаются, их потенциальное наличие в Исфьорде и Ван-Миджен-фьорде практически не исследовано. Результаты интерпретации 2D-сейсмических данных позволили нанести на карту основные стратиграфические единицы и структурные элементы фьордов, а также определить распределение потенциальных нефтегазоматеринских пород. Мы также обнаружили различные пути миграции, такие как разломы и вулканические интрузии, предположительно переносящие газ на морское дно. Кроме того, анализ гидрографических данных, полученных в августе 2015 г. и в июне 2021 г., позволил количественно оценить и описать газовые факелы во фьордах и сравнить характеристики газовой системы в конце весеннего и раннего осеннего сезонов. В целом на эхограммах, полученных в 2015 г., было зарегистрировано 796 газовых факелов (668 в

Ис-фьорде и 115 в Ван-Миджен-фьорде), а в 2021 г. в пределах Исфьорда – 152 факела. Наблюдения выявили активную систему миграции флюидов во фьордах с очевидной пространственно-временной изменчивостью сипинга. Более того, различные морфологические проявления на морском дне, такие как покмарки, были пространственно сопоставлены с факелами; прямой связи с современным сипингом не было обнаружено. В дополнение к результатам данной работы необходимы дальнейшие усилия, чтобы окончательно доказать присутствие газовых гидратов во фьордах архипелага Шпицберген. Кроме того, необходимы дополнительные исследования, чтобы понять связь между областями с высокой активностью газовых факелов и аномалиями концентраций метана в атмосфере, что позволит оценить потенциальный отток метана (диффузия между поверхностными водами и атмосферой), способствующий накоплению углерода в атмосфере.

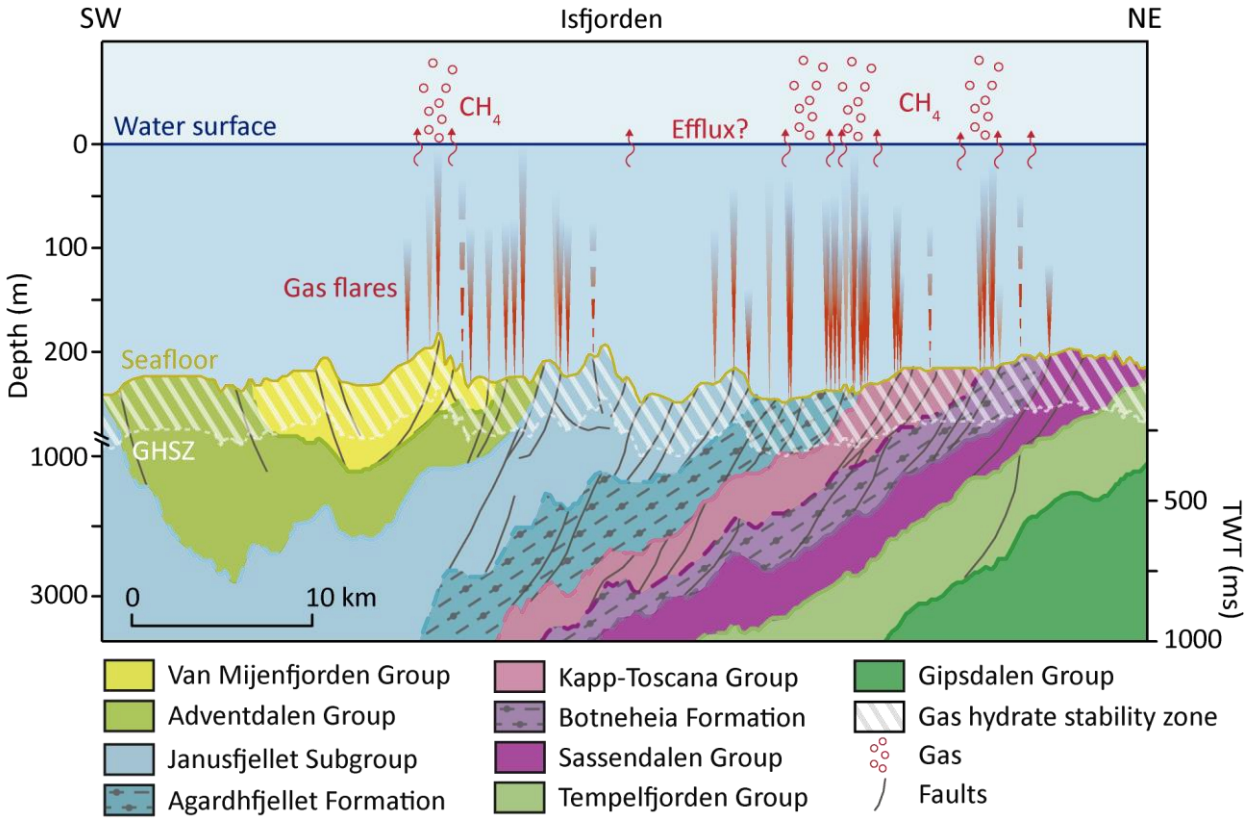

Графический реферат. Концептуальная модель системы движения флюидов в Ис-фьорде от нефтегазоматеринских пород к атмосфере. На нем показаны основные стратиграфические подразделения, предположительно переносящие газ в сторону морского дна, что в дальнейшем обнаруживается как акустические факелы в водной толще. Величина возможного оттока газа в атмосферу остается неизвестной.

Ключевые слова: газовый сипинг, газовые факелы, источники углеводородов, гидроакустическое картирование, гидраты природного газа, системы арктических фьордов, архипелаг Шпицберген.

1. INTRODUCTION

The discovery of numerous gas flares seeping in the fjords of western Spitsbergen, Svalbard archipelago (Figure 1), is of great interest in a moment of accelerated warming in the waters of the fjords (Skogseth et al., 2020) and the Arctic as a whole. Understanding the origin and composition of the gas is crucial for assessing the present-day and future impact of the seepage in near-shore settings of the Arctic, which is globally distinguished as an early climate change warning system. The gas seeping in the shallow waters of the fjords could reach the atmosphere contributing to the atmospheric carbon pool, increasing the Arctic amplification and global warming (Shindell et al., 2009; Betlem et al., 2021).

Gas seepage may be indicative of temporal destabilization of near-bottom agglomerations of natural gas hydrates (NGH) in near-shore settings in the Arctic (Salomatin et al., 2010). NGH are ice-like crystalline solids composed of water and light molecular weight gas, commonly methane (CH_4). Their formation and stability require high pressure, low temperature and sufficient gas supply to oversaturate the surrounding and overlaying pore water (Kvenvolden, 1993). Thermobaric modeling results predict NGH occurrence onshore Svalbard (Betlem et al., 2019; Minshull et al., 2020) and in Isfjorden, the major fjord system of Spitsbergen (Roy et al., 2012, Betlem et al., 2021) (Figure 1, A). However, NGHs have not been discovered in the Svalbard archipelago yet, and overall, near-shore NGH potential in the fjords is poorly constrained.

The geology of Svalbard presents thick sedimentary units comprising both source and reservoir rocks along with surface oil and gas seeps. Although there are no commercial petroleum discoveries in the archipelago, many gas (predominantly methane) discoveries in measurable quantities have been made associated with Late Palaeozoic-Mesozoic successions (Senger et al., 2019). The organic-rich Botneheia Formation (Middle Triassic) and the organic-rich Agardhfjellet Formation (Upper Jurassic) present a gas-prone source in central Spitsbergen, which progressively turns into the oil maturation window in east Spitsbergen and Edgeøya (Koevoets et al., 2016, 2018; Senger et al., 2019; Birchall et al., 2021).

Decadal water column thermal trends indicate heat transfer into the fjord waters of the archipelago, raising the water temperature. In Isfjorden, the heat transfer is linked to an increase in mean fjord water temperatures of 0.7°C in winter and 0.6°C in the summer season (Skogseth et al., 2020). This temperature rise could result in sub-sea thawing of permafrost (Betlem et al.,

2021) and gas hydrates dissociation (Shakhova et al., 2010, Mienert et al., 2005), causing additional methane release into the water column.

Multiple sub-cropping thrust faults outcrop in the main trunk of Isfjorden, which could serve as migration pathways for fluids and gas (Roy et al., 2014). Seabed morphologies are recordable indicators associated with fluids -such as methane gas- escape through the seafloor, evidencing the presence of an underlying conventional petroleum system. In Isfjorden, over 1300 individual pockmarks have been described (Roy et al., 2015), which could be signs of methane seepage from the seabed into the water column, serving as a potential piece of evidence for hydrate occurrence (Minshull et al., 2020).

Gas can escape the sediment by diffusion in pore water and sediment systems or via seepage forming flares when oversaturated. The assessment of gas flares characteristics and distribution can be used as easily recordable prospecting indicators of near-bottom agglomerations of NGH (Salomatin et al., 2010). Therefore, the occurrence of active gas seeps may be indicative of a temporal destabilization of the temperature-dependent gas hydrate stability zone (GHSZ), using its distribution as an evaluation tool for the near-shore NGH distribution in the Svalbard fjords.

Very few gas flares reach the water surface, and even for these, it is probable that nitrogen and other gases would have largely replaced methane in the bubbles during their ascent over the water column (Westbrook et al., 2009). Still, it is estimated that worldwide, about 10 Tg CH_4 yr^{-1} could transfer to the atmosphere by diffusion (Kvenvolden and Rogers, 2005), and in shallow areas such as fjords, the CH_4 released from the seafloor has a greater potential to reach the atmosphere (Hovland et al., 1993, McGinnis et al., 2006).

Methane emissions are of great importance since it is a powerful greenhouse gas. When averaged over a 100-year timescale, the warming effect of methane per unit mass is 28 times higher than that of carbon dioxide (CO_2) (IPCC. Climate Change 2013), and its emissions constitute the second-largest contribution to historical warming after CO_2. Methane release into the atmosphere influences and will influence the global climate (Shindell et al., 2009).

In the fjords of Spitsbergen, a correlation between the major stratigraphic units and structural elements of the fjords, different seabed morphologic expressions such as pockmarks (Roy et al., 2015, 2019), gas seepage detected in the water column and the modeled GHSZ (Betlem et al., 2021) is missing. Consequently, this study focuses on integrating and evaluating the fluid flow from the source rocks to the water surface in Isfjorden and Van Mijenfjorden (Figure 1, B) to

assess the potential distribution and stability of NGH based on indirect hydrate indicators (geological, geophysical and geochemical attributes to the presence of hydrates) seen in the seafloor and the water column.

To fulfill the purpose of the research, I have inquired the general gas system of the fjords of central Spitsbergen, describing the main geological groups and formations outcropping in the fjords and having an insight into the potential fluid migration pathways to the seafloor. I analyzed the seepage recorded in the water column echograms from two cruises (August 2015 and June 2021) and correlated it with different seabed morphologies. This has allowed me to compare the characteristics of the formerly detected flares over two different seasons and evaluate temporal variabilities of the seepage between late spring and early autumn in the fjords. Finally, I tried to assess the input of methane into the atmosphere, aiming to provide enhanced information to constrain uncertainties in future climate scenarios related to possible near-shore NGH dissociation in a climate-sensitive area such as the Svalbard archipelago (Ruppel and Kessler, 2017).

The outcome of this work will contribute valuable scientific data and complement previous studies of the gas system in other fjords of the archipelago. It will also facilitate further investigation of observed phenomena responding to the presence of NGH by comparing the GHSZ thermodynamic requirements with the direct and indirect hydrate indicators. Inferring this data is vital to assess the hydrate-related resource potential and mitigate hydrate-related geohazards such as submarine landslides. Exploring and quantifying the NGH in the Svalbard archipelago is essential since its dissociation could result in immense amounts of methane into the atmosphere, contributing to positive feedbacks enhancing the polar amplification and global warming (Ruppel and Kessler, 2017; Betlem et al., 2021).

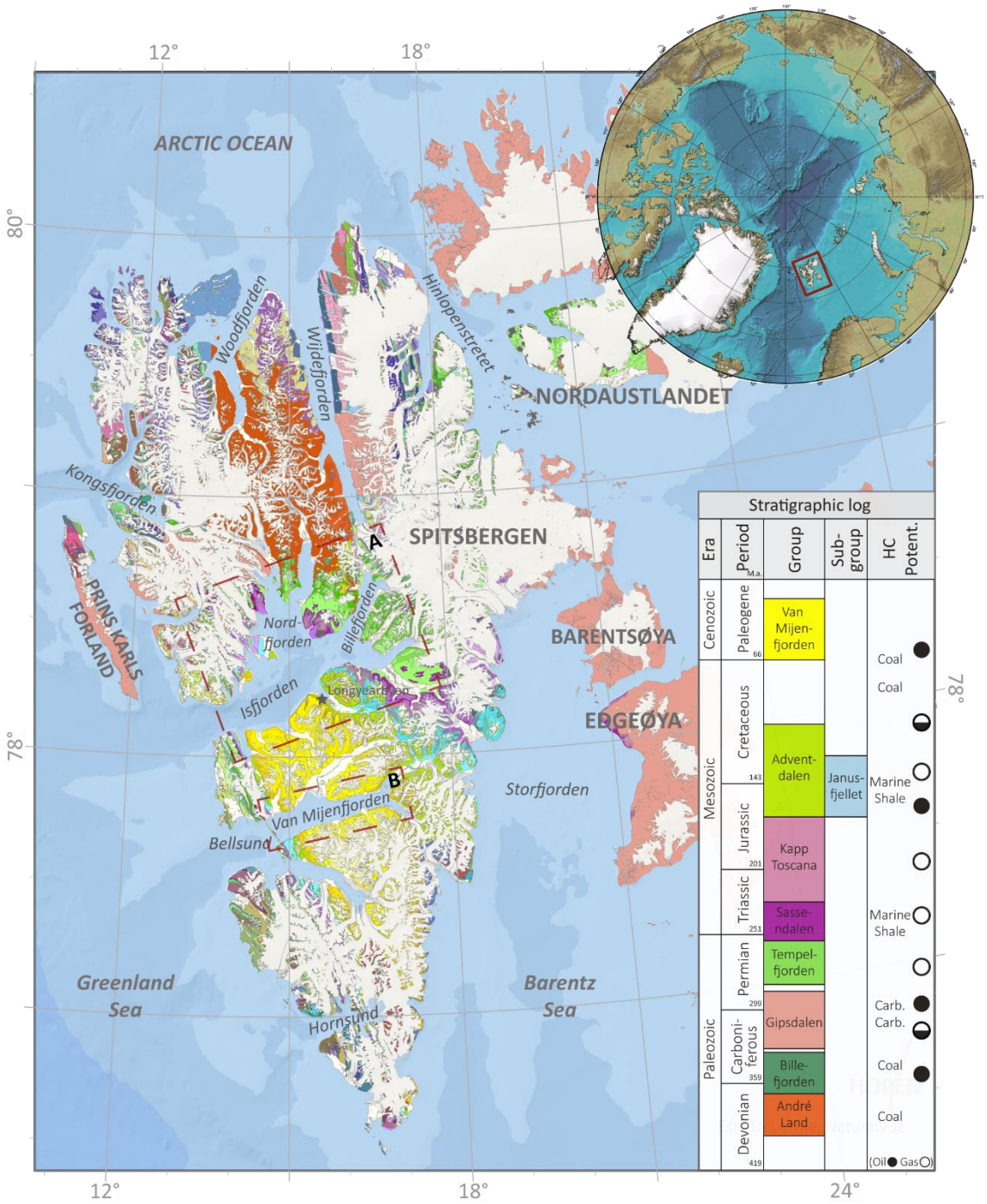

Figure 1. Regional map of Svalbard archipelago in EPSG:32633 projection. The red-discontinuous polygons are the study areas: A. Isfjorden area; B: Van Mijenfjorden area. In the upper right corner is the International Bathymetric Chart of the Arctic Ocean (IBCAO) Version 3.0 (Jakobsson et al., 2012). The stratigraphic log is based on Betlem et al., 2021, and the Stratigraphic Atlas of the Arctic.

2. STATE-OF-THE-ART BACKGROUND

2.1. Methane seepage

Natural methane seepage is the upward migration of methane gas that commonly occurs in both terrestrial and marine settings (Kvenvolden et al., 2001). The flow of gaseous hydrocarbons from subsurface sources to Earth's surface can be steady or episodic, slow or rapid, visible or invisible (Etiope, 2015), and that is why the rates of methane seepage are difficult to assess.

The sources of methane are varied, and they are broadly grouped into modern microbial carbon and ancient thermogenic carbon. Microbial methane gas is produced by methanogenic organisms that chemically break down the organic matter and generate methane under anaerobic conditions. Thermogenic methane gas is the result of chemical reactions that occur under high temperatures and pressure underground. It originates from deep source rocks, which commonly include shales, coalbeds and limestone. In both cases, if methane reaches the sediment surface and the gas concentration in the pore water exceeds saturation, methane gas will exolve in the water column (Bohrmann and Torres, 2006).

Marine seeps are an important contribution of methane to the atmosphere. It is estimated that 50 Tg/yr are released from the seabed, of which about 30 Tg/yr reaches the atmosphere. Methane oxidation and dissolution are two crucial processes limiting the amount of methane transferred to the atmosphere (Kvenvolden et al., 2001). Microbial methane oxidation is a microbial process that happens in both anaerobic and aerobic conditions. It is an important methane sink since it consumes over half of the total methane produced on Earth. On the other hand, methane dissolution happens during methane transport through the water column. Gas bubbles rising from great depth can be coated by a clathrate hydrate layer. This phenomenon slows the rate of gas dissolution from the bubbles, which will survive much longer in the water column, increasing the chances to reach the water surface (Kvenvolden et al., 2001).

Marine seeps are traditionally called "cold seeps" to distinguish them from the hot and CO_2-rich hydrothermal vents (Etiope, 2015). They are found in passive continental shelves and slopes, and can be associated with seabed morphologies such as pockmarks, which are produced by the expulsion of fluids.

2.2. Natural gas hydrates (NGH)

Natural gas hydrates, also called clathrates, are non-stoichiometric solid compounds, similar to ice crystals with water as the host element and a lightweight gas molecule acting as a guest (Sloan, 1998). They form three-dimensional (3D) stacking cages of hydrogen-bonded water molecules, with Van der Waals forces holding the lattice together. No bonding exists between the guest and host molecules. Nevertheless, the empty cage is unstable and requires encapsulated gas molecules to stabilize the clathrate crystal (Collett et al., 2009).

Five types of polyhedral cages are known (Figure 2). Depending on the formation environment, hydrates crystalize naturally in three different structures (I, II, H), with varying cage sizes (Sloan, 1998). Each cage can hold a single gas molecule and the gas changes depending on the hydrate structure.

- Structure I: Crystalizes in the cubic (isometric) system. It is formed by 46 water molecules that enclose 8 cages where gas molecules are hosted. It consists of two types of cages: Six larger gas sites are enclosed by water cages with 12 pentagonal and 2 hexagonal faces (5^{12} 6^{2}), while two smaller gas sites occur within pentagonal dodecahedral cavities. It has a size of 5.2 Å.

  It is the most common structure observed in nature. Methane molecules typically fill both small and large cages. However, other gas molecules that are smaller than propane (C_3H_8), such as CO_2 or H_2S, can be enclosed in the structure.
- Structure II: Crystalizes in the cubic (isometric) system. It consists of 136 water molecules forming 24 cages. The smallest consists of 12 pentagonal faces (5^{12}) (4.8 Å), and the large consists of 12 pentagons and 4 hexagonal faces (5^{12} 6^{4}) (6.9 Å).

  This structure is usually confined to areas where the formation of thermogenic gas takes place in the sediment. The typical guest molecules are O_2 and N_2, but C_3H_8 or iso-butane ($HC(CH_3)_3$) can also be found.
- Structure H: Crystalizes in a hexagonal system. It has 34 water molecules associated with 3 small (5^{12}), 2 medium-sized (4^{3} 5^{6} 6^{3}) and 1 exceptionally large (5^{12} 6^{8}) cages.

  To be stable, it requires the cooperation of two guest gases (large and small). Different combinations are possible. They have only been found in the Gulf of Mexico, related to heavy hydrocarbons.

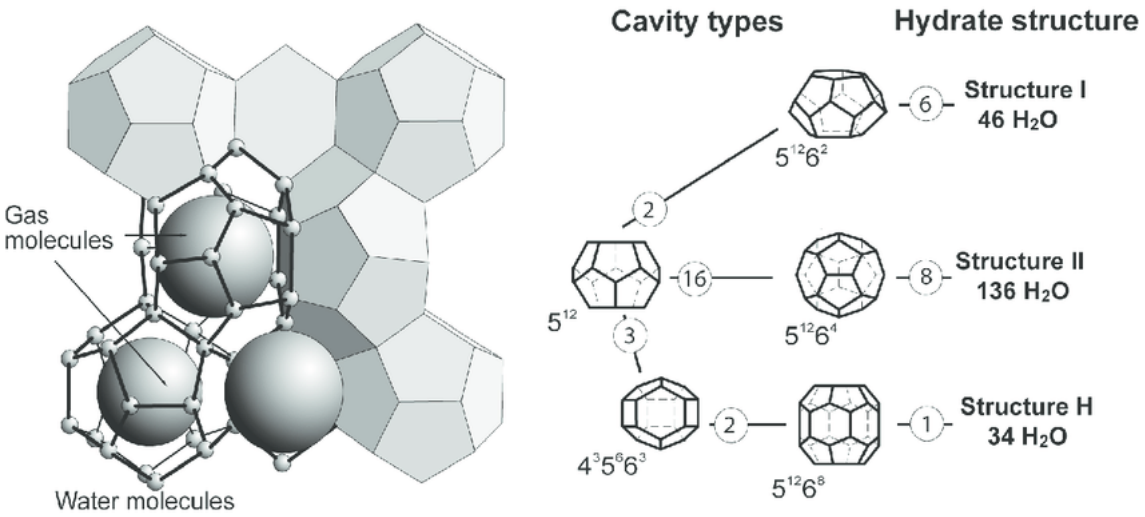

Figure 2. Figure published by Bohrmann and Torres, 2006.The figure on the left side is a gas hydrate of type structure I; small spheres are water molecules forming cages; large spheres are gas molecules. The figure on the right is a diagram with the cage types and the number of individual cages forming the three common hydrate crystal structures. The circled numbers denote the numbers of the cages used to form the hydrate structure.

Pressure (i.e., water depth), the seafloor temperature, and the geothermal gradient are the primary parameters affecting the gas hydrates stability zone in marine environments (Sain et al., 2011). Other parameters such as the gas composition or the pore water salinity also influence the stability curve. These factors are used to calculate a theoretical diagram to estimate the local stability of NGH at any depth. The gas hydrate stability zone (GHSZ) is the zone at which temperature, pressure and geochemical regimes meet the requirements for the stable natural occurrence of NGH of a specific composition. Above or below the GHSZ, the gas either dissolves in the water or remains in a free state (Figure 3).

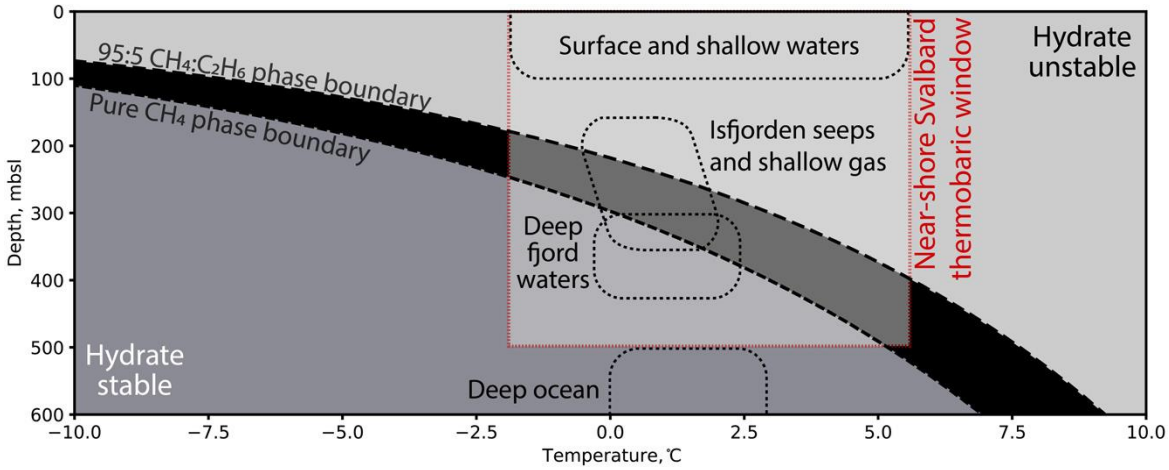

Figure 3. Schematic illustration of Svalbard's fjords' estimated GHSZ (for pure CH_4 and a mixture of CH_4:C_2H_6 of 95:5). Figure published by Betlem et al., 2021.

As the temperature in sediments increases with depth with a uniform geothermal gradient, the thickness of the GHSZ is quite constant for a given depth (Bohrmann & Torres, 2006). Therefore, the lower boundary of the GHSZ acts as an isotherm that can sometimes be characterized using seismic methods by the Bottom-Simulating-Reflector (BSR) (Shipley et al., 1979). BSR is a strong reflector of reverse polarity that mimics the seabed topography cutting across reflections of stratigraphic origin (Bohrmann & Torres, 2006). It appears as a result of the decrease of impedance between the NGH and free gas (Paull et al. 1996; Cooper and Hart, 2003).

During the formation of gas hydrates, the water and the gas content in the sediment pores are converted into solid form, increasing the sediment strength. Depending on the formation environment, NGH deposits can present different fabrics (disseminated, nodular, layered and massive). In deep marine environments, it is typical fracture and pore space fillings, while, in shallow environments, layers of NGH parallel to bedding, massive hydrates and bubble fabric are prevalent. This makes NGH relevant for the stability of the seafloor sediments, playing a significant role in pre-conditioning slopes for failure (Hornbach et al., 2007).

The compact nature of the hydrate structure makes it highly effective for packing gas. A volume of 1 m^3 gas hydrate at standard pressure and temperature (101.3 kPa, 273.15 K), contains 164 m^3 of gas and 0.8 m^3 of water. Gas hydrate volume estimates rely on two basic parameters: the amount of pore space, or porosity, available for gas hydrates in the stability zone (Kvenvolden, 1988). Their heterogeneous distribution and uncertainties in porosity and gas hydrate saturation have led to widely varying global estimates of the methane contained in hydrates. Different assessments address the hydrate distribution patterns (Archer, 2007) to improve the constrained estimations of this energy source.

Methane is a dynamic component of the sub-sea-floor environment and the global environment as a whole. Gas hydrates can be charged with methane over time or discharged, releasing large quantities of methane (Dickens et al., 2011). If methane inputs to gas hydrate exceed methane outputs, gas hydrate volumes grow whenever pore water is available, sequestering methane as the hydrate forms. They can act as a methane source, releasing methane as the hydrate breaks down.

Gas hydrates played a significant role in past climate changes, like the Palaeocene-Eocene thermal maximum (PETM), when the global temperatures rose by 5 to 6°C over a 1 to 10 thousand year period (Dunkley-Jones et al., 2010). Current temperature increases and lowering

pressures could trigger NGH dissociation, strongly influencing the environment and climate, and becoming an important factor in future global warming.

Most methane released from dissociating gas hydrates in the marine environment is dissolved and oxidized into carbon dioxide in the deep-ocean water. However, permafrost found in fjord systems, which account for 0.25% of the global gas hydrates (Ruppel et al., 2011), are likely to release methane, a fraction of which can reach the atmosphere directly (McGinnis et al., 2006).

Marine gas hydrates have a global distribution (Figure 4). They have been found or inferred in sub-oceanic sediments in the polar regions (shallow water) and in the continental margin and onshore permafrost, where pressure and temperature conditions combine to make them stable. It is estimated that 99% of the world's gas hydrate occurs in the uppermost hundreds of meters of marine sediments at ocean depths greater than 500 m (300 m in the polar oceans (Kvenvolden, 1998)) and close to any passive and active continental margin (Dale et al., 2008).

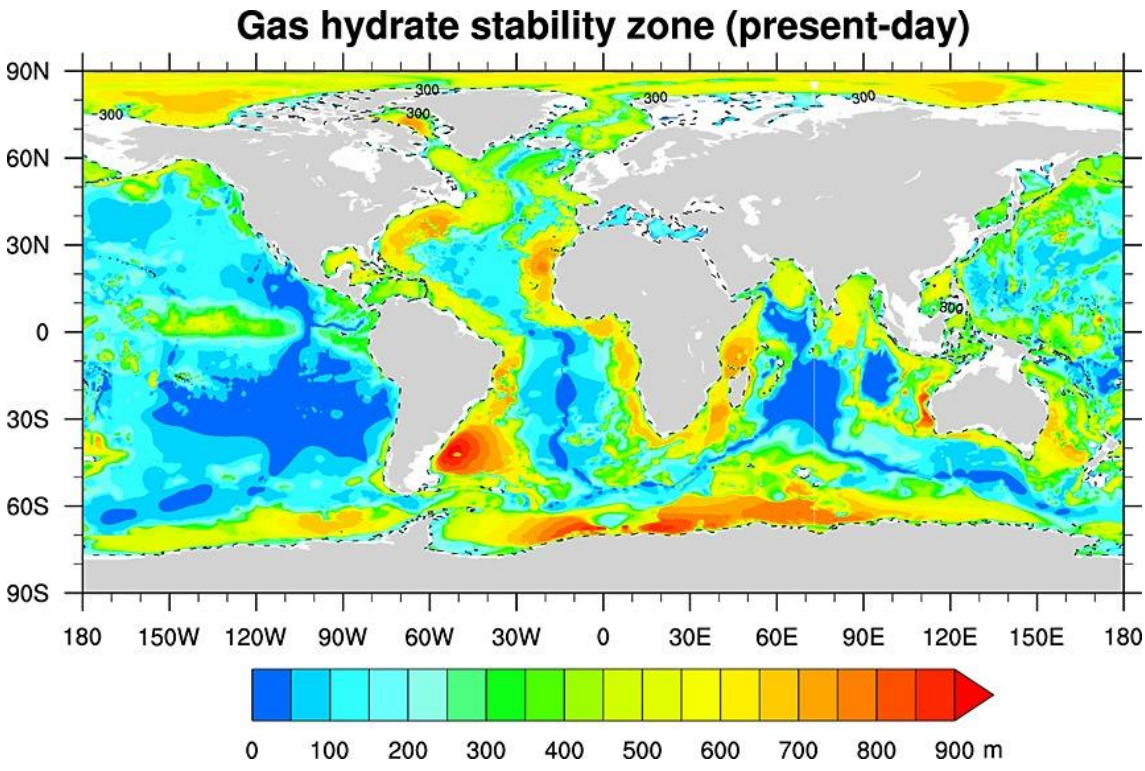

Figure 4. The global map of the modeled GHSZ thickness in meters under present-day climatic conditions (mean 1988-2007). Figure published by Kretschmer et al., 2015. Global estimates present considerable limitations due to the model's resolution. Consequently, this figure shows GHSZ anywhere in Svalbard. Nevertheless, regional models by Betlem et al., 2021 predict a stable GHSZ under thermogenic conditions in multiple fjords of the archipelago.

2.3. Geological and physiographic setting

2.3.1. Geological evolution of Svalbard

Geologically, the Svalbard archipelago represents the uplifted and exposed north-western corner of the Barents Shelf. The stratigraphic setting displays a nearly complete stratigraphical succession ranging from Pre-Ordovician basement and Devonian Red sandstones to the Paleogene basin-infill of the Central Spitsbergen Basin (CSB), offering multiple organic-rich source rocks and porous reservoir rocks (Henriksen et al., 2011; Worsley, 2008; Dallmann et al., 2015).

Evidence of past and present faulting is widespread throughout the archipelago (Harland et al., 1974; Lowell, 1972; Betlem et al., 2021). Western and central Spitsbergen have been affected by structural shortening during the West Spitsbergen Fold-and-thrust Belt formation during the Paleogene, causing extensive fracturing and structural heterogeneities that can serve as fluid migration and leakage pathways (Henriksen et al., 2011; Ogata et al., 2014).

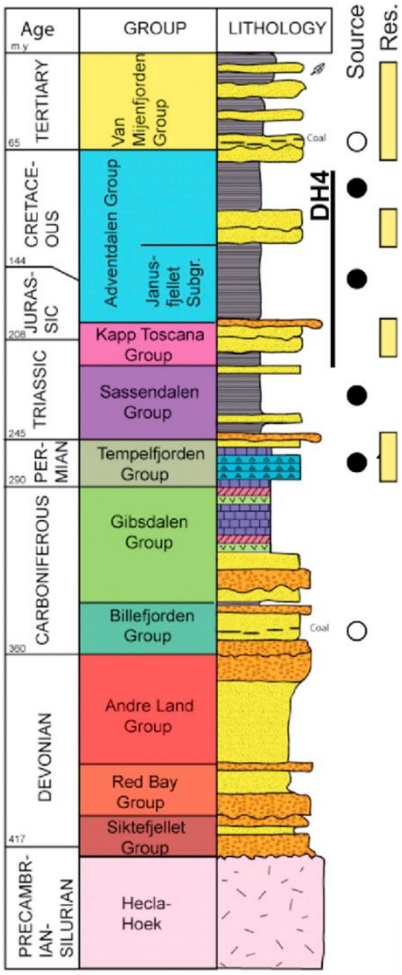

Figure 5. Stratigraphic column published by Betlem et al., 2019. It is based on an unpublished figure by Arild Andresen (University of Oslo). Source rock intervals (Abay et al., 2017) and reservoir units (Res.) are highlighted.

The entire stratigraphic sequence is clastic-dominated, and the only significant carbonates are found in the late Carboniferous and early Permian (Worsley et al., 1986). The following groups are found in Spitsbergen (from the oldest to the youngest):

Andrée Land Group, Early Devonian (Emsian 405 Mya) - Late Devonian (Famennian 371.1 Mya). It is >3000 m succession of Devonian rocks consisting mainly of distinct red, crimson or greyish-green conglomerates, sandstones, siltstones, mudstones and shales, locally with limestone interbeds. The lower beds result from alluvial fans, braided to meandering rivers, and alluvial plains depositing in a dry to semi-dry climate. The upper, greyish-green strata reflect coastal tidal plains, brackish lagoons, estuaries and delta environments, possibly deposited under more humid conditions (Dallmann et al., 2015).

Billefjorden Group, part of the Late Devonian (Famennian 371.1 Mya) - Middle Carboniferous (Visean 330.3 Mya). It is a <1000 m succession of greyish conglomerates, sandstones and shales locally intercalated with coal seams. It represents paleo-environments dominated by large alluvial fans, fluvial, lacustrine and alluvial environments in a warm, humid climate. Coal seams and abundance of vegetation remains reflect a varied and richly vegetated paleoenvironment dominated by swamp forests and wetlands (Dallmann et al., 2015).

Gipsdalen Group, Middle Carboniferous (Serpukhovian 325 Mya) - Early Permian (Artinskian 290.5 Mya). It is a <1800 m succession of red conglomerates, sandstones, siltstones and shales in the basal beds, that change into evaporites (gypsum and anhydrite) and carbonates (dolostones and limestones). The basal beds were deposited in terrestrial steppe- to desert-like paleoenvironments. These changed to coastal sabkhas and tidal flats that migrated into a shallow-marine, warm-water shelf sea studded with coral reefs and extensive carbonate platforms. Finally, a global sea-level fall resulted in the emergence and karstification of the platforms (Dallmann et al., 2015).

Tempelfjorden Group, Middle Permian (Artinskian, 283.3 Mya) - Late Permian (Changhsingian 251.9 Mya). It is a <460 m succession formed by highly variable deposits that comprise marine clasts (sandstones, siltstones and black shales), spiculitic cherts (accumulations of sponge spicules) and carbonates, that were accumulated in temperate to cold, shallow-marine, nearshore to deeper marine offshore environments (Dallmann et al., 2015).

Sassendalen Group, Early Triassic (Induan, 251.9 Mya - Middle Triassic (Carnian, 237 Mya). It is a <700 m succession with diverse lithologies. Along western Spitsbergen, marine clasts were deposited in a low-relief, reasonably deep, boreal shelf embayment with coastal to deltaic sediments. The Middle Triassic is very organic-rich and consists of sandstones, siltstones and shales that were deposited in the central part of the embayment from Svalbard. Shale dominates, along with siltstones; sandstone intervals in the west (Dallmann et al., 2015).

Kapp-Toscana Group, Late Triassic (Carnian, 237 Mya) - Middle Jurassic (Bathonian, 168.2 Mya). It is a <475 m succession formed by shales, siltstones and sandstones with coal layers and scattered carbonate beds deposited in alluvial, paralic, deltaic and shallow-marine environments. The uppermost part forms a condensed clastic sedimentary succession containing thin phosphatic nodule layers (Dallmann et al., 2015).

Adventdalen Group, Late Jurassic (Callovian, 164 Mya) - Early Cretaceous (Albian, 105 Mya). It is a <1600 m succession that was deposited in the epicontinental basin. The lower part consists of organic-rich mudstone deposited on a marine shelf, and this passes upwards into a unit dominated by shale deposited on an open-marine environment. The upper part of the group is a response to uplift in the north, from where coarse-grained sediments were delivered to build up a fluvial to deltaic, southeastwards prograding wedge of conglomerates, sandstones and shales with subordinate coal beds. This wedge was later drowned by a shallow sea that deposited sand, mud and fossiliferous calcareous sediments (Dallmann et al., 2015). The reflectors defining the Adventdalen Group units depict a wide and asymmetric syncline of deposits of Late Jurassic - Early Cretaceous. The Upper Cretaceous strata are missing, forming an unconformity with the Van Mijenfjorden Group's Paleogene.

Van Mijenfjorden Group, Paleogene (Danian, 66 Mya) - (Priabonian, 33.9 Mya). It is a <900 m succession deposited in Central Spitsbergen Basin. It consists of continental sandstones, siltstones and shales with plant beds and coal seams deposited in coastal (deltaic) to shallow-marine environments (Dallmann et al., 2015).

2.3.2. Spitsbergen petroleum system elements

Multiple investigations have unveiled the presence of a functional petroleum system in Spitsbergen. Hydrocarbon presence has been found by technical discoveries in several wildcat exploration wells onshore (Senger et al., 2019). Also, an unconventional discovery of shale gas was found in research wells in Adventdalen (Ohm et al., 2019). Thermogenic, an admixture of biogenic, mixed microbio- and thermogenic gas seeps, have been documented in the marine sediments of Isfjorden (Knies et al., 2004). Multiple pockmarks have been described in Isfjorden (Roy et al., 2015, 2019). Finally, numerous sedimentary rocks outcrop in different sites of Spitsbergen (Abay et al., 2017), of which it outstands the Middle Triassic Botneheia and Upper Jurassic Agardhfjellet Formations as the main source rocks for oil and gas found in Spitsbergen (Bjorøy et al., 2010; Henriksen et al., 2011; Mørk and Bjorøy, 1984).

The Agardhfjellet Formation is part of the Janusfjellet Subgroup and the Adventdalen Group and was deposited in the Late Jurassic. It is 90-350 m thick. Its dominant lithology is siltstone, sandstone and beds of black organic-rich shales. These represent deposition in alternating oxic and anoxic bottom conditions, indicating periodic deposition under very shallow water into the fair-weather wave base (Koevoets et al., 2019). The shales did bury up to 2.5 km under paleo-burial temperatures of 150-180°C (Koevoets et al., 2016). There is a high percentage of vitrinite-

rich type III kerogen in areas with more silty parts, while clay-dominated areas are rich in liptinitic type II kerogen, meaning that the formation has the potential to generate both oil and gas (Ohm et al., 2019).

Botneheia Formation is part of the Sassendalen Group, deposited in the Middle Triassic. Its lithology is defined by black shale with abundant small phosphate nodules, silty dolomite and the upper part is highly calcitic due to numerous marine fossils and reptile bone fragments. The formation presents a changing thickness of 80-168 m. The upper part is very rich in organic material, presenting lateral variations in maturity, with high total organic carbon (TOC) values (5-10%), high hydrogen index (HI) values (400-600 mg HC/g TOC), low production index (PI) (0.04-0.1) and Tmax (439-446°C) suggesting excellent source rocks composed of oil-prone Type II kerogen. Isotope and biomarker data suggest shallow/open marine facies. The source rocks from Svalbard are more mature than their time-equivalent formations offshore Barents Sea (Abay et al., 2014). Botneheia Formation is the most promising hydrocarbon source rock of Svalbard and one of the major source rocks in the southwestern Barents Sea (Abay et al., 2017).

2.3.3. Subsurface fluid flow in the archipelago

Gas occurrences described in Isfjorden are in close association with seafloor expressions and tectonic lineaments. This suggests that stratigraphy, lithology and faulting control the fluid flow migration from deep source rocks in Isfjorden (Roy et al., 2014).

Faults are the primary conduits for fluids in many basins worldwide, providing direct routes for the buoyant hydrocarbon fluids through the deeper subsurface where more consolidated to completely lithified rocks are present (Ligtenberg, 2005). In the Spitsbergen Fold-and-thrust Belt complex, various types of faults and fracture networks have been documented (Maher et al., 1986; Teyssier et al., 1995; Braathen et al., 2012), underlining a relevant role in the migration of fluids ascending from deep source rocks and terminating on the seafloor (Roy et al., 2014).

In Isfjorden, different acoustic features such as enhanced reflections, turbid acoustic zones and acoustic blankings have been interpreted on subbottom acoustic profiles and linked with regional faults. They suggest possible gas accumulation and migration through the various shallow fractures in the bedrock up to the seafloor (Roy et al., 2014).

Early Cretaceous doleritic intrusions are exposed both onshore and offshore Isfjorden (Senger et al., 2013). They are implied to have a crucial role in directing the buoyant flow towards the

surface (Roy et al., 2014). The impermeable permafrost layer could act as another mechanism directing the migration of fluids to seep through to the seabed in places where the permafrost is absent (Roy et al., 2014).

Pockmarks (crater-like depression features on the seafloor) and pingos are morphological features related to the expulsion of fluids from deep sources (Vanneste et al., 2005; Roy et al., 2014; Dallmann et al., 2015). In high latitudes, groundwater seepage, thawing permafrost, gas hydrate dissociation and up-drifting ice detached from the seafloor are important factors for pockmark formation. Roy et al., 2012 and 2015 discussed and described the morphology and spatial distribution of 1304 pockmarks in Isfjorden. These were found closely linked to the outcropping edge of the igneous intrusions and shallow and deep faults, which could have acted as migration pathways of fluids to the seafloor. However, it is also suggested that they could result from direct fluid migration from organic-rich geologic formations (Agardhfjellet and Botneheia Formations) into the soft, fine-grained sediments (Forwick et al., 2009).

2.3.4. Gas system in the fjords of Svalbard

The Svalbard archipelago groups three crucial factors contributing to the presence of NGH: 1) suitable thermobaric conditions, 2) an active petroleum system, 3) a constant flux of thermogenic and microbial gas. Flares, pockmarks and thermogenic methane found in several Svalbard fjords are evidence of active fluid seepage both onshore and offshore the archipelago (Betlem et al., 2019).

Several organic source rocks are widespread in Svalbard, with examples including Paleozoic, Mesozoic, and Cenozoic coals in addition to the two Mesozoic organic-rich marine mudstones, Agardhfjellet Formation and Botneheia Formation, which are the main sources for the migrating hydrocarbons in Spitsbergen (Nøttvedt et al., 1993; Paech and Koch, 2001; Nicolaisen et al., 2019). These can potentially release large amounts of methane into the water column. Nevertheless, it is estimated that the biological oxidation effect in the near-surface sediments will effectively reduce the amount of methane seeping (Liira et al., 2019).

Significant quantities of hydrate-bound gas have been discovered in the extensively studied offshore provinces of Vestnesa Ridge on the continental slope west of Svalbard and Prins Karls Forland. In the fjords of the archipelago, several studies (Forwick et al., 2009; Roy et al., 2016, 2015; Liira et al., 2019) have found evidence of fluid seepage. However, the near-shore NGH potential in Svalbard fjords is poorly constrained with indirect offshore hydrate indicators

(seismic chimneys, pockmarks, seismic blanking). No clear hydrate-related signatures have been identified despite good 2D seismic coverage (Bælum and Braathen, 2012; Blinova et al., 2013).

By modeling the GHSZ, methane hydrate-stable conditions have been predicted in Isfjorden (Figure 6), Hinlopenstretet, Kross- and Kongsfjorden, and Rijpfjorden, but they do not predict such conditions for Bellsund (Betlem et al., 2021). This coincides partially with field observations, which documented high methane concentrations in Isfjorden, Hornsund, Van Mijenfjorden, Adventfjorden and Tempelfjorden, with methane concentrations exceeding the atmospheric equilibrium concentration up to two orders of magnitude (Damm et al., 2005; Damm et al., 2021).

In Isfjorden, 1304 individual pockmarks have been recorded in water depths of 40–320 m (Roy et al., 2015) (Figure 6). The formation and distribution of pockmarks have been related to the possible dissociation of NGHs, major tectonic faults and igneous conduits, which may act as potential fluid pathways, seepage of shallow gas, permeable fluid migration pathways and external trigger mechanisms such as seismic activity (Roy et al., 2015, 2019). Furthermore, many of the newly identified flares, pockmarks, and other fluid seepage features detected in the fjord are found within or in close proximity to the GHSZ (Betlem et al., 2021) (Figure 6).

A mixture of thermogenic and microbial methane were analyzed from surface sediments of Isfjorden (Knies et al., 2004; Liira et al., 2019). These gases are proven to seep from both the pockmarks and undisturbed seafloor, suggesting a slow and steady degassing of the fjord sub-surface. The geochemical characterization indicates an active fluid flow system in Isfjorden (Knies et al., 2004; Liira et al., 2019).

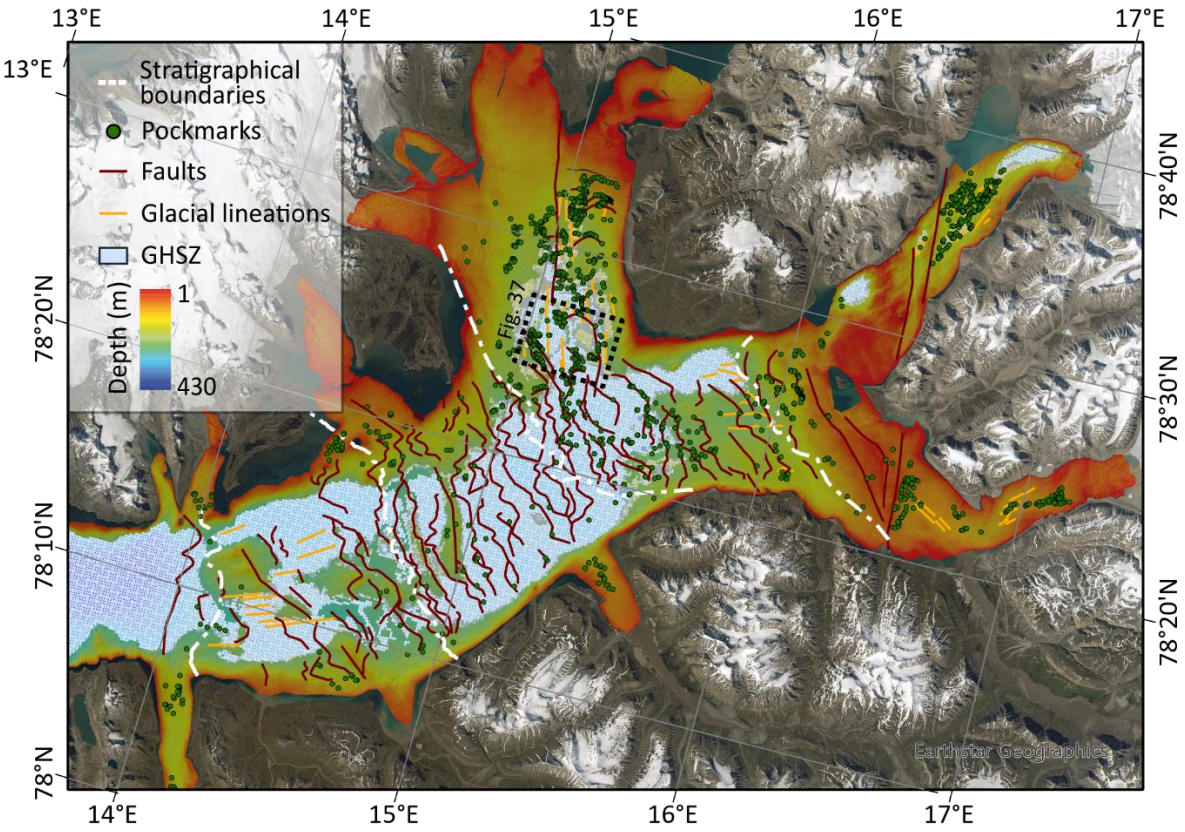

Figure 6. Compilation of the background information from Isfjorden. The stratigraphical boundaries were interpreted by Blionva et al., 2012. The pockmarks, glacial lineations and faults were described by Roy et al., 2015. The GHSZ was modeled by Betlem et al., 2021, and represents the maximum extent for thermogenic gas conditions. The base map is courtesy of Earthstar Geographics.

2.3.5. Physiographic conditions of the study area

This work's study area is in Isfjorden and Van Mijenfjorden, two of the main fjords in western Spitsbergen, in the Svalbard archipelago, located in the Arctic Ocean, midway between Norway and the North Pole (Figure 1). Svalbard comprises all islands between 74° and 81° north and between 10° and 35° east. Spitsbergen is the largest island with a land surface of 39.000 km^2 (Ingólfsson, 2004).

Central Spitsbergen presents higher-than-expected temperatures compared to other parts of the High Arctic in the same latitude (Eckerstorfer and Christiansen, 2011) due to the West Spitsbergen Current (WSC). The WSC brings warm and saline Atlantic Water (AW) in the upper 500–700 m along the shelf break and slope towards the north (Przybylak et al., 2014). The current mean annual air temperature in Longyearbyen and the surrounding area (-5 to 0°C) has changed significantly during the 1961–1990 period due to a regional increase of 1–2°C since

1981 (Isaksen et al., 2017). However, the present temperature range still allows the occurrence of gas hydrates both within or below the permanently frozen soil layers (Betlem et al., 2019).

The waters around Svalbard feature a large seasonal variability in water column temperatures, and the bottom water temperatures are complicated by factors that include effects of water-terminating glaciers, sea ice formation, and potentially subsea permafrost (Skogseth et al., 2020).

2.3.5.1. Isfjorden

Isfjorden is the largest fjord system in western Spitsbergen. It is comprised of a main trunk with thirteen tributary fjords (Figures 1 A, 7). The Isfjorden main trunk (IMT) is 8–25 km wide and 107 km long. The deepest point of the IMT is the Svensksunddjupet basin (430 m), located near the mouth of the fjord (Figure 7). Isfjorden has a total area of 3084 km^2 and a volume of 390 km^3 (Nilsen et al., 2008).

Its bathymetric relief is characterized by sub-parallel ridges, bedrock knobs, streamlined bedforms, sediment debris lobes, and numerous pockmarks (Roy et al., 2012, 2015). The bedrock structures in Isfjorden and Isfjordbanken span from Paleozoic carbonates and evaporites to Mesozoic and Paleogene sandstones and shales (Dallmann et al., 1999). The sedimentary environment of IMT was influenced by nine tidewater glaciers that terminated there during the Younger Dryas and the Allerød period, which now are covered by the early-Holocene glacial, subglacial and deglacial deposits (Forwick and Vorren, 2009).

Adventfjorden

Adventfjorden is a small side fjord situated in the southern part of Isfjorden (Figure 7). The fjord is about 8 km long and 3.5 km wide. Water depths range from 50 to 80 m in the central part, and it reaches nearly 100 m in the fjord's mouth. It has a wide, deep fjord inlet without a sill, which provides easy water exchange with the IMT (Damm et al., 2021).

Tempelfjorden

Tempelfjorden is the easternmost tributary fjord of Isfjorden (Figure 7). It is 14 km long and 5 km wide and covers an area of 57 km^2 (Forwick et al., 2010). Water exchange is, to some extent, restricted from Isfjorden. Tempelfjorden has two basins separated by a sill (Figure 7). The outer

basin is 110 m deep, and it is shared with Sassenfjorden (Damm et al., 2021). The inner basin is much shallower is highly influenced by the tidewater glacier Tunabreen (Forwick et al., 2010).

Nordfjorden

Nordfjorden is located in the northernmost part of the inner part of Isfjorden. It is approximately 20 km long and 17 km wide (Figure 7). The water depth in Nordfjorden varies from 7 to 260 m. It has a wide and deep mouth providing an easy water exchange with the IMT. It concentrates the highest density of pockmarks in the Isfjorden fjord system (Roy et al., 2015).

Sassenfjorden

Sassenfjorden is located on the eastern side of Isfjorden, between the main trunk and Tempelfjorden (Figure 7). It is approximately 15 km long and 10 to 5 km wide (close to Isfjorden and close to the mouth of Tempelfjorden, respectively). It is separated from Tempelfjorden by a sill with a maximum depth of about 55 m, limiting the water exchange with Isfjorden, which only overflows under specific circumstances (Damm et al., 2021).

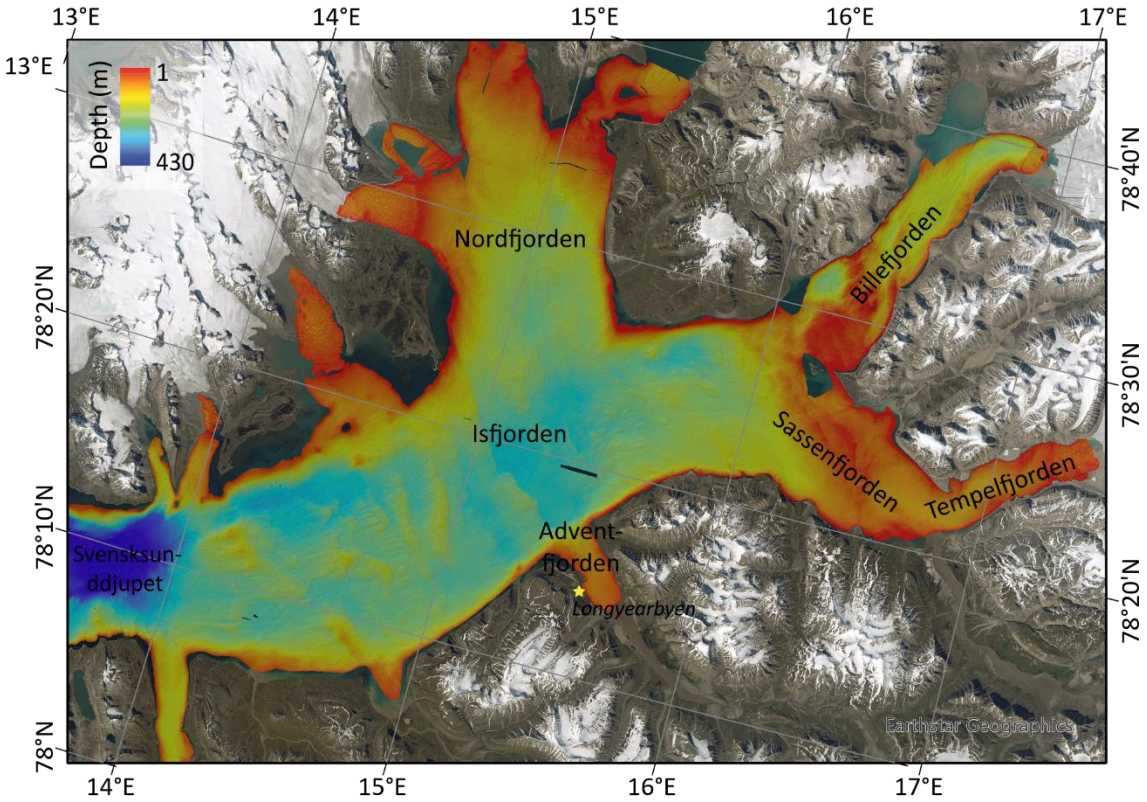

Figure 7. Bathymetric relief of Isfjorden and the main tributary fjords in EPSG:32633 projection.

2.3.5.2. Van Mijenfjorden

Van Mijenfjorden is the second-largest fjord in western Svalbard, comprising 50 km long and 10 km wide (Figure 1, B). It is divided into three basins with a maximum depth of 112 m in the outer basin, 74 m in the middle basin and only 30 m deep in the inner basin. The fjord is separated from Bellsund further out by Akseløya and Mariaholmen islands, which block more than three-quarters of the fjord entrance, restricting ocean communication. Van Mijenfjorden is characterized by a shallow sill, as well as the shallower depths of the inner basins in relation to the shelf depth in front of the fjord (Damm et al., 2005).

Stratigraphically, Van Mijenfjorden is dominated by a large syncline forming part of the Spitsbergen central basin, a sedimentary bedrock of various types such as sandstones, siltstones, shales, coals and coal pebbles (Steel and Worsley, 1984). The inner basin is filled mainly with glaciogenic sediments, with a thickness of >30 m. The outer basin is dominated by up to 20 m of glaciomarine sediments resting on a till deposited during the Younger Dryas (Hald et al., 2001). The current sea-floor surface sediments are dominantly silty clay (Hald and Korsun, 1997).

3. RESEARCH OBJECTIVES

In this thesis, I study the fluid flow distribution and characteristics as an indirect indicator of the potential NGH occurrence in the fjords of western Spitsbergen. The focus on Isfjorden and Van Mijenfjorden is owing to the richness in available data, previous modeling of the GHSZ (Betlem et al., 2019; 2021), and their relatively easy accessibility from Longyearbyen.

Seven research objectives were addressed through this study:

1. Determine if flare intensity, height and time deflection are valuable parameters for characterizing the seepage distribution in the shallow waters of fjords.
2. Describe the gas seepage and evaluate if it manifests strong seasonality as a result of the fjord's hydrographic characteristics.
3. Asses if present-day fluid expulsion identified in the acoustic flare data correlates with the pockmark distribution in Isfjorden.
4. Investigate if the gas seeps detected in the water column result from the temporal destabilization of the GHSZ and NGH dissociation.
5. Examine if geological heterogeneities like fault zones, igneous intrusions and high-permeable strata control subsurface fluid migration in the fjords.
6. Interpret the organic-rich formations -namely Agardhfjellet and Botneheia Formations- outcropping in the fjords and assess if they are the source rocks for the gas seeping in the fjords.
7. Estimate if the gas seepage detected in the fjords directly contributes to the atmospheric carbon pool via methane diffusion from the water column to the atmosphere.

4. DATA AND METHODS

The work performed in this study is summarized in a flowchart (Figure 8) that schematically shows the different methods that I applied to make the geostatistical data analysis. 2D seismic interpretation of the general stratigraphy of the fjords, multibeam and backscatter data for describing seabed morphologies, hydroacoustic data for flares detection, air analyzer for detecting the atmospheric CO_2 and CH_4 concentrations, water sampling for hydrocarbon analysis, and CTD sampling for the water column characteristics. It is complemented with Table 1, which integrates all relevant datasets and sources utilized.

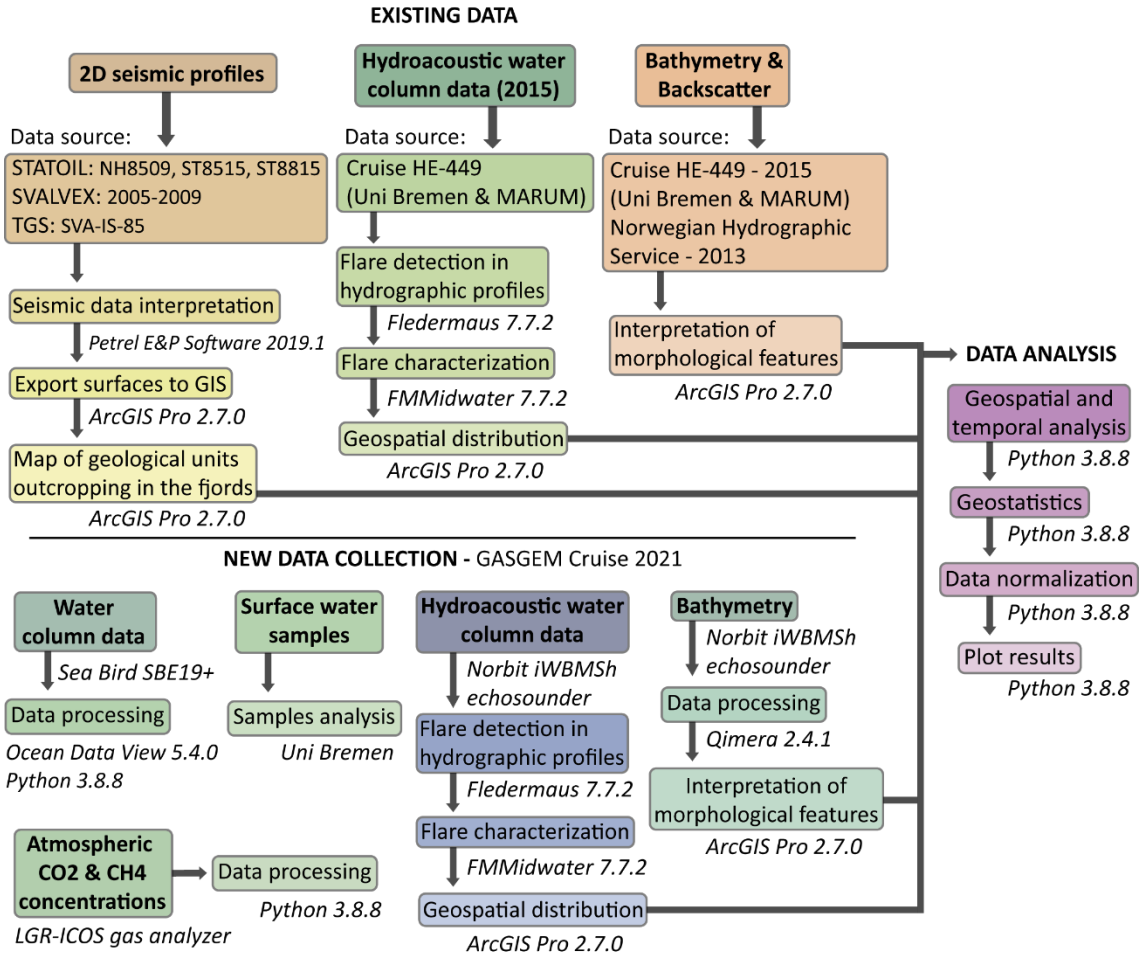

Figure 8. Flow chart explaining the method followed for the realization of this work.

Data type	Location/extent	Comments	Source
Bathymetry and MBES	Isfjorden and tributary fjords, Van Mijenfjorden	200 m resolution, locally 5 m	Norwegian Hydrographic Service, Norwegian Mapping Authority, The University Centre in Svalbard (UNIS), University of Bremen & MARUM
Geological maps	Onshore Svalbard	Mapped at 1:100000 scale in most areas, at 1:250000 in east Svalbard	Norwegian Polar Institute, NPI (2016)
2D Seismic	Isfjorden and tributary fjords, Van Mijenfjorden, Onshore Svalbard	Isfjorden: 47 seismic profiles (1615 km), Van Mijenfjorden: 17 seismic profiles (328.5 km)	STATOIL (surveys NH8509, ST8515 and ST8815), SVALVEX (surveys 2005, 2006, 2007, 2008 and 2009), TGS (survey SVA-VM-85), Bælum et al. (2012), Blinova et al. (2012), Blinova et al. (2013), Roy et al. (2019)
Boreholes	Reindalen	Reindalpasset I (7819/12-1)	Bælum et al. (2012); Roy et al. (2014); Senger et al. (2019)
Gas hydrate stability zone	Isfjorden	Thermobaric conditions, Modeled distribution in Isfjorden (quartile 0.1, 0.5, 0.9)	Betlem et al. (2019); Betlem et al. (2021)
Hydrographic data	Isfjorden 2015 and 2021, Van Mijenfjorden 2015	Isfjorden 2015: 741 km, Van Mijenfjorden 2015: 203 km, Isfjorden 2021: 523.8 km	University of Bremen & MARUM (HE-449 cruise, 2015); This study (GASGEM2021)
Offshore geochemical sampling	Isfjorden	Chemical composition	Liira et al. (2019); Damm et al. (2021)
Seabed morphologies	Isfjorden and tributary fjords		Pockmarks (Roy et al. (2015), Roy et al. (2016), Roy et al. (2019)), Faults (Blinova et al. (2012), Roy et al. (2014), Roy et al. (2015)), Glacial lineations (Roy et al. (2015))
CTD data	Isfjorden, Tempelfjorden, Nordfjorden	16 stations along 4 transects	This study (GASGEM2021)
Water samples	Isfjorden, Tempelfjorden, Nordfjorden, Billefjorden, Sassenfjorden	37 surface samples for hydrocarbon analysis	This study (GASGEM2021)

Table 1: Summary of datasets.

4.1. 2D seismic interpretation

The aim is to define the sub-surface stratigraphical structures forming Isfjorden and Van Mijenfjorden to correlate the methane seepage detected in the water column with the source rocks and, ultimately, find hydrate indicators such as Bottom-Simulating Reflector (BSR).

The seismic interpretations have been made using Schlumberger's Petrel E&P Software Platform v2019.1 and are based on seismic data acquired in multiple seismic surveys. In Isfjorden, the data was acquired by STATOIL (actual Equinor) in the surveys NH8509, ST8515 and ST8815; SVALVEX during the surveys performed in 2005, 2006, 2007, 2008 and 2009; and TGS in the survey SVA-IS-85. In Van Mijenfjorden, the seismic data was acquired by TGS during the survey SVA-VM-85. A total of 47 seismic lines have been interpreted in Isfjorden with a total length of 1615 km. In Van Mijenfjorden, 17 seismic lines have been interpreted with a total length of 328.5 km (Figure 9). The low frequency of the seismic acquisition results in deep penetration and low resolution of the seismic profiles. Consequently, it is possible to interpret reflectors of deep stratigraphic units, but it will be challenging to differentiate anomalies and reflectors on the shallow marine sediments such as potential BSR.

The groups, subgroups and formations interpreted in this work are based on the lithological structure described by Bælum et al., 2012 from the Borehole Reindalspasset I (7819/12-1), located in Reindalen at 78°03'28" N and 16°56'31" E (Senger et al., 2019). Two land-based seismic lines linked the borehole onshore with the seismic profiles in Van Mijenfjorden (Figure 9). Once I had interpreted Van Mijenfjorden's general stratigraphy, I extrapolated the interpreted reflectors to Isfjorden by generating seismic surfaces.

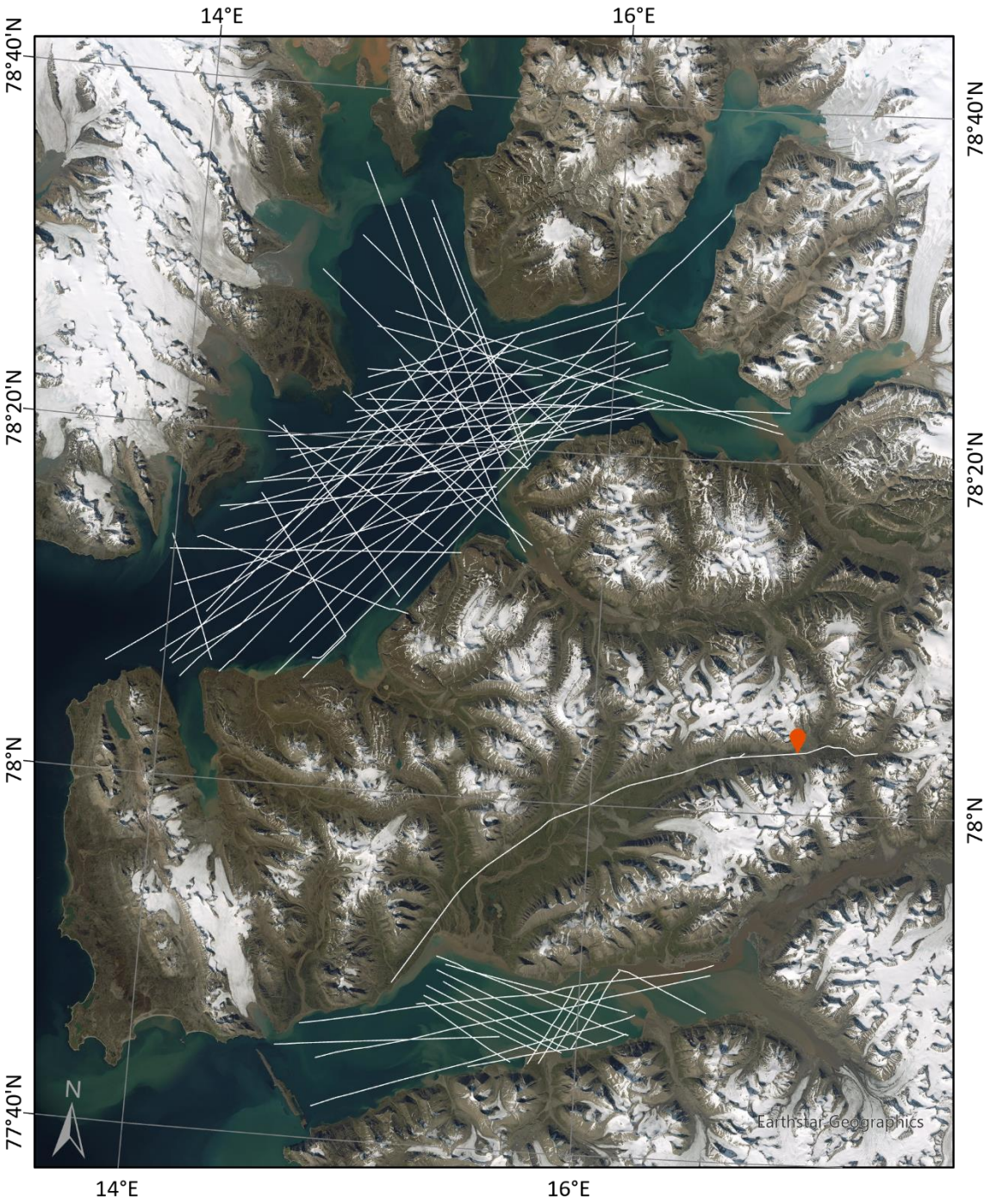

Figure 9. The white lines outline the seismic lines interpreted for this work. The orange dot indicates the geographic location of the Reindalpasset I borehole used to describe the stratigraphic units—satellite image of western Spitsbergen courtesy of Earthstar Geographics.

4.2. Bathymetry and backscatter

The integration of multiple bathymetric datasets has allowed the characterization of different seabed morphologies in the fjords.

In Isfjorden, I received the full seafloor surface morphology coverage of the fjord courtesy of the University Centre in Svalbard (UNIS) in collaboration with the Norwegian Hydrographic Service and the Norwegian Mapping Authority with a 5 m resolution. Moreover, I incorporated the transects covered by the HE-449 cruise onboard R/V Heincke in 2015. The bathymetric information during the HE-449 was acquired with the shallow to mid-water multibeam echosounder Kongsberg EM710 operating at 70–100 kHz to acquire an updated high-resolution bathymetry and backscatter cover of the main trunk of Isfjorden (Figure 10).

Finally, during the GASGEM cruise in June 2021 (https://www.youtube.com/watch?v=VuFjKIMPqt0), we acquired bathymetric data using a NORBIT - iWBMSh high-end turnkey multibeam sonar system, operating at 200-400 kHz. The system operated with an equiangular mode, with a maximum swath angle of 120° in shallow areas and 90° in deeper waters for an optimal depth range of 10-250 m. Sixteen CTDs were performed along the transects to calculate the Sound Velocity Profiles (SVP) that were inserted in the Data Collection Tool (DCT) (©Norbit Subsea). The data logging was in .wbm and .s7k files format, which were further exported and processed using Qimera v2.4.1 (©QPS). In total, we surveyed 523.8 km over the inner part of Isfjorden, Adventfjorden, Tempelfjorden, Billefjorden and Nordfjorden (Figure 10). However, and due to the shallow-water characteristics of the multibeam used, the data acquired was remarkably noisy in the deep parts of the fjords. Consequently, I decided not to incorporate it in the general bathymetric chart.

In Van Mijenfjorden, I worked with the bathymetric cover acquired from the HE-449 R/V Heincke Cruise in 2015, which partly covered the westernmost basin and made two transect lines through the center of the fjord. The acquisition characteristics were the same as those described in Isfjorden during this cruise, which also provided a high-resolution bathymetry and backscatter. Moreover, I also received a bathymetry from the north part and inner part of the fjord with a 10 m resolution grid provided by the Norwegian Hydrographic Service and the Norwegian Mapping Authority (Figure 10).

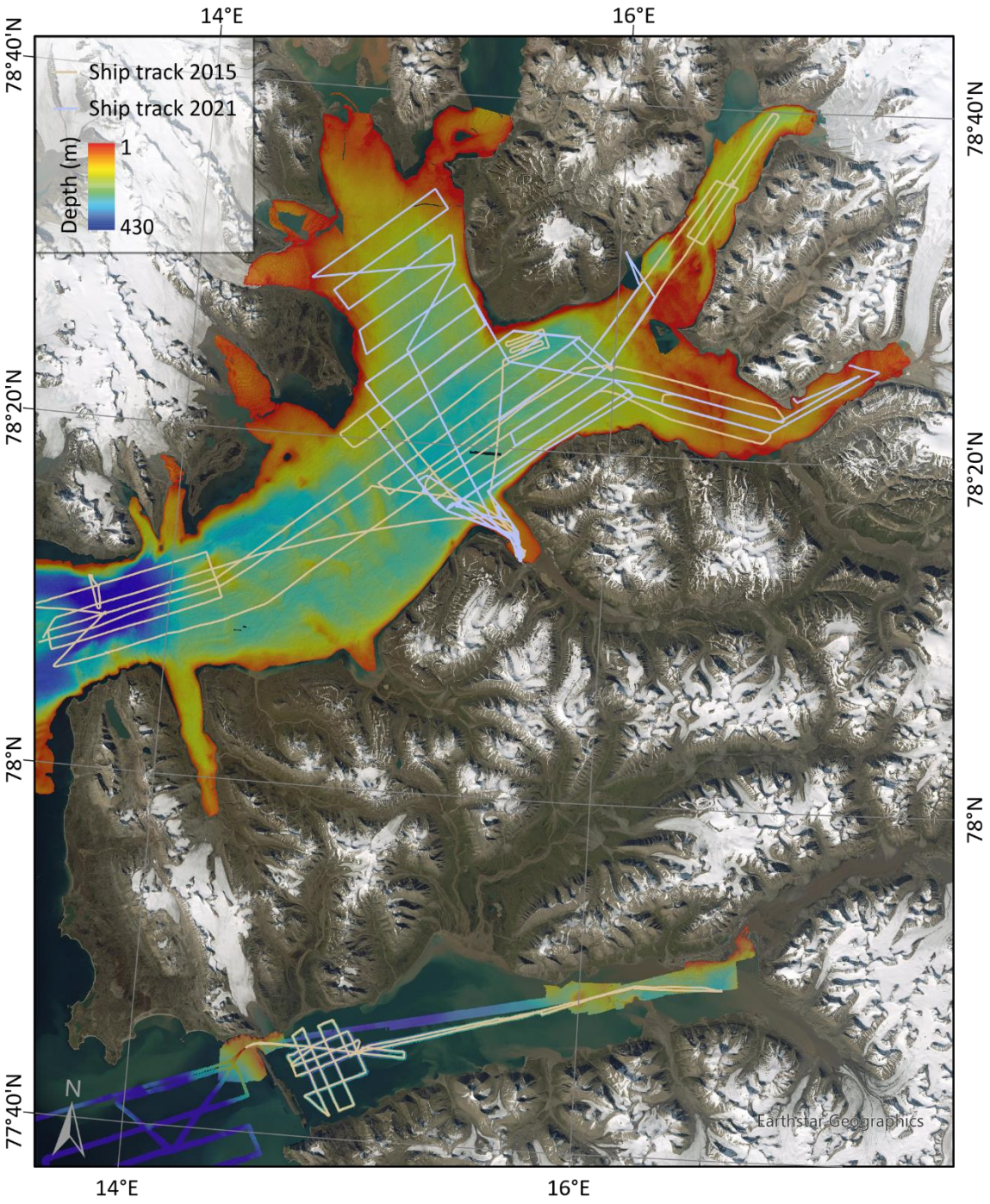

Figure 10. Regional map of western Spitsbergen with the bathymetric surfaces used in this work. Also, the ship tracks that were followed during the HE-446 cruise in August 2015 and the GASGEM cruise in June 2015 for the acquisitions of hydrographic data. The base map is courtesy of Earthstar Geographics.

4.3. Water column imaging

The water column information for the dataset from 2015 was acquired during cruise HE-449, organized by the University of Bremen and MARUM - Center for Marine Environmental Sciences, onboard the R/V Heincke in August 2015. The research vessel was equipped with a multibeam hydroacoustic echosounder Kongsberg EM710 operating at 70–100 kHz, making it an efficient tool to identify and characterize submarine active and passive seepages (Veloso et al., 2015; Mau et al., 2017).

The water column and bathymetric information from 2021 have been acquired during the GASGEM Cruise, organized in collaboration between the University Centre in Svalbard and the General Geology-Marine Geology Group of the University of Bremen, onboard R/V Clione during 1-8 of June 2021. The vessel was equipped with a NORBIT - iWBMSh high-end turnkey multibeam sonar system, which operated at frequencies of 200 (deeper than 200 m) or 400 kHz (shallower than 200 m) for the acquisition of high-resolution hydrographic data.

In both cruises, the swath width acquisition method enabled wide lateral coverage for bathymetric and seafloor backscatter mapping and the detection of high backscatter anomalies in the hydroacoustic profiles attributed to the presence of gas bubbles (acoustic flares).

In the dataset from August 2015, a total of 944 km of water column hydrographic profiles (741 km in Isfjorden and 203 km in Van Mijenfjorden area) were analyzed. For the data acquired in June 2021, 523.8 km of water column hydrographic profiles were acquired in Isfjorden, and no data was acquired in Van Mijenfjorden. The data of both datasets have been analyzed using Fledermaus v7.7.2 tools and the FMMidwater v7.7.2 module (©QPS), employing the FMGeopicking Tool to extract the flare source point data and get the reference information related to the point. To visualize flare deflections and bubble rising heights, selected flares were extracted from the multibeam echosounder's water column records and were edited using the 3D Editor. In addition, the Time Series Tool was used to define and export the flare's intensity values in decibels (dB). The information related to the flare characteristics was exported to Microsoft Excel v2107 for further analysis.

The flare data consisting of information about the flare position and reference in the dataset, nature of the flare (pulsing or continue), its architecture defining traits as rooted to the seafloor, the total height and the body deflection, or the intensity values, were spatially plotted using

ArcGIS Pro v2.7.0 (©ESRI) (Figure 11). This software has been used to grid, visualize and interpret the data.

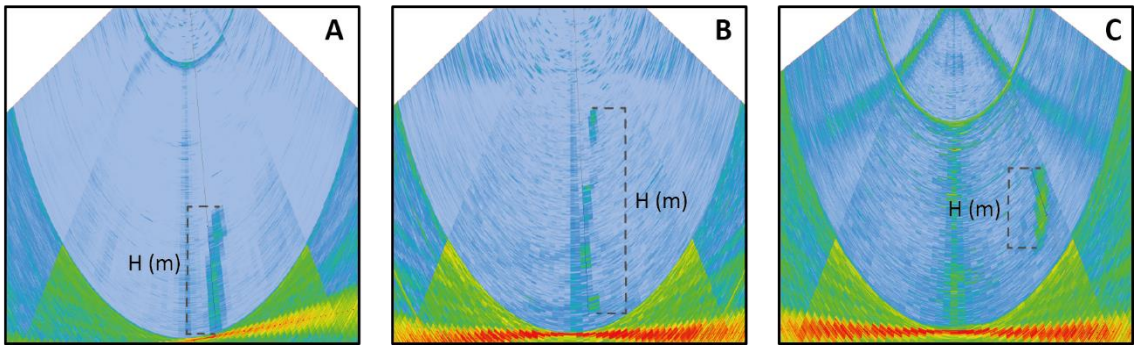

Figure 11. Example of flares with different characteristics: A: Continue, Rooted to the seafloor, H (m) total height, Homogeneous intensity; B: Pulsing, Not rooted to the seafloor, H (m) total height, Decreasing intensity; C: Continue, Not rooted to the seafloor, H (m) total height, Homogeneous intensity.

Due to the multibeam echosounder's limitations, the real width coverage for detecting gas flares is slimmer than the full bathymetric range. Therefore, a calculation of the real footprint for flare identification was required. For doing so, the FMGeopicking Tool was employed to define the flare area's detection boundaries in the hydrographic profiles. The points were spatially plotted using ArcGIS Pro v2.7.0. By measuring the distance in different depths, it was possible to empirically define the footprint's angle: d(D) = 2 (tan(31.864) * D) (Figure 12). Next, the bathymetric values were extracted to the ship track to define the footprint values in each depth and plotted again in ArcGIS Pro v2.7.0 using the Buffer Tool to define the final polygon (Figure 13).

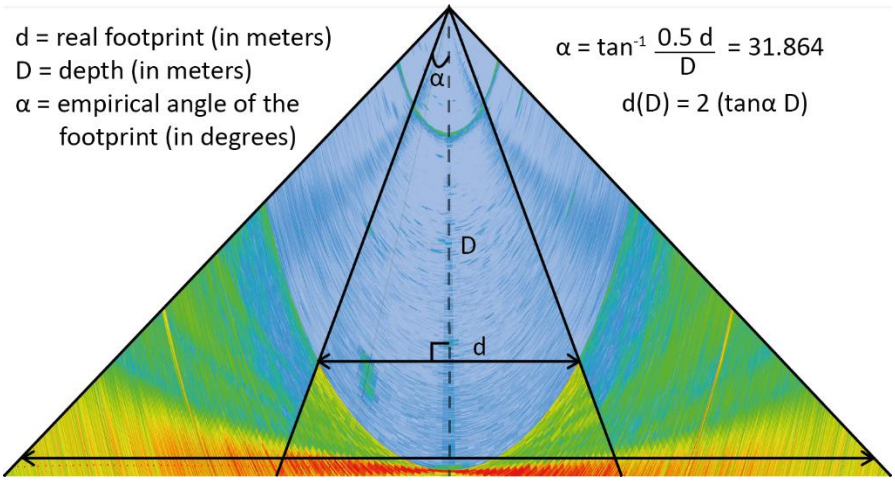

Figure 12. Diagram explaining the method for calculating the real footprint of the hydrographic profiles.

A similar procedure was used for evaluating the flare's footprint. Nevertheless, in this case, each flare had a unique imprint on the seafloor, generating a single polygon for each individual flare. The workflow consisted of identifying the points where the same flare appeared rooted to the seafloor. The FMGeopicking Tool was used for picking the points, which were further plotted in ArcGIS Pro v2.7.0 to define the area and extension of the flare's footprint. However, this is not a precise method for calculating the seepage area because the lateral and temporal resolution of the hydrographic profiles is too low to define the specific area with a square centimeter resolution.

Microsoft Excel v2107 has been used for doing the calculations of the flare characteristics. The statistical analyses were computed using Python v3.8.8. According to the statistical quartiles, the flare's characteristics have been grouped into four categories. The characteristics defined by unique values have been categorized into groups of approximated values.

The geo-statistics and spatial analysis have been programmed with Python v3.8.8, mainly using pandas v1.2.4 and geopandas v0.9.0 for computing and matplotlib v3.3.4 and Cartopy v0.18.0 for plotting. To work with it, I used the open-source web-based user interface, JupyerLab v3.0.14. The code is available in Appendix 3.

Geographical visualization, statistical analysis and data georeference have been performed using ESRI ArcGIS Pro v2.7.0. This method has helped to make a detailed comparison of the flare distribution with the fault system, the outcropping geological sequences, and the pockmark distribution in Isfjorden.

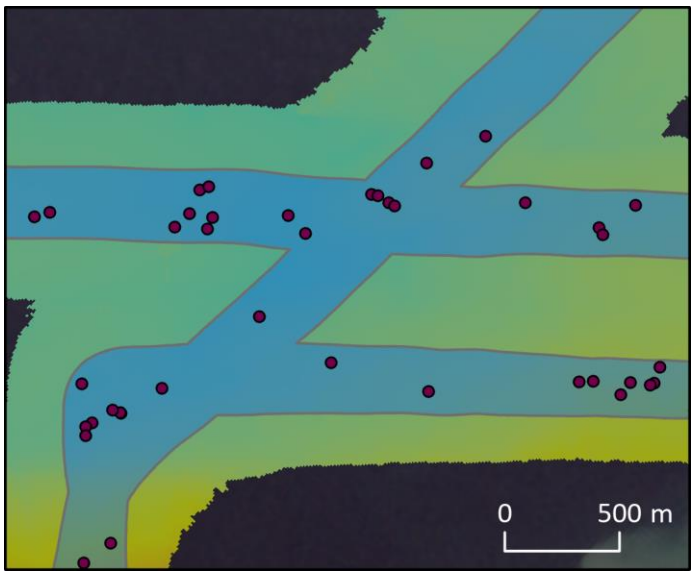

Figure 13. Image of detail comparing the bathymetry swath (green-yellow) with the real footprint (light blue). The red dots are the flares located inside the real footprint area.

4.4. Hydrographic data

Profiles of salinity and temperature in the water column were obtained using a Conductivity-Temperature-Depth (CTD) system during the GASGEM cruise in June 2021. The instrument used was a Sea-Bird SBE19+. A winch with a meter counter wheel was used when lowering the CTD through the water column. The data was processed and visualized using the programming language Python v3.8.8 and Ocean Data View v5.4.0 (ODV; Schlitzer, Reiner, Ocean Data View, https://odv.awi.de). The interpolations between the data points were done in ODV using the weighted-average gridding feature.

A bucket was used to collect a total of 37 discrete surface water samples over the fjords. It was the less invasive method since we avoided large turbulences and bubbles, which could influence the dissolved gases in the water. Once on deck, we rinsed a 100 mL glass vial 3 times, and after filling it with the surface water, we crimped it with aluminum caps trying not to generate any bubbles. Afterwards, we injected 1 mL of NaOH (1M) with a syringe through a self-sealing membrane to stabilize the sample from any biological activity. Finally, we stored the samples up-side-down in a cold and dark environment. Hence, we collected 37 discrete seawater samples over the fjord's surface that were sent to the University of Bremen (Germany) to analyze methane concentrations.

4.5. Geostatistical analysis

To perform the geostatistical analysis of the geospatial data, I have used JupyerLab v3.0.14, an open-source web-based user interface for data science. Pandas v1.2.4 and geopandas v0.9.0 have been the main packages I used to make the data analysis, and I used matplotlib v3.3.4 to plot the results and make figures.

The analysis of the data has required three different workflows:

1. Nearest neighbour between two point datasets: The nearest neighbour analysis aims to find the closest geometry to another geometry feature. In this case, I was looking for the closest distance between two point datasets (Figure 14) (Code in Appendix 3.1). In the data, I calculated the distance between flares and pockmarks, and to normalize the data, I also calculated the distance from the ship track to pockmarks.

2. Nearest neighbour between a point and a line/polygon: Calculating the nearest neighbor between a point and a polygon is not evident because the closest distance needs to be defined to a geometry formed by multiple coordinate points (Code in Appendix 3.2). With the closest distance to the polygon, I created bins of data at the same distance from the polygon. An example is the flare and ship track point distribution with respect to the coastline. To present the results, I made a bin of the data to have the percentage of flares distributed in groups of 1 km from the coastline.

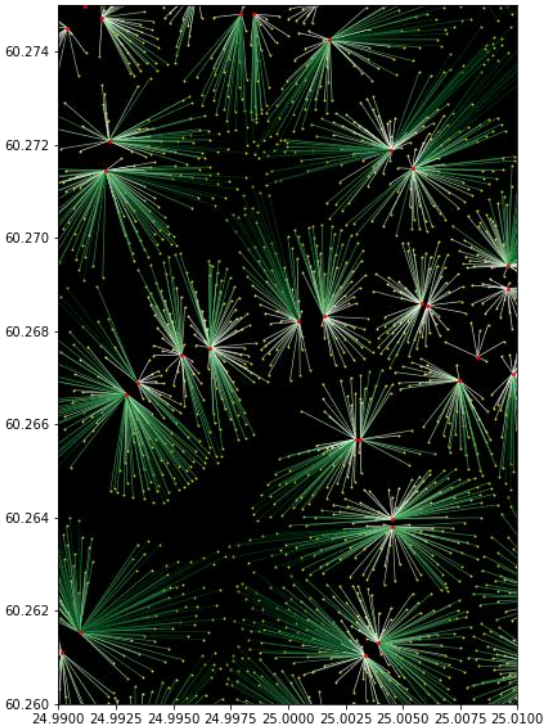

Figure 14. Nearest neighbour schematic model taken from the autogis-site developed by Henrikki Tenkanen & Vuokko Heikinheimo (University of Helsinki). It shows the links between point features (yellow dots) to the closest ending feature (red dots).

3. Point in Polygon intersection: It consists of finding out if a certain point is located inside or outside an area (Figure 15). In this case, I compared the flare and ship track distribution inside each one of the areas for the geological groups, subgroups and formations outcropping in the fjords (Code in Appendix 3.3). Because different polygons formed one geological unit, I had to merge them into a single multipolygon. Furthermore,

creating a loop has accelerated the calculation of the data. Finally, to normalize the flare data distribution, I correlated the percentage of flares inside each geological unit, which we normalized with the ship track.

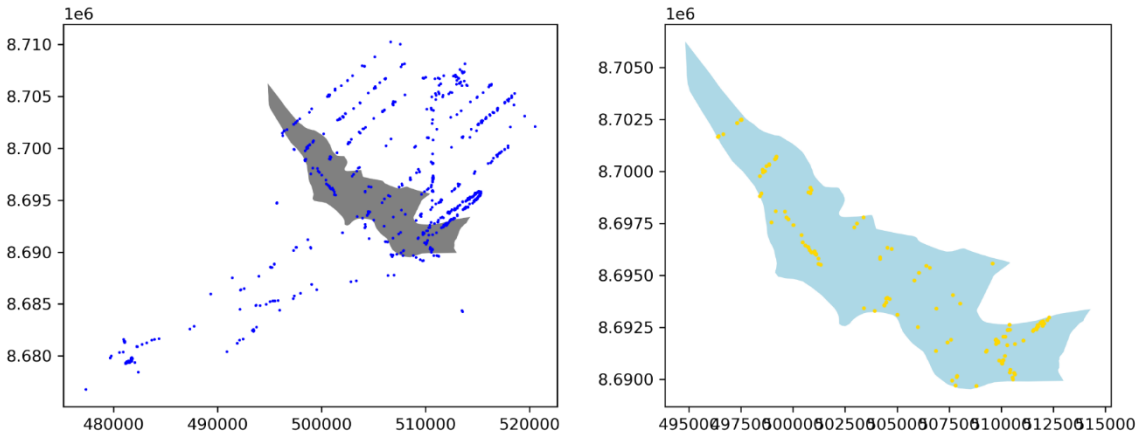

Figure 15. Explanatory visual model of the method used to calculate the points within a polygon applied for the flares detected in the 2015 dataset and the outcrop area of the Kapp Toscana Group.

5. RESULTS

5.1. Subsurface geology and stratigraphy of the fjords

The 2D-seismic interpretation of the 47 profiles in Isfjorden and 17 profiles in Van Mijenfjorden based on the description of the Reindalpasset borehole (Bælum et al., 2012) as a reference, has enabled mapping the major stratigraphic elements outcropping in the fjords.

In Isfjorden, the units form a large syncline with an almost vertical outcropping angle on the western side and a lower angle (~10°) towards the east (Figure 16). I interpreted the major groups: Van Mijenfjorden Group (250 km^2), Adventdalen Group (690 km^2), Kapp Toscana Group (275 km^2), Sassendalen Group (335 km^2), Tempelfjorden Group (225 km^2) and Gipsdalen Group (390 km^2) (Figure 17).

As part of the Adventdalen Group, I could differentiate the boundaries of the Janusfjellet Subgroup (490 km^2), which is represented by large thickness variations caused by folding and related to compressional tectonics from the Paleogene. Janusfjellet Subgroup is further subdivided into the Agardhfjellet Formation and Rurikfjellet Formation (Maher Jr, 2001).

The Agardhfjellet Formation is of high interest in this study due to its potential as a source rock. That is why I tried to define its stratigraphic limits. However, the seismic data showed blurry reflectors on the upper boundary of the formation. Consequently, the limits have been extrapolated and described based on the layer's thickness outcropping onshore and from exploration well holes. On the south coast of Isfjorden, it has been assumed a mean thickness of 350 m with a sound travel velocity of 1700 m/s, defining a reflector 400 ms in two-way travel time (TWT) above the reflector defining the top of Kapp-Toscana Group. In the central part of the fjord, I assumed a mean thickness of 220 m (260 ms in TWT), and in the northern part of Isfjorden, I assumed a thickness of 90 m (100 ms in TWT). The total outcropping area of the formation in the fjord is 80 km^2 (Figure 17).

In Isfjorden, I also defined the lower limits of Botneheia Formation, the youngest unit of the Sassendalen Group. Botneheia presents a changing thickness of 80 m (95 ms in TWT) in the southern part of Isfjorden and 180 m (210 ms in TWT) in the northern part of the fjord. It is also a primary unit of interest in our study for its hydrocarbon potential. It outcrops over 195 km^2 in the inner part of Isfjorden (Figure 17).

The seismic lines I used only covered the inner part of Isfjorden, which is why the unit boundaries in the upper coast, Nordfjorden, Billefjorden, Tempelfjorden and the mouth of Isfjorden, were interpreted following the general stratigraphical trends and the geology onshore. Consequently, they are considered as areas of uncertain interpretation (Figure 17).

In Van Mijenfjorden, the stratigraphy of the syncline and the fjord's general structure make the Van Mijenfjorden Group and Adventdalen Group outcrop in almost the full extent of the fjord, covering 260 km^2 and 210 km^2, respectively. The Janusfjellet Subgroup (60 km^2), Kapp Toscana Group (12 km^2), Sassendalen Group (25 km^2) and Tempelfjorden Group (2.5 km^2) outcrop in the western part of the fjord (Figure 17). I have designated the interpretations in the inner-most and outer-most parts of the fjord as uncertain since the seismic data that I used does not cover those areas. Nevertheless, the onshore geology gives explicit hints of the units outcropping. Moreover, it has not been possible to discern the reflectors defining the boundaries of the Agardhfjellet and Botneheia Formations.

No Bottom-Simulating Reflector (BSR) has been identified in the seismic profiles. Finally, the faults defined in Isfjorden are from the interpretations of Blinova et al., 2012 and Roy et al., 2015.

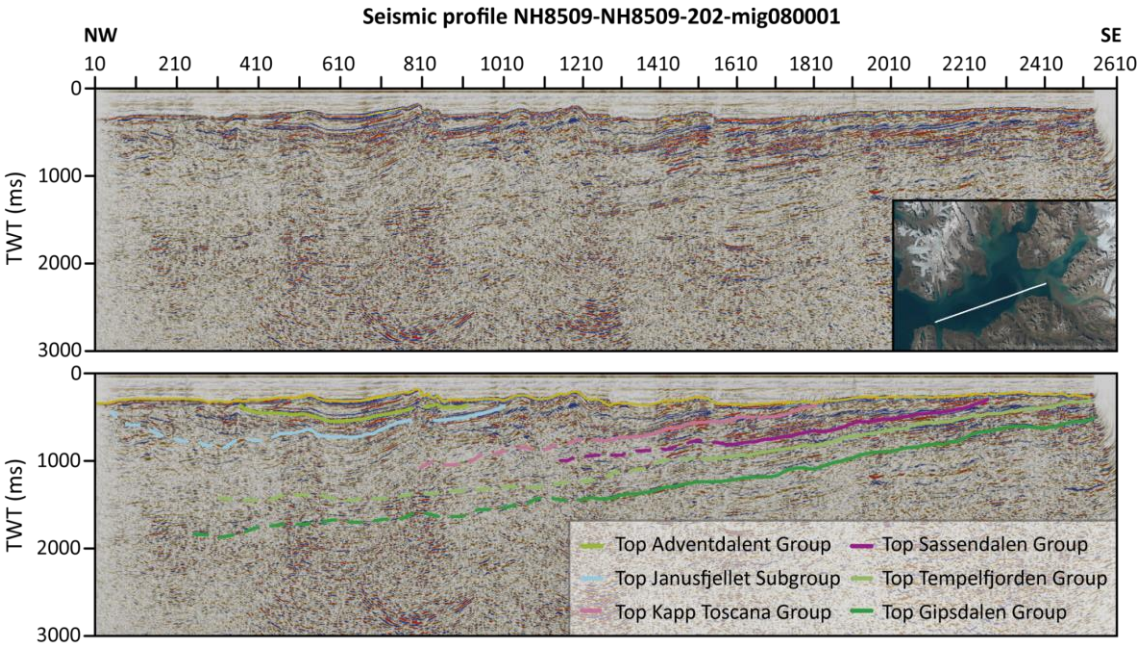

Figure 16. Interpretation of the seismic profile NH8509-NH8509-202-mig080001 crossing the main trunk of Isfjorden. The seismic profile is a central section of Isfjorden, and it is representative of the structures that are present on all profiles. It has a vertical exaggeration x10. The map shows the outline of the line in the regional setting of the fjord.

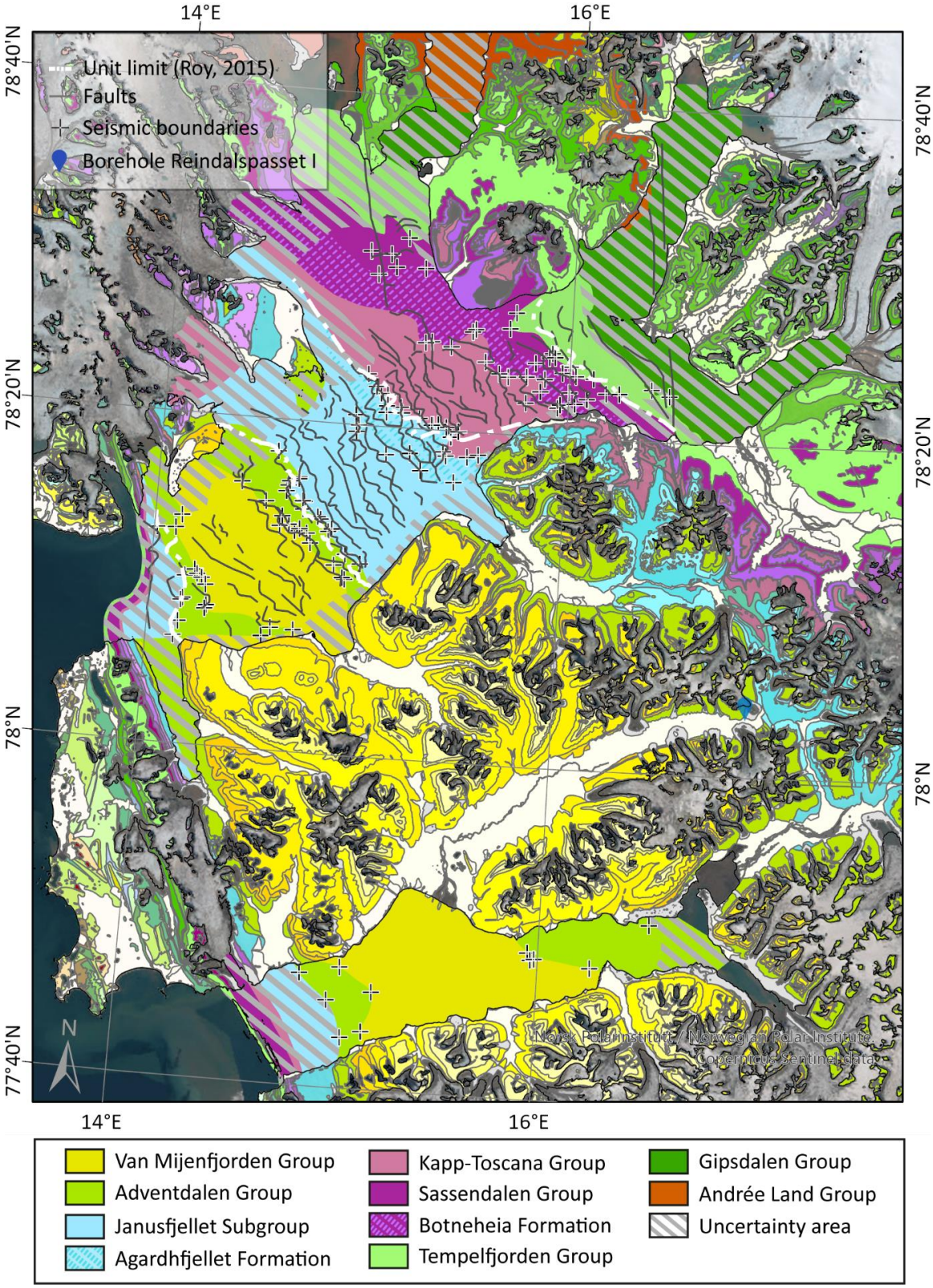

Figure 17. Geological map of western Spitsbergen. The onshore geological information is courtesy of the Norwegian Polar Institute (NPI). The stratigraphic units outcropping in the fjord are the result of the interpretations of the seismic profiles. In shredded are the areas interpreted based on the geological setting onshore. In blue is the location of the Reindalpasset I borehole. In Isfjorden, are shown the stratigraphic boundaries (Blinova et al., 2012; Roy et al., 2015) and the faults described by Roy et al., 2015.

5.2. Seabed morphologies and backscatter

The outer part of Isfjorden is occupied by Paleogene rocks surrounded by outcrops of Jurassic-Cretaceous strata (Blinova et al., 2012). The seafloor relief is characterized by parallel ridges and troughs in the NW-SE direction (Figure 7). These show a correlation between the depth values and the backscatter intensity. The shallow part of the ridges is characterized by high backscatter values, while the troughs have low backscatter values.

Most of the onshore extension of Van Mijenfjorden is constituted by seven different formations of Cenozoic clastic infill, which are grouped under the name Van Mijenfjorden Group (Harland, 1969). Mesozoic strata cross the western-most part of the fjord. The bathymetry presents low-backscatter values for most of the extension, except for a deep basin located in the west part of the area covered, which presents high backscatter values.

5.3. Hydroacoustic flare characterization and distribution

The gas flares have been detected by a multibeam echosounder as acoustic anomalies in the water column appearing in successive hydrographic profiles. A criterion used to differentiate gas flares from other anomalies, such as fish schools, is that the water's anomaly has to present a constant upward movement over time, as do the gas bubbles in the water column.

5.3.1. Dataset August 2015

In Isfjorden, 668 flares were detected over an area of 176 km^2, and 115 flares were identified in Van Mijenfjorden over an area of 20 km^2 (Figures 18, 19).

The flares identified in the hydroacoustic data were registered in water depths between 30.3 and 278.4 m in Isfjorden, being 193.7 m the depth with the highest flare concentration (median) (Appendix 1 Table 8). In Van Mijenfjorden, gas flares were registered in water depths between 30.7 and 116.4 m, being 108 m the median depth value with the highest flare concentration and 98.2 m as a mean value (Appendix 1 Table 8). The footprint of the flares has a mean value of 90 m^2, with values going from 2 m^2 to 458 m^2.

In Isfjorden, the flares' height values range between 1.2 and 192.2 m above the seafloor, with a mean height value of 42.8 m and a median value of 37.2 m. The shallowest depth reached by a recorded flare is 18.5 m, and the average value for the dataset is 117 m.

The intensity values of the flares in Isfjorden ranges between -80 and -5 dB. The intensity value for the first quartile is -60 dB and -45 dB for the third quartile. The median value of the flares is -55 dB.

In Van Mijenfjorden, the flares' height ranges from 0.9 m to 69.7 m above the seafloor, with a mean height value of 21.4 m and a median value of 18.5 m. The shallowest depth reached by a recorded flare is 5.8 m, but the average value is 61.1 m depth.

The intensity values for the flares in Van Mijenfjorden ranges between -75 dB and -25 dB. The intensity value for the first quartile is -60 dB and -40 dB for the third quartile. The median value of the flares is -50 dB.

Error of the dataset

The dataset's error has been calculated based on the data previously interpreted by Dr. Miriam Römer and the interpretation for this work by Nil Rodes.

The previous interpretation of individual seepage in Isfjorden was a total of 691 flares, while the author has only identified 668 flares. In Van Mijenfjorden, the prior interpretation detected 70 individual flares along the fjord, and the author identified 115 flares.

For the flares that coincide in both interpretations, the average distance between them in Isfjorden is 5.5 m, with a minimum distance of <1 m and a maximum distance of 41 m. In Van Mijenfjorden, the average distance between flares is 4.3 m, with a minimum distance of <1 m and a maximum distance of 23 m between flares. These differences are probably the result of picking the first or the last sign of the flare in the hydrographic profiles since there are flares up to 22 m long.

In the author's interpretation, no double counting of flares has been done in neither of the fjords.

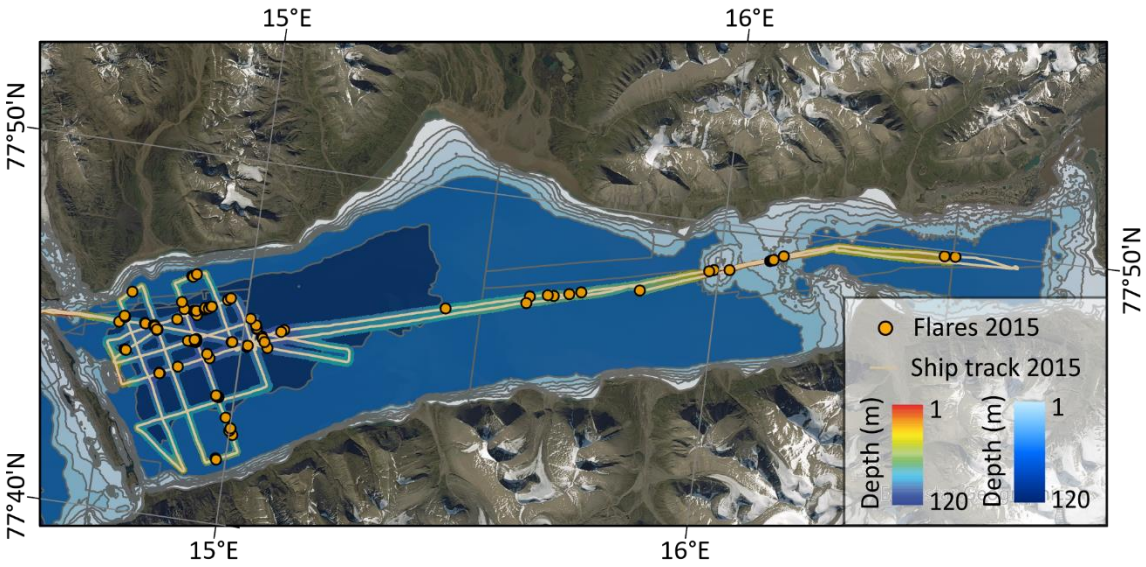

Figure 18. Flare distribution in Van Mijenfjorden over of the bathymetric relief. EPSG:32633 projection and base map is courtesy of Earthstar Geographics.

5.3.2. Dataset June 2021

In the dataset acquired in June 2021, a total of 152 gas flares have been identified over an area of 110 km^2, seeping from the seabed in the inner part of Isfjorden, Tempelfjorden, and Nordfjorden (Figure 19). The flares have been found in a depth range between 13 and 232 m, being 66 m the depth with the highest flare concentration (median) (Appendix 1 Table 8).

The size of the flares detected in June 2021 ranges between 3.52 m for the smallest flare and 44.9 m for the largest flare. The average size is 16.1 m. In this dataset, flares have been detected reaching the water surface. Due to time limitations, I did not obtain the intensity information for the flares.

Error of the dataset

The author has interpreted the hydrographic profiles from the 2021 dataset, and there is no other interpretation. Consequently, it is not possible to make a comparison and calculate the error of the dataset. No double counting of flares has been done in the 2021 dataset.

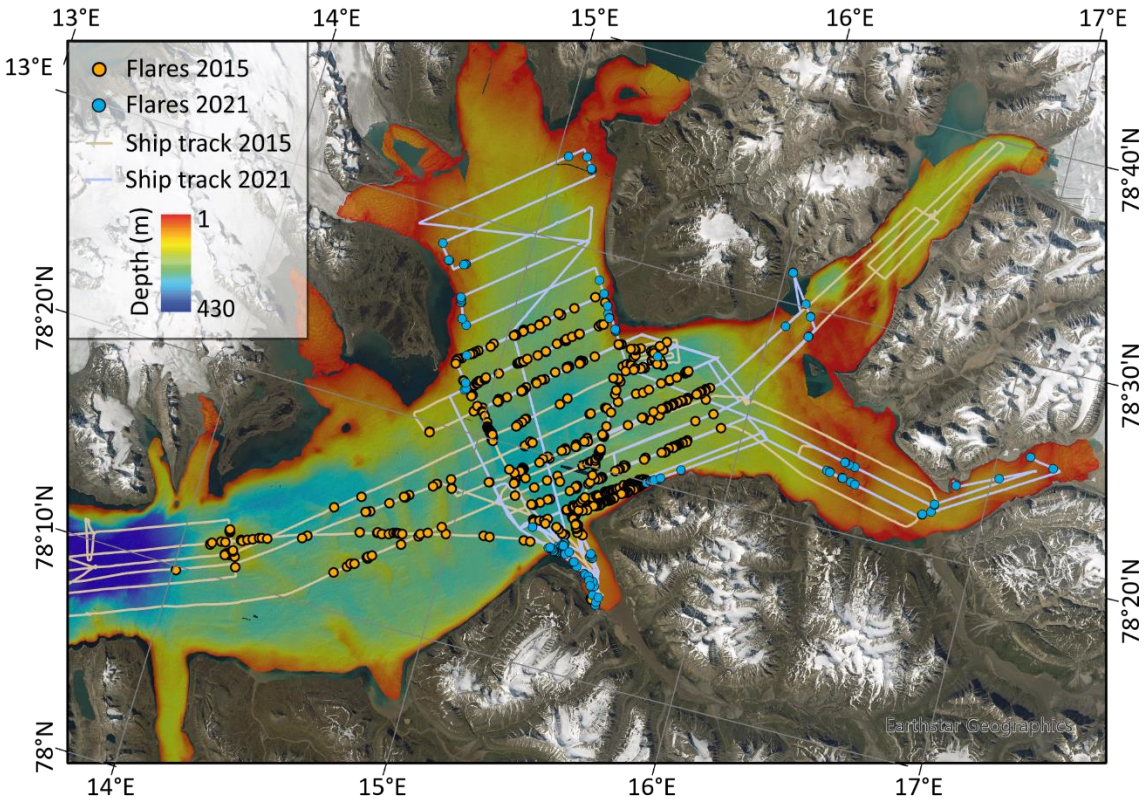

Figure 19. Flare distribution in Isfjorden on top of the bathymetry. In yellow are the flares interpretations along the transect lines of the 2015 dataset. In blue are the flares interpretation and the ship track from the 2021 dataset. EPSG:32633 projection and the base map is courtesy of Earthstar Geographics.

5.4. Hydrographic data

The water column's temperature, salinity, and oxygen characteristics acquired over 16 CTD profiles distributed in 4 main transects present similar values in the south Isfjorden, inner Isfjorden and Nordfjorden transects and vary in the Tempelfjorden transect (Figure 20). The temperature values ranged between 1 and 0°C in the south Isfjorden transect and the inner Isfjorden transect over the entire water column. In Nordfjorden, the surface water temperature was between 1.5-2°C. The temperature profiles in Tempelfjorden ranged from 1.5-2°C on the surface waters to <-1°C in the deeper parts of the fjord. The salinity was similar in the surface waters of the south and inner Isfjorden and Nordfjorden transects, with values ranging 34.3-34.4 psu. In deeper waters, inner Isfjorden presented the lowest salinity values (34.4-34.5 psu). Nordfjorden and south Isfjorden transects present similar values in deep waters (34.55-34.7 psu). Finally, the salinity profile in Tempelfjorden shows a large variability with low salinity values in the surface (<31 psu) and saline values in the deep waters (34.65 psu). The oxygen levels were

similar in most fjords, ranging between 1 and 3 O2_v. In some stations of the south Isfjorden transect, we got some measurement errors.

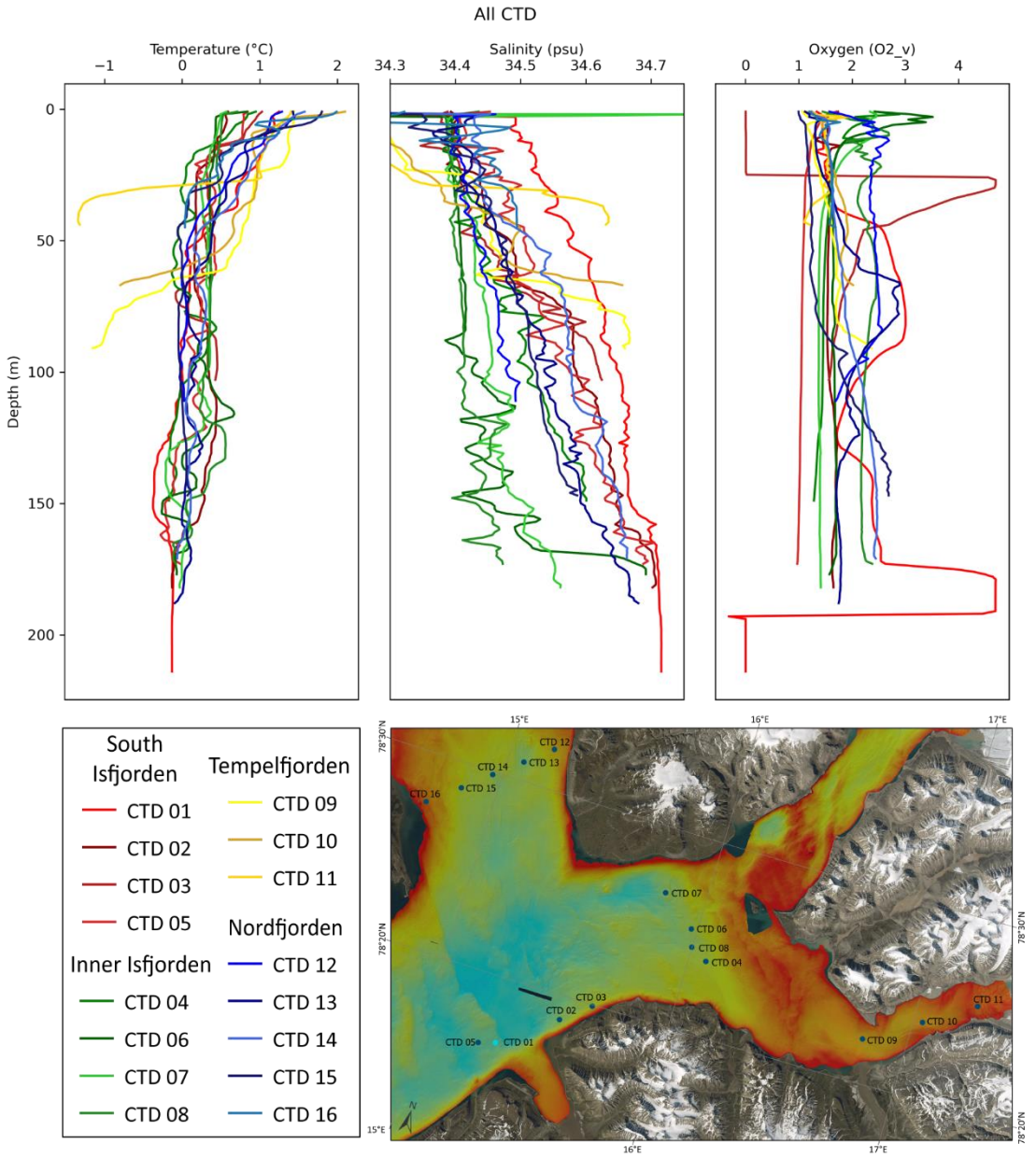

Figure 20. Temperature, Salinity and Oxygen plots of the 16 CTD acquired in the study area. The profiles were divided into 4 main transects—Appendix 2 for the individual plots of each station.

5.5. Geostatistical analysis

The ship track made during the hydroacoustic data acquisition did not cover the totality of the fjords, and both the range of depth covered and the distance to the coast are not even.

Therefore, it has been necessary to normalize the results and adjust the data measured during the transects to see if there are statistically significant distribution anomalies.

For example, in the 2015 dataset, 20% of the ship track covered areas distanced 6-7 km from the coastline, while it only sailed 5% of the transects 7-8 km from the coast. Consequently, and assuming an equal distribution of flares in the fjord, we should expect four times more flares in the 6-7 km bin than in the 7-8 km only from the difference of area covered during the research cruise. This normalization method of adjusting different values to a common scale helps us identify irregularities in the distribution of the values.

For the data acquisition in June 2021, we used a high-resolution multibeam meant for shallow waters. The deepness of some areas, the bad weather days, and the instrument limitations made different data qualities, which I grouped by confidence depending on the depth ranges. Below 200 m depth, the results have very low confidence as a consequence of the background noise. Between 200 and 175 m, the resolution depended on the sea conditions while acquiring the data but still presented low confidence results. The depths between 175 and 150 m have a better resolution. Nevertheless, sometimes there is some noise, which could alter the results, adding some uncertainty. Finally, there is strong confidence in the data acquired above 150 m depth and its results since the echograms above this depth are clear. Consequently, to normalize the results from 2021, I used the high confidence data, which only considers the values shallower than 150 m.

5.5.1. Isfjorden 2015

Comparing the 2015 flare distribution to the coastline in Isfjorden, there is a high density of flares in the bins 1-2 km, 2-3 km and 6-7 km from the coastline with 96 (14.4%), 95 (14.2%) and 111 (16.6%) flares respectively. These are also the bins more highly covered by the ship track (14.9%, 21.4% and 20.9%, respectively). The lowest flare occurrence is distributed in the most distant bins from the coastline, with 14 flares in the 10-11 km (2.1%) and 3 flares further than 11 km from the coast (0.4%). However, the ship track coverage was minimal over these areas, representing 0.6% of the ship track in the 10-11 km bin and 0.2% of the ship track in distances >11 km from the coast. The distance bins 3-4 km, 4-5 km and 5-6 km were covered more or less evenly, representing around 8% of the ship track each. The normalization of the flares with the ship track shows higher flare concentrations in the closest bin to the coast (0-1 km), representing 9.7% of the total value, and the bins further from the coast: 7-8 km with 10.2%, 8-9 km with 7.7%, 9-10 km with 8.7%, 10-11 km with 19.8% and >11 km with 13.7% (Appendix 1 Table 5).

The distant bins from the coast concentrate the lowest absolute number of flares. However, they present the highest percentage of normalized flares. The reason for it is that these are also areas with the lowest ship track cover. Furthermore, the distance bins with the highest absolute number of flares are the ones with the lowest percentage of normalized values as a result of the high area covered by the ship track. Nevertheless, in the 7 km closest to the shore, there is a regular percentage of normalized flares of around 5% for each bin, except for the first km, which has a value close to 10% of the normalized values. The distances between 7 and 10 km from the coast present values higher than 7.5% of the normalized flares, and the bins further than 10 km have much higher percentages (Figure 21).

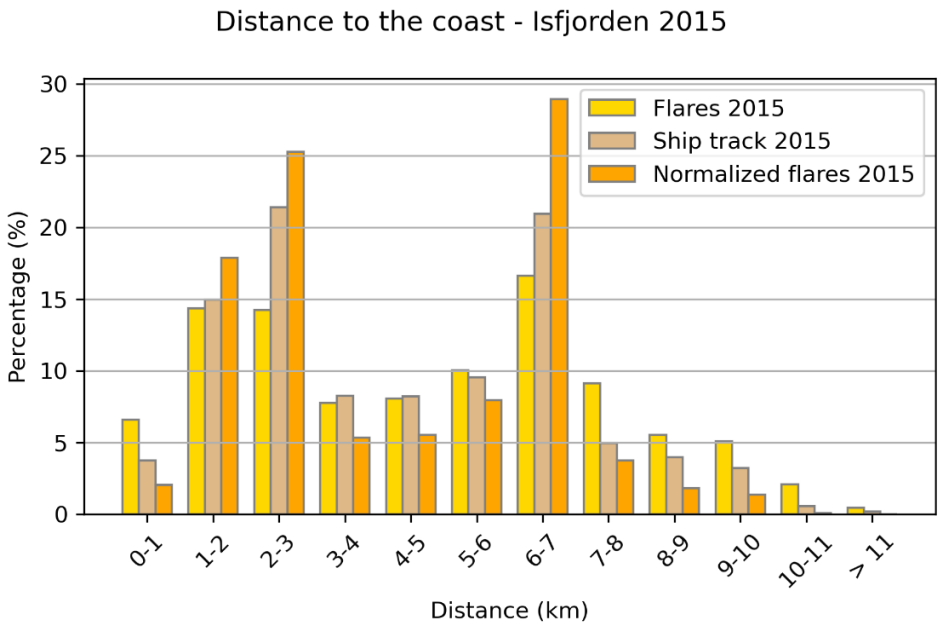

Figure 21. Bar chart of the percentage of flares, ship track and normalized flares divided in 1 km distance bins from the coastline in Isfjorden for the 2015 dataset.

The depth distribution of the 2015 flares shows that the majority of the flares are found below 100 m, except for 2 flares located 30-40 m, 1 flare in 70-80 m and 1 flare in 80-90 m deep. The highest flare congregations are located in 170-180 m, 180-190 m and 190-200 m, accounting for 8.1%, 9.9% and 10.7% of the flares, respectively. However, when normalizing the results with the ship track distribution, we find the highest concentration of flares in 100-110 m, 110-120 m and 190-200 m, with 9.3%, 8.2% and 9.4% of the flares, respectively. Between 140 and 260 m, there is a homogeneous concentration of approximately 6% of the flares for each depth bin (Figure 22) (Appendix 1 Table 8).

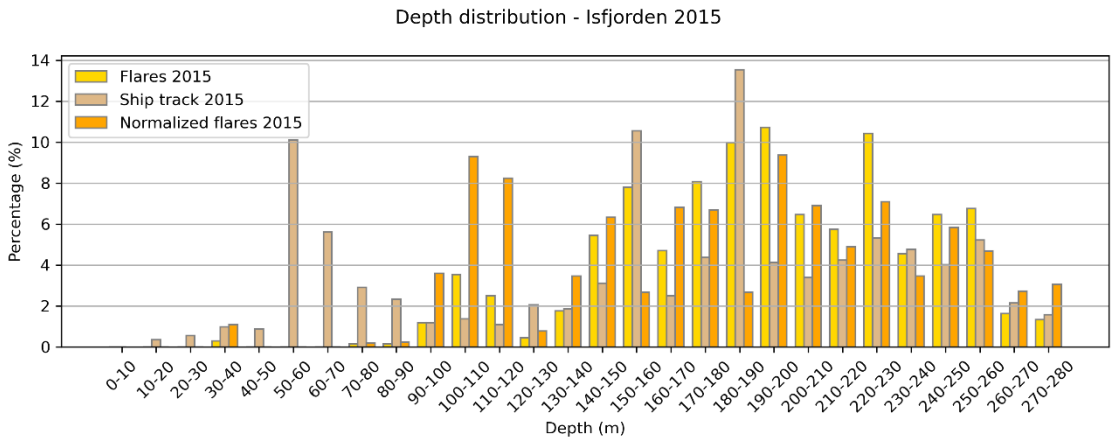

Figure 22. Bar chart of the percentage of flares, ship track and normalized flares organized by depth ranges in Isfjorden for the 2015 dataset.

Based on the seismic-well tie interpretations, I defined the areas in which different geological groups, subgroups and formations outcrop in the fjords.

In the 2015 dataset, there is a very different distribution between the number of flares inside each geological unit and the ship track. The ship track from 2015 in Isfjorden covers all the units outcropping in the fjord, being Tempelfjorden Group (22,4%) and Gipsdalen Group (28,9%) the ones with higher coverage. However, no flares were distributed above these geological groups. Instead, the flares are concentrated in the center of the fjord, in the areas where the Agardhfjellet Formation (19,3%), Kapp Toscana Group (45,9%) and Botneheia Formation (10,6%) outcrop. The percentage of the ship track coverage for these geological units only represents 4,3%, 11,7% and 4,4%, respectively. When normalizing the flare data with the ship track, Agardhfjellet Formation (29.1%) and Kapp Toscana Group (25.6%) stand out as the outcropping units with the highest flare concentration, followed by Botneheia Formation (15.9%) and Van Mijenfjorden Group (11.1%) (Figure 23) (Appendix 1 Table 2).

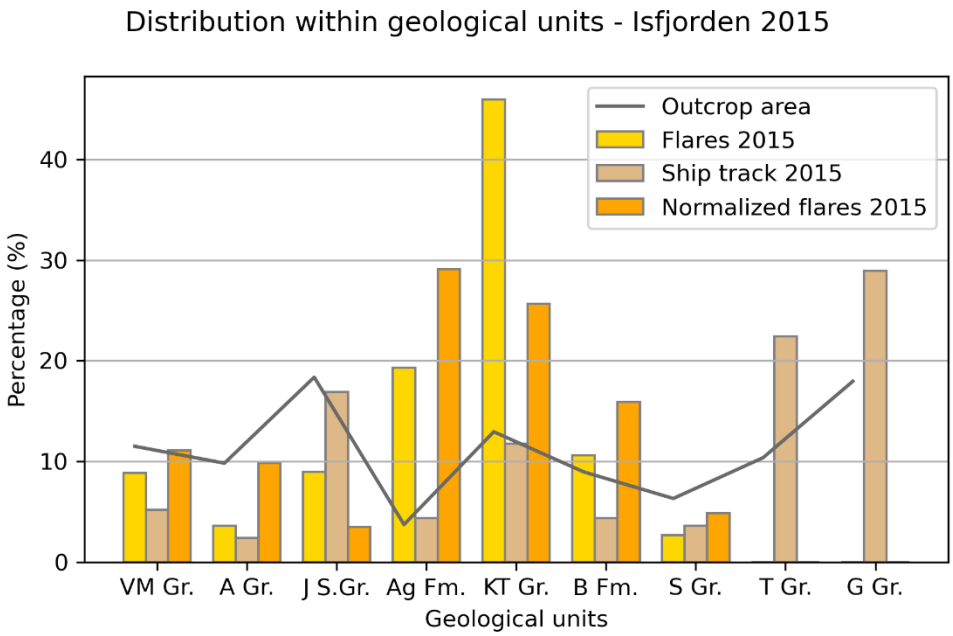

Figure 23. Bar chart of the percentage of flares, ship track and normalized flares within each stratigraphic unit (youngest to oldest from left to right) in Isfjorden for the 2015 dataset. VM Gr. stands for Van Mijenfjorden Group, A Gr. stands for Adventdalen Group, J S.Gr. stands for Janusfjellet Subgroup, Ag Fm. stands for Agardhfjellet Formation, KT Gr. stands for Kapp Toscana Group, B. Fm. stands for Botneheia Formation, S Gr. stands for Sassendalen Group, T Gr. stands for Tempelfjorden Group and G Gr. stands for Gipsdalen Group. The line shows the percentage of area that each geological unit represents in the fjord.

5.5.2. Van Mijenfjorden 2015

The flare dataset from Van Mijenfjorden compared with the coastline shows that the highest percentage of flares is located in the bins 2.5-3 km (23.5%) and 3-3.5 km (17.4%) from the coast, with a ship track cover in these areas of 8.1% and 10.3%, respectively. The highest percentage of ship track cover (41.8%) is located in the 4.5-5 km bin, which only gathers 11.3% of the flares. All this is reflected in the normalized values, showing that the 2.5-3 km and 4-4.5 km bins have the higher flares/ship track ratio with 22.4% and 19.1% of the total, respectively, followed by the bin 1-1.5 km (15.6%) and 3-3.5 km (13.1%). The areas closer than 1 km to the coastline do not present any flares, and the bins of distance 3.5-4 km and 4.5-5 km have the lowest values (2.7% and 2.1%, respectively) (Figure 24) (Appendix 1 Table 7).

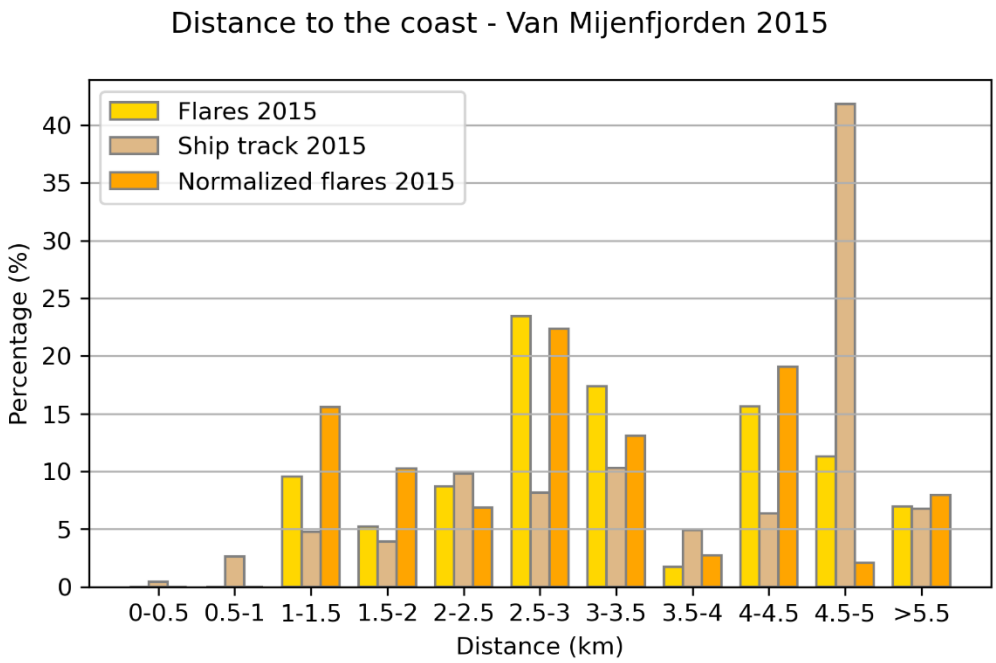

Figure 24. Bar chart of the percentage of flares, ship track and normalized flares divided in 500 m distance bins from the coastline in Van Mijenfjorden for the 2015 dataset.

In Van Mijenfjorden, there are 81 flares (72.3%) below 100 m depth. However, this uneven flare distribution in deep areas coincides with the ship track cover in the fjord, which also covered 72.3% of the transects below 100 m. Nevertheless, the flare values normalization regarding the ship track shows different trends. In this case, there is a peak of flares between 30 and 40 m deep, accounting for 27.7% of the total. Below that depth, there are barely any flares until 70 m, where 22.7% of the flares are concentrated. Beyond 80 m, the depth bins congregate around 10% of the flares each (Figure 25) (Appendix 1 Table 8).

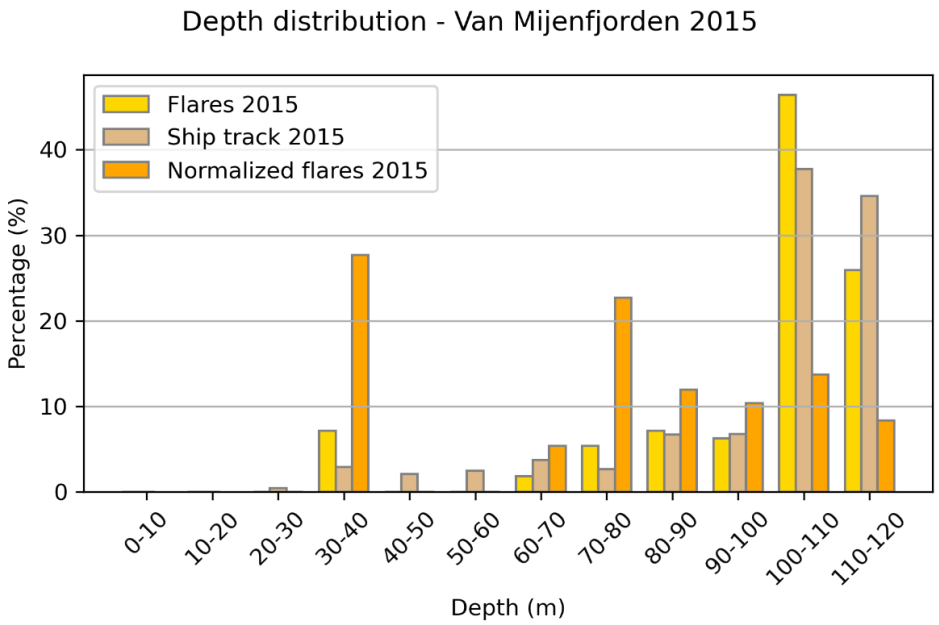

Figure 25. Bar chart of the percentage of flares, ship track and normalized flares organized by depth ranges in Van Mijenfjorden for the 2015 dataset.

When interpreting the geological units outcropping in Van Mijenfjorden, it has not been possible to differentiate the organic-rich formations from their general geologic groups and subgroups. Therefore, Agardhfjellet Formation is included as part of the Janusfjellet Subgroup and Botneheia Formation as part of the Sassendalen Group.

The comparison of the data acquired in 2015 with the interpretation of the geological units outcropping in Van Mijenfjorden shows different trends for each geology. Van Mijenfjorden Group represents the 50.5% outcropping in the fjord. However, only 8.8% of the total ship track covered it, identifying 6.9% of the total flares. Adventdalen Group covers 30% of the fjord, and the track coverage over this geological unit was 41.6%, identifying 22.6% of the total flares. Nevertheless, more than two-thirds of the flares (67.8%) were identified above the area occupied by Janusfjellet Subgroup (11.7%), covered by 40.4% of the total ship track. Kapp Toscana Group, Sassendalen Group and Tempelfjorden Group occupy less than 5% of the fjord, and the coverage of the ship track has also been below 5% for each of these stratigraphic units. Consequently, the number of flares identified in the echograms is also meager. By doing the normalization of the number of flares with regard to the ship track, it stands out that 47.3% of the flares are located within Janusfjellet Subgroup, 22.2% are over Van Mijenfjorden Group, and 15.5% and 15.1% are over Kapp Toscana Group and Adventdalen Group, respectively. No flares were detected within the Sassendalen Group and Tempelfjorden Group (Figure 26) (Appendix 1 Table 2).

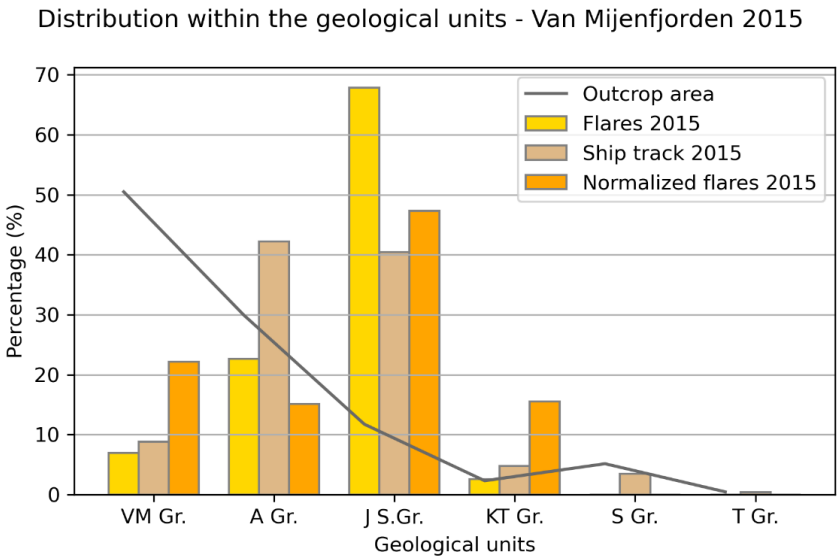

Figure 26. Bar chart of the percentage of flares, ship track and normalized flares within each stratigraphic unit (youngest to oldest from left to right) in Van Mijenfjorden for the 2015 dataset. VM Gr. stands for Van Mijenfjorden Group, A Gr. stands for Adventdalen Group, J S.Gr. stands for Janusfjellet Subgroup, Ag Fm. stands for Agardhfjellet Formation, KT Gr. stands for Kapp Toscana Group, B. Fm. stands for Botneheia Formation, S Gr. stands for Sassendalen Group, T Gr. stands for Tempelfjorden Group and G Gr. stands for Gipsdalen Group. The line shows the percentage of area that each geological unit represents in the fjord.

5.5.3. Isfjorden 2021

The absolute number of flares in the dataset from June 2021 shows a high abundance of flares near the coast, finding 97.3% of them inside the closest 4 km from the coastline. These distance bins have a higher percentage of flares than ship track coverage, accounting for 61.5% of the total. The bin 1-2 km concentrates the highest number of flares, with 40.8% of the total, and accounting for 18% of the ship track cover (Figure 27). Unlike the dataset from 2015, there are no flares located further than 5 km from the coastline (Appendix 1 Table 5).

As a result of bad data quality in the deepest areas of the fjords, the flares' normalization has been done applying different confidence ranges based on depth ranges. The normalization based on the full ship track shows a high percentage of flares close to the coastline (28.7% in 0-1 km and 34.3% in 1-2 km), and lower values in distant bins (17.5% in 2-3 km, 15.97 km in 3-4 km and 3.5% in 4-5 km). However, the normalization based on the high confidence ship track, which only covers areas shallower than 150 m, shows much more regular values for the 4 closest bins (18.8% in 0-1 km, 26.1% in 1-2 km, 21.2% in 2-3 km and 26.2% in 3-4 km). Since no flares were found further than 5 km, and consequently, the normalization values for both confidences account for zero (Figure 27).

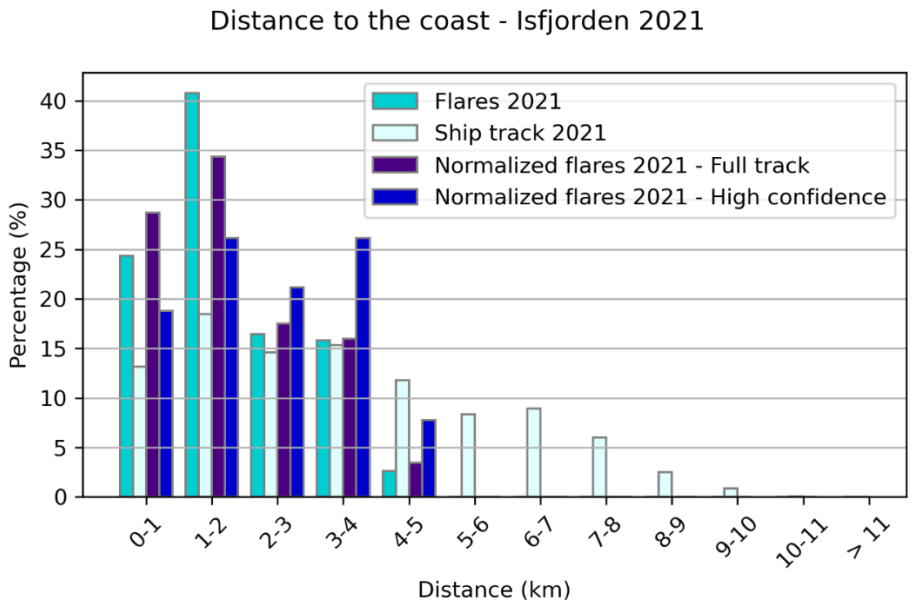

Figure 27. Bar chart of the percentage of flares, ship track and normalized flares for two confidence range. The data is divided into 1 km distance bins from the coastline in Isfjorden for the 2021 dataset.

The depth distribution of the flares from the 2021 dataset presents a Gaussian-like distribution, concentrating 94.5% of the total flares in the upper 100 m. Below that depth, there is a low number of flares. However, the total ship track covered all depth bins until 260 m (Appendix 1 Table 8).

I have used the ship track with the highest confidence (<150 m) for the data normalization (Appendix 1 Table 9). The results show that between 10 and 50 m, there are the highest flare percentages: 14.4% in 10-20 m, 11.8% in 20-30 m, 11.9% in 30-40 m and 20.3% in 40-50 m. Below 50 m, the flare concentration plummets until 140 m (Figure 28).

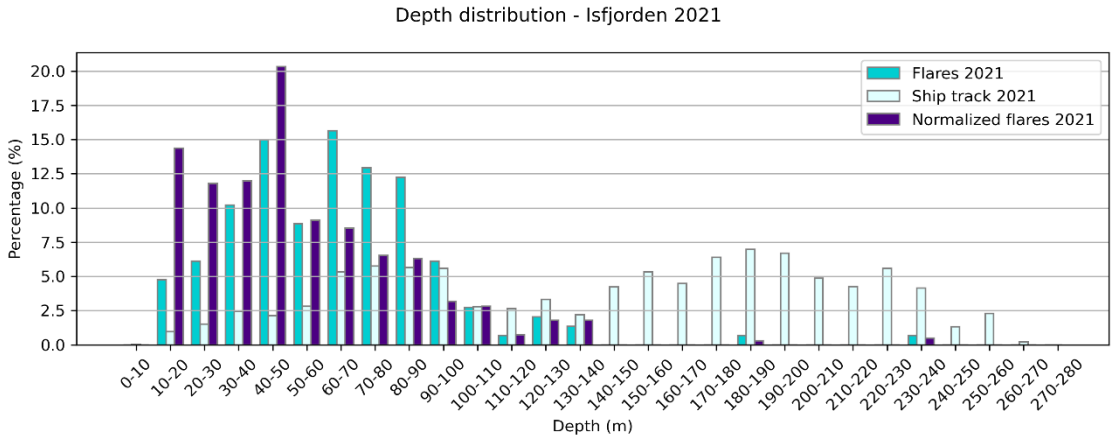

Figure 28. Bar chart of the percentage of flares, ship track and normalized flares organized by depth ranges in Isfjorden for the 2021 dataset.

In the 2021 dataset, the highest concentration of flares is over Janusfjellet Subgroup (43.4%). The percentage of flares is higher than the percentage of ship track for all its associated uncertainties covering this geological unit. Gipsdalen Group (17.8%), Tempelfjorden Group (13.1%), Kapp Toscana Group (14.5%) and Botneheia Formation (10.5%) follow being the units with the highest percentage of flares, which is lower than the percentage of ship track. One and zero flares are found over Agardhfjellet Formation and Sassendalen Group, respectively. Van Mijenfjorden Group and Adventdalen Group do not have data because they were not covered during the cruise performed in June 2021, which focused on the inner part of Isfjorden. The flare normalization with regard to the high-confidence ship track presents different results. Kapp Toscana Group is the unit with the highest flare concentration, with 23.8% of the flares. It is followed by Janusfjellet Subgroup (22.8%), Tempelfjorden Group (15.8%), Botneheia Formation (13.6%), Agardhfjellet Formation (12.8%) and Gipsdalen Group (11.1%) (Figure 29) (Appendix 1 Table 2).

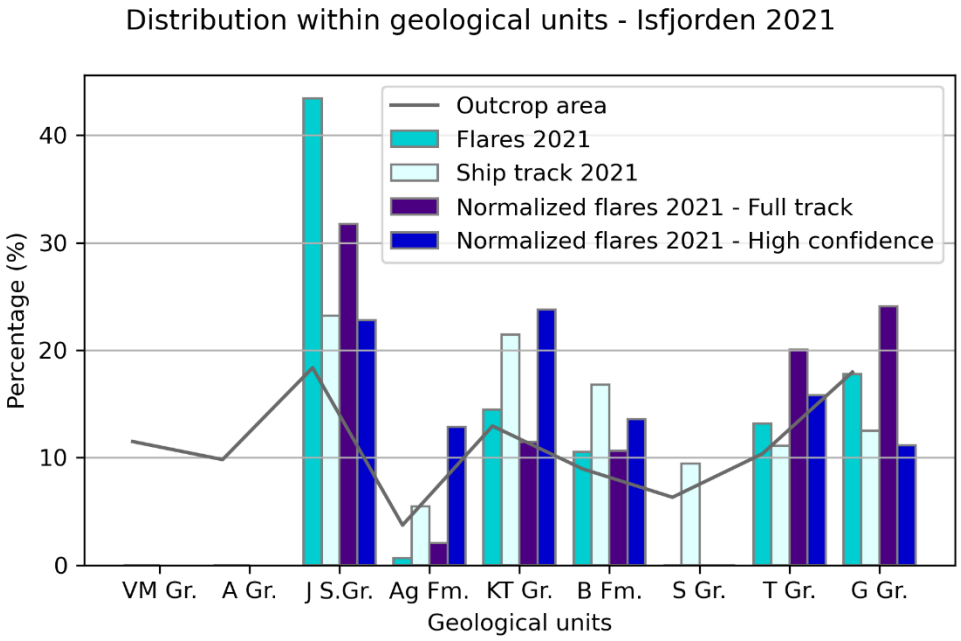

Figure 29. Bar chart of the percentage of flares, ship track and normalized flares within each stratigraphic unit (youngest to oldest from left to right) in Isfjorden for the 2021 dataset. VM Gr. stands for Van Mijenfjorden Group, A Gr. stands for Adventdalen Group, J S.Gr. stands for Janusfjellet Subgroup, Ag Fm. stands for Agardhfjellet Formation, KT Gr. stands for Kapp Toscana Group, B. Fm. stands for Botneheia Formation, S Gr. stands for Sassendalen Group, T Gr. stands for Tempelfjorden Group and G Gr. stands for Gipsdalen Group. The line shows the percentage of area that each geological unit represents in the fjord.

5.5.4. Pockmarks

The distribution of pockmarks (Roy et al., 2015) results from the interpretation of the full bathymetric coverage in Isfjorden (Figure 6). Therefore, it is not influenced by the ship tracks performed during the cruises. Unfortunately, no pockmark interpretation was performed in Van Mijenfjorden. The geostatistical analyses show a very low concentration of pockmarks in the first km closer to the coast of Isfjorden (2.8% in 0-1 km). The highest concentration of pockmarks is compressed between 1-3 km from the coastline, representing 16,9% for the 1-2 km bin and 20,3% for the 2-3 km bin. After that, there is a decreasing concentration trend towards the center of the fjord. In the range 3-8 km, there is an average pockmark concentration of 11% per bin, and further into the fjord (>10 km), the concentration drops to less than 1% (Appendix 1 Table 5).

Looking at the pockmark distribution within the geological units outcropping in the fjord, we see that the Van Mijenfjorden Group presents a low concentration of pockmarks (1.4%), representing 11.5% of the area in Isfjorden. Individually the western part of the Adventdalen Group, Janusfjellet Subgroup (3.9%) and Agardhfjellet Formation also present a low number of pockmarks. However, they are part of Adventdalen Group, the most extensive geological unit outcropping in the fjord, occupying 31.9% of the total area, and when summing the pockmarks, they represent 13.2% of the total. Kapp Toscana Group accumulates 21.8% of the pockmarks over 12.9% of the area of Isfjorden. Botneheia Formation alone groups 12.1% of the pockmarks over 8.9% of the area. However, combining it with the rest of Sassendalen Group sums 26.1% of the pockmarks over 15.3% of the area. Finally, Tempelfjorden Group has 12.2% of the pockmarks in 10.4% of the area, and Gipsdalen Group is the geological unit with the highest number of pockmarks (25.2%) over 17.9% of the area in the fjord (Figure 30) (Appendix 1 Table 4).

To make a quantitative comparison of the pockmark distribution, I normalized the point density based on the area of each geological unit in the fjord (Appendix 1 Table 4). And in this case, the distribution presents a clear trend. The geological units located in the inner part of Isfjorden concentrate a high number of pockmarks per outcropping area: Kapp Toscana Group (18.4%), Botneheia Formation (14.8%), Sassendalen Group (24.2%), Tempelfjorden Group (12.9%) and Gipsdalen Group (15.3%). The units located towards the mouth of Isfjorden present a low ratio of pockmarks per area, being Agardhfjellet Formation (2.8%) and Van Mijenfjorden Group (1.4%) the ones with the lowest values (Figure 30) (Appendix 1 Table 4).

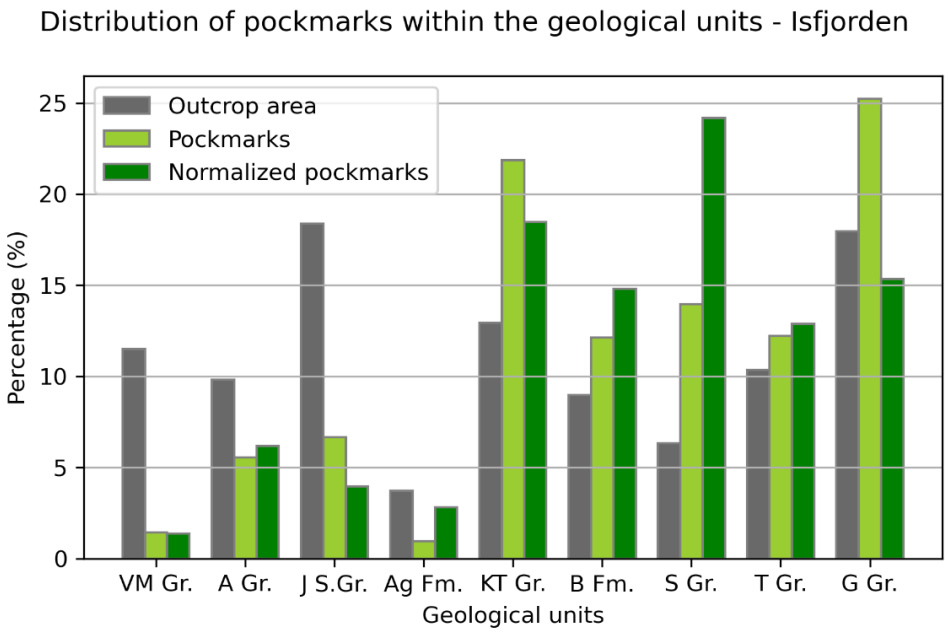

Figure 30. The bar chart shows the percentage of area each geological unit represents in the fjord, pockmarks and normalized pockmarks within each stratigraphic unit (youngest to oldest from left to right) in Isfjorden. VM Gr. stands for Van Mijenfjorden Group, A Gr. stands for Adventdalen Group, J S.Gr. stands for Janusfjellet Subgroup, Ag Fm. stands for Agardhfjellet Formation, KT Gr. stands for Kapp Toscana Group, B. Fm. stands for Botneheia Formation, S Gr. stands for Sassendalen Group, T Gr. stands for Tempelfjorden Group and G Gr. stands for Gipsdalen Group.

6. DISCUSSION

6.1. Flare analysis and interpretation

6.1.1. Flare characteristics

Inferring the flare characteristics from the 2015 dataset, we see that the flare intensity distribution between Isfjorden and Van Mijenfjorden does not reflect a clear pattern. In Isfjorden, high-intensity flares seem to be related to the base of steep slope areas in the fjord's inner part (Figure 31). Proportionally, Van Mijenfjorden has 5.8% of more intense flares than Isfjorden. Nonetheless, in Van Mijenfjorden, there is no correlation between the flare intensity and the bathymetry since high-intensity flares are concentrated both in the shallowest and deepest part of the fjord.

The flare's geometry and structure from the 2015 dataset shows that the flares from Isfjorden are much higher than the ones in Van Mijenfjorden. The average flare height in Isfjorden is 42.7 m, and the maximum value, 192.2 m. In Van Mijenfjorden, the average flare height is 21.4 m, and the maximum height is 69.7 m. The flare's characteristics from the 2021 dataset in Isfjorden show that the average height is 16.1 m, and the maximum value is 44.9 m, much smaller than the flares detected in 2015 (Figure 31). I suggest that these height differences result from larger bubbles size due to greater accumulations of subsurface shallow gas seeping from the seafloor in the deeper parts of Isfjorden.

Methane fluxes into the atmosphere rise with increasing flare height and decreasing water depth (Greinert et al., 2010). Shallow sites (depths <100 m) may represent a significant source of methane to the surface water and direct local emissions into the atmosphere (Schmale et al., 2005). The flares detected in the deep parts of Isfjorden do not reach the water surface but contribute to keeping the fjord waters supersaturated with methane (Damm et al., 2021). Methane is mixed within the water column, transported along vertical isopycnals until it reaches the water-atmosphere interface (Damm et al., 2021). Nevertheless, I believe the shallow sites with large flares clusters contribute direct methane efflux (gas input into the atmosphere).

Neither of the datasets contains double flare countings, even though flares were detected in ship track crossings (Figure 13). This suggests that the flares were not always present, and even

detecting a large proportion of continuous flares in the hydroacoustic profiles, the gas flux is spatially and temporally variable.

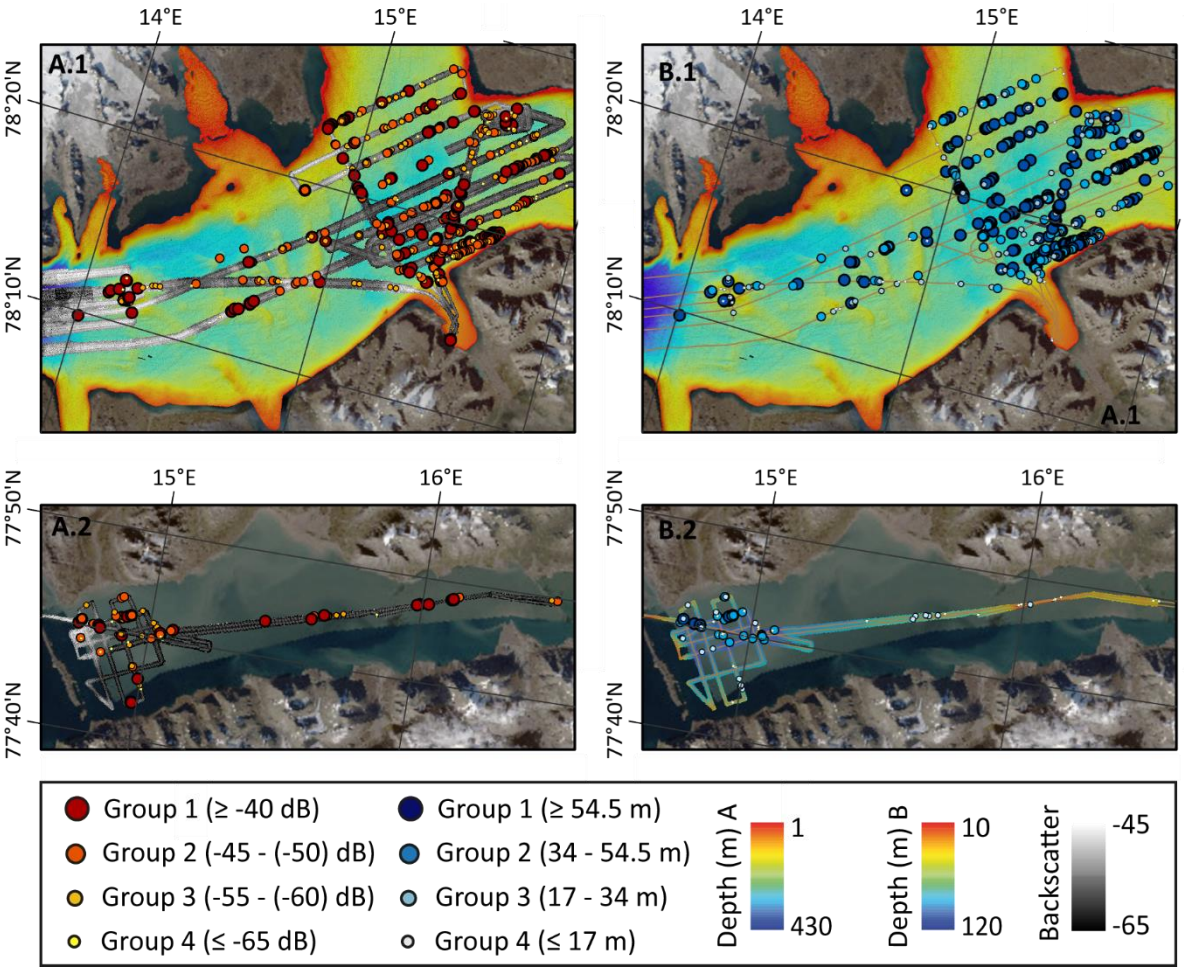

Figure 31. A.1: Map of Isfjorden with the flares characterized by intensity groups. A.2: Map of Van Mijenfjorden with the flares characterized by intensity groups. B.1: Map of Isfjorden with the flares characterized by height groups. B.: Map of Van Mijenfjorden with the flares characterized by height groups.

6.1.2. Flare distribution

The area covered is the result of the ship track and the fjord's bathymetric profile. The shallower the bathymetric relief, the narrower is the multibeam swath, reducing the probability of observing flares in the echograms (Figures 18, 19). Therefore, it can be assumed that there is a bias in which the area covered by the ship track influences the flare distribution. Consequently, it is essential to normalize the depth values of the flares with the percentage of depth covered by the ship track (Figure 32). Moreover, the 2021 results could also be biased by the bad acquisition quality in the deeper parts of the fjord (i.e., >150 m depth). This also influenced the ship track, which had to be adjusted according to the multibeam depth range limitations, mainly

covering the shallow waters of Isfjorden and the tributary fjords. The quality of the echograms is depth-dependent. Consequently, the ship track data has been divided into different depth groups and their uncertainty to reduce possible bias.

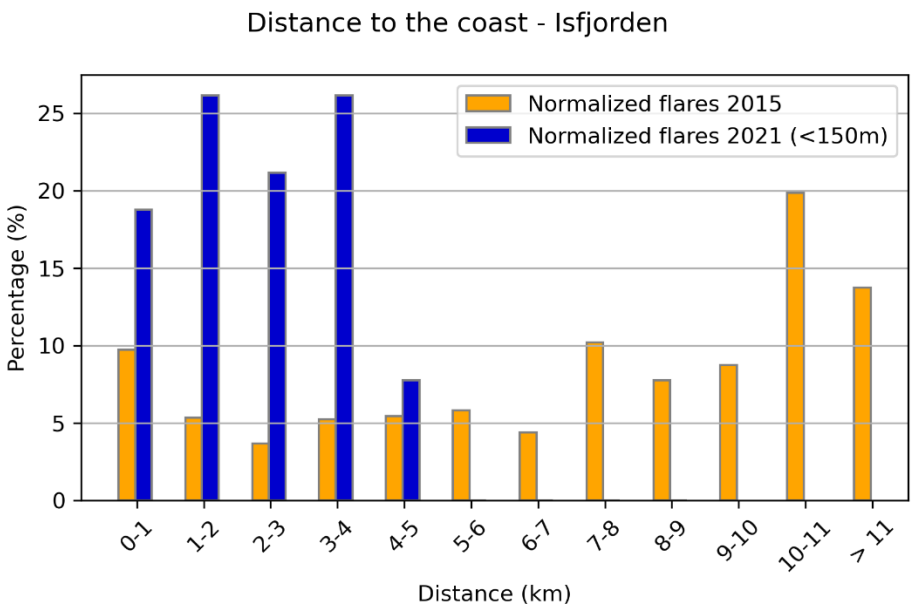

Figure 32. Bar chart comparing the percentage of normalized flares, organized in 1 km distance bins from the coastline in Isfjorden, for the 2015 and 2021 datasets.

6.1.3. Correlation with stratigraphic units

The results of the distribution of flares in 2015 compared to the geological units outcropping in the fjord revealed that gas emissions were concentrated above Agardhfjellet Formation, Kapp Toscana Group and Botneheia Formation. Agardhfjellet Formation and Botneheia Formation are the rich-organic formations of Svalbard, rock formations with oil and gas potential. Moreover, the Kapp Toscana Group presents a large concentration of faults with respect to its area (12,9%), concentrating the 21% of the overall faults outcropping in the fjord (Blinova et al., 2012; Roy et al., 2015) (Appendix 1 Table 4). These faults could act as migration pathways for the gas generated in the underlying Botneheia Formation, reaching the seafloor and seeping into the water column. Moreover, there is a high percentage of pockmarks (21.8%) within the area covered by the Kapp Toscana Group, indicating an active fluid flow system.

The comparison of the normalized flare and ship track datasets from 2015 and 2021 with the geological units illustrates some differences: a) In the 2015 dataset, only 3.5% of the normalized flares were found within the Janusfjellet Subgroup. However, in 2021, 22.8% of the normalized flares are over this unit. This is because the highest concentration of flares found in 2021 is

located inside the shallow waters of Adventfjorden, where the Janusfjellet Subgroup outcrop dominates. b) The distribution of flares inside the Agardhfjellet Formation also differs between the two years. In 2015 the flares found within this formation represented 19.3%, while in 2021, they only account for 0.6%. c) Another difference relates to the Kapp Toscana Group, where 45.9% of the flares detected in 2015 were within outcrops of the predominant geology grouping, but this value decreased to 14.5% in 2021. d) Finally, Tempelfjorden Group and Gipsdalen Group, over which no flares were described in 2015, account for 13.1% and 17.8% of the flares in 2021, respectively. In contrast, Botneheia Formation and Sassendalen Group present similar flare values between the two datasets (Figure 33).

Due to the lack of information in the 2021 dataset, no comparison has been made over Van Mijenfjorden Group and Adventdalen Group.

The ship tracks differences between 2015 and 2021 could be a source of error in our results. However, the proportion of coverage of the geological units is similar in both datasets. Therefore, this bias can be neglected in this discussion.

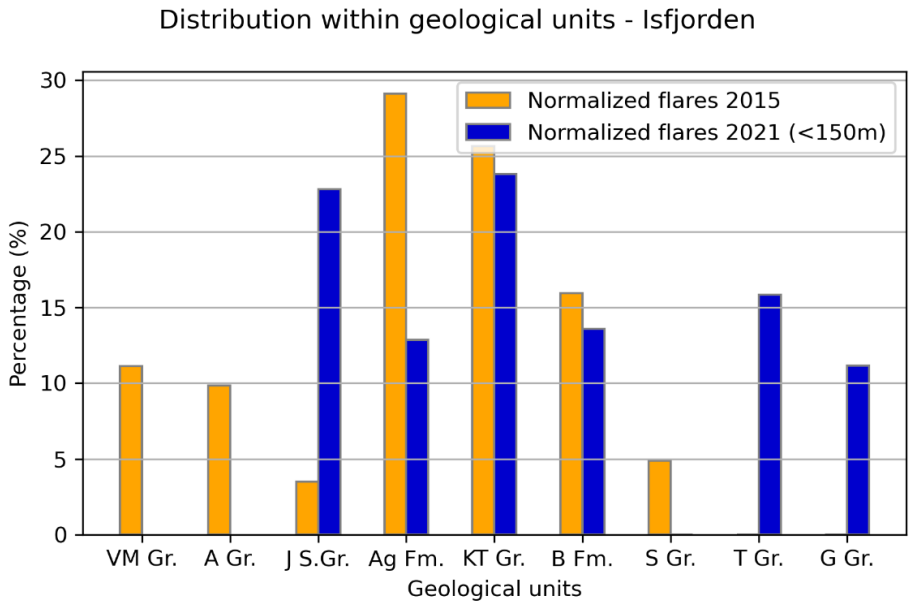

Figure 33. The bar chart compares the normalized flares' percentage within each geological unit (youngest to oldest from left to right) outcropping in Isfjorden for the 2015 and 2021 datasets. VM Gr. stands for Van Mijenfjorden Group, A Gr. stands for Adventdalen Group, J S.Gr. stands for Janusfjellet Subgroup, Ag Fm. stands for Agardhfjellet Formation, KT Gr. stands for Kapp Toscana Group, B. Fm. stands for Botneheia Formation, S Gr. stands for Sassendalen Group, T Gr. stands for Tempelfjorden Group and G Gr. stands for Gipsdalen Group.

In the seismic profiles from Van Mijenfjorden, I could not differentiate Agardhfjellet and Botneheia Formations from their respective stratigraphical groups and subgroups (Figure 34).

Agardhfjellet Formation is a rich-organic unit part of the Janusfjellet Subgroup, with related hydrocarbon potential. I speculate that the observations of a high flare concentration above the Janusfjellet Subgroup might be related to light hydrocarbons produced within the Agardhfjellet Formation.

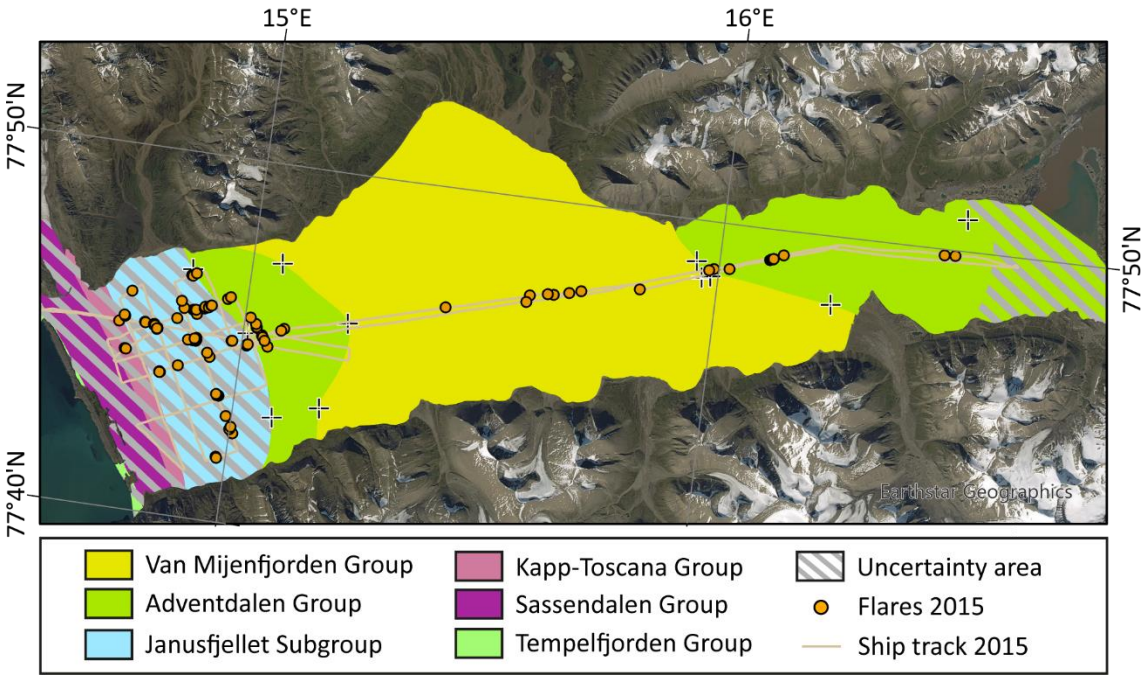

Figure 34. Flare distribution in Van Mijenfjorden within the different stratigraphic units outcropping in the fjord. EPSG:32633 projection and base map is courtesy of Earthstar Geographics.

6.2.4. Correlation with pockmarks

There is no clear correlation between the areas densely populated with pockmarks and the flare distribution. Pockmarks are displayed as single bathymetric features or in clusters. Generally, in both cases, flares are absent in areas with high pockmark concentrations (Figure 35). On the one hand, the reason why pockmarks have not developed in the areas where gas flares have been detected can be a consequence of a coarser nature of the seafloor sediments (Forwick et al., 2009). On the other hand, this can be due to the current inactivity of the pockmark locations or because the pockmarks are not releasing enough methane to appear as a gaseous phase and to be detected as an acoustic flare in the water column (Roy et al., 2015).

In Isfjorden, the pockmarks are concentrated in the inner part of the fjord, the region where the oldest stratigraphical units outcrop. Moreover, there is no clear relationship between the pockmark distribution and the flares detected in the 2015 and 2021 datasets (Figure 35). Therefore, I speculate that the pockmarks described by Roy et al., 2015 in Isfjorden are not

caused by the current seepage but might be paleopockmarks caused by a former fluid system that migrated along fault zones, doleritic intrusions and geological unconformities towards the surface. Meanwhile, the seepage detected in the flare datasets found its way to the water column via other channels. Pockmarks located far from the tectonic lineaments could be formed by diffuse fluid flow through the marine sediments or seepage of microbial gas formed in the shallow sediments. The pockmarks in Isfjorden could partly also result from the dissociation of gas hydrates since more than 600 pockmarks are located within the potential GHSZ (Betlem et al., 2021) (Figure 6). Thawing near-shore subsea permafrost and gas hydrate dissociation are possible mechanisms for pockmark formation (Roy et al., 2015).

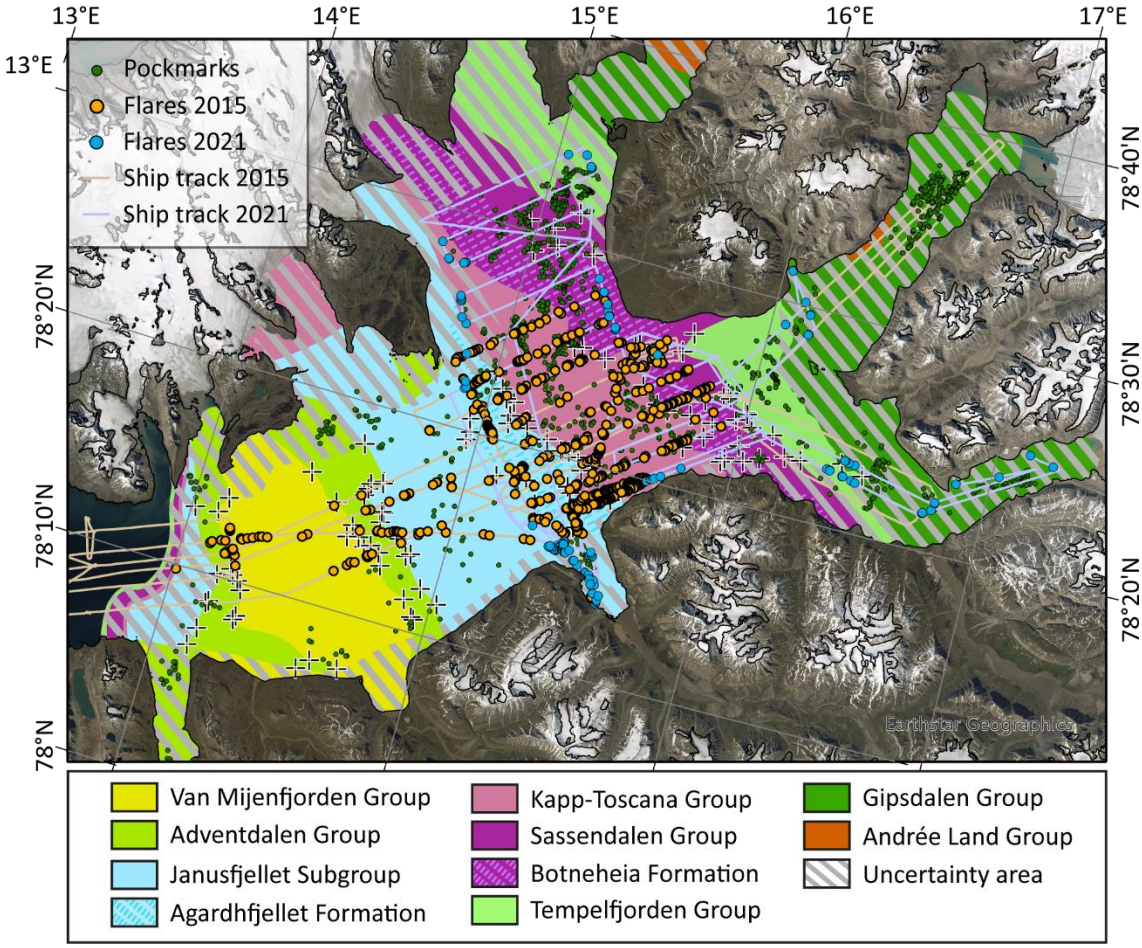

Figure 35. Stratigraphic units outcropping in Isfjorden and tributary fjords. In yellow are the flares interpretations along the transect lines of the 2015 dataset. In blue are the flares interpretations and the ship track from the 2021 dataset. In green is the pockmark distribution described by Roy et al., 2015. EPSG:32633 projection and base map is courtesy of Earthstar Geographics.

6.2. Spatio-temporal variability of the gas seepage

Based on the observations and analyses of the results, I argue for five different hypotheses regarding the spatio-temporal variability of the gas seepage:

6.2.1. Hypothesis 1: Thermogenic origin from source rocks

The first hypothesis that I raise is that the gas flares detected in the echograms rising through the water column have a thermogenic origin coming from deep sources and that the stratigraphy and lithology control the fluid flow.

The results from the geostatistical analysis show that in Isfjorden, the highest flare concentration in 2015 was concentrated over Agardhfjellet Formation, Kapp Toscana Group and Botneheia Formation. In June 2021, the highest flare concentrations were over Janusfjellet Subgroup (mainly located in Adventfjorden) and Kapp Toscana Group. In the latest dataset, barely any flares were found over Agardhfjellet Formation (Figure 36).

In Van Mijenfjorden, the largest number of flares is within Janusfjellet Subgroup. This includes the Agardhfjellet Formation, which I could not differentiate in the seismic profiles.

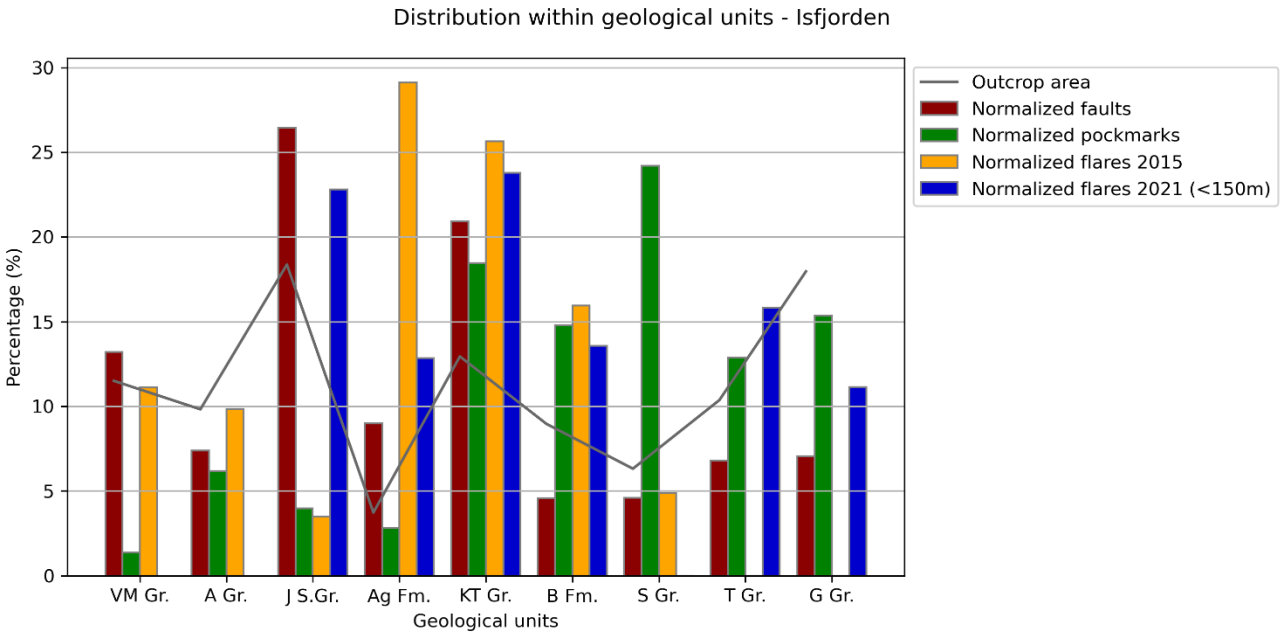

Figure 36. The bar chart compares the normalized flares' percentage within each geological unit (youngest to oldest from left to right) outcropping in Isfjorden for the 2015 and 2021 datasets. Also, the percentage of normalized flares and pockmarks in the geological units. VM Gr. stands for Van Mijenfjorden Group, A Gr. stands for Adventdalen Group, J S.Gr. stands for Janusfjellet Subgroup, Ag Fm. stands for Agardhfjellet Formation, KT Gr. stands for Kapp Toscana Group, B. Fm. stands for Botneheia Formation, S Gr. stands for Sassendalen Group, T Gr. stands for Tempelfjorden Group and G Gr. stands for Gipsdalen Group.

As introduced in section 2.3.2., the Agardhfjellet and Botneheia Formations have hydrocarbon potential and are a direct gas source. Roy et al., 2014, suggests that the gas migrates from the bedrock sources through fluid-flow systems up to the seafloor. Moreover, Knies et al., 2004 found high concentrations of adsorbed methane and ethane in the southern part of Nordfjorden, implying a thermogenic gas origin that could have experienced a short-range migration from the organic-rich formations.

Structural fracture zones are areas where methane migrates upwards from deep bedrocks, and shallow gas occurrence eventually favors gas seeping into the marine environment (Judd and Hovland 2007; Forwick et al., 2009; Roy et al., 2015; Mau et al., 2017). The Kapp Toscana Group is the most porous and permeable unit in the area and presents a high concentration of faults (Figure 36) (Appendix 1 Table 4), which could act as fluid conduits for large quantities of gas coming from the underlying Botneheia Formation. Janusfjellet Subgroup consists of strongly crushed and altered shale and is highly fractured (Roy et al., 2014). Structural characterization of core samples documents a high fracture frequency up to 50 f m^{-1} (Braathen et al., 2012). Moreover, it contains more than 25% of the total faults interpreted in Isfjorden, which could serve as migration pathways for the gas from the underlying Agardhfjellet Formation.

Pockmarks are found over all the units outcropping in the fjord, but with higher concentrations over Kapp Toscana Group, Botneheia Formation, Sassendalen Group, Tempelfjorden Group and Gipsdalen Group (Figure 36). Their numerous occurrence aligned with fractures and steep faults suggests that these could provide direct routes for the methane-rich fluids, which would then seep through the seafloor forming pockmarks (Roy et al., 2014) (Figure 38). There is also a high concentration of pockmarks along the outcropping edge of doleritic intrusions from the Early Cretaceous, which could also be crucial in channeling the buoyant fluid flow towards the surface (Roy et al., 2014).

The spatial distribution of flares detected in the fjords does not correlate with the pockmark distribution. This could be because the flare distribution is altered by differences in sediment accumulation, subsurface bedding geometry, migration paths (fractures, faults and intrusions), differences in expulsion rates, and action of bottom currents. The non-flare-pockmark correlation also suggests that the pockmarks described by Roy et al., 2015 are paleopockmarks formed by a former fluid system that migrated along faults towards the surface. This is clear over the Kapp Toscana Group, a unit that does not have high hydrocarbon potential but is highly fractured, transporting the gases from deep sources. The spatial pockmark distribution in the

seafloor over this unit is closely correlated with the faults interpreted by Blinova et al., 2012 outcropping in the fjord (Figure 37).

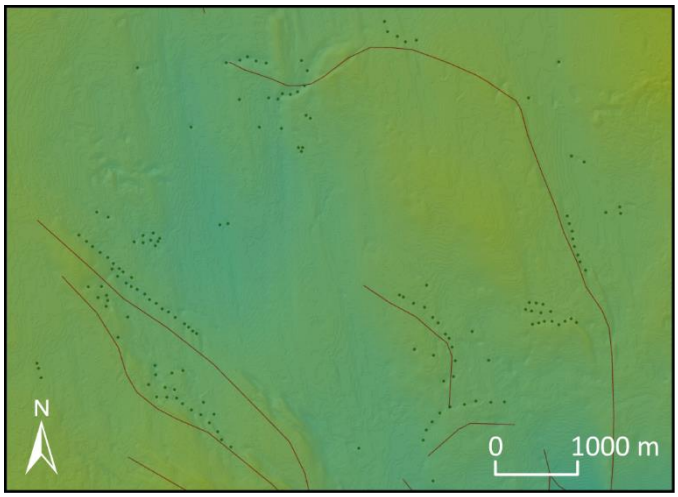

Figure 37. Detail of the outcropping faults in red (Blionva et al., 2012) and the pockmark distribution in green (Roy et al., 2015) over Isfjorden's seafloor. The figure is spatially referenced in Figure 6.

In Van Mijenfjorden, the highest number of normalized flares is at 30-40 m water depth, in the sill located 33 km from the fjord's mouth. This matches with the outcropping stratigraphical boundaries between Van Mijenfjorden Group and Adventdalen Group (Figure 34), which could indicate fluid migration in the boundary between stratigraphic units.

Another fact supporting this hypothesis are the flares detected in the 2021 dataset over the Billefjorden fault zone (Figures 6, 19). These flares are over the Tempelfjorden and Gipsdalen Groups, which do not have hydrocarbon potential. However, the Billefjorden fault system could act as a migration pathway from deep thermogenic sources towards the seafloor.

This hypothesis does not explain the flares detected in Tempelfjorden, where there is a large cluster of pockmarks but no faults outcropping in the fjord (Figure 6). Therefore, it is unlikely that the gas detected in that area has a thermogenic origin.

In any case, the only way to prove that the gas comes from a thermogenic source is to take in-situ samples and analyze the hydrocarbon concentrations revealing the C_1:C_{2+} ratio and the carbon and hydrogen isotopic composition.

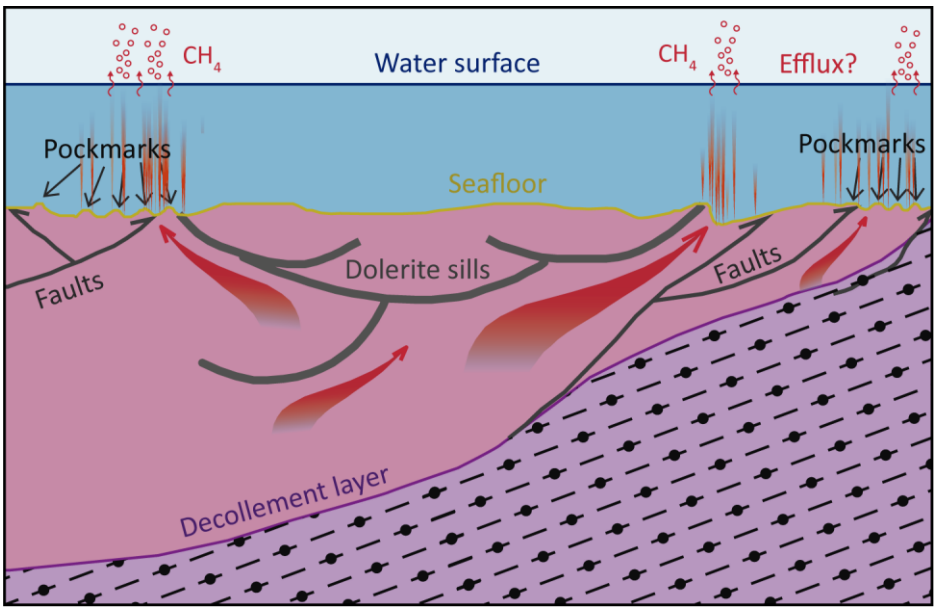

Figure 38. Conceptual model adapted from Roy et al., 2014. It shows the decollement layer between two stratigraphic units (the underlying unit represents rich-organic content). The igneous intrusions and the faults act as migration pathways for the gas that seeps through the seafloor in the form of gas flares and creating pockmarks.

6.2.2. Hypothesis 2: In-situ gas production from Holocene sediments

The second hypothesis that I pose based on the observations is that the gas detected in the hydrographic profiles results from the in-situ production in the Holocene sediments of the fjords. In both the 2015 and 2021 hydrographic datasets, many flares are distant from fluid migration systems such as faults and the boundaries of the geological units (Figure 35). Consequently, I suggest that the gas detected in these areas is attributed to the seepage of microbial gas formed in the shallow sediments.

The gas flares characterization shows that 33% of the flares detected in 2015 in Isfjorden and 42% of the flares detected in 2021 have a pulsing nature, and in Van Mijenfjorden, the pulsing flares account for 29% of the total. I suggest that this could be an indicator of biogenic gas accumulation as a consequence of microbial activity producing methane and forming bubbles when methane concentrations in the sediment are high enough (similar to the biogenic gas formation mechanism described in lake systems).

Fjords present some of Earth's most rapid sedimentation rates and organic carbon burial (Włodarska-Kowalczuk et al., 2019). If muddy sediments contain enough organic matter to support microbial communities, these can produce microbial gas (Audsley et al., 2021). In the

Svalbard archipelago, high organic matter deposition rates of 5 to 17 g m^{-2} yr^{-1} were reported in the fjords (Winkelmann and Knies, 2005), favoring the methane produced by the degradation of organic matter in near-surface sediments (Damm et al., 2021).

The microbial methanogenesis would support the spatio-temporal variability of the gas flares detected in the 2015 and 2021 datasets in Isfjorden (Figure 39). A temperature-dependent mechanism could boost the microbial activity in the superficial sediments of the fjord in summer due to the temperature increase of the water column. This would explain why in the dataset from June 2021, when the deep parts of the water column are still cold but the upper part is getting warmer, there is a high concentration of flares in the upper 100 m. Contrarily, in the dataset from late August 2015, when higher temperatures reached the deeper parts of the water column, flares are found below 100 m, but rarely above this depth.

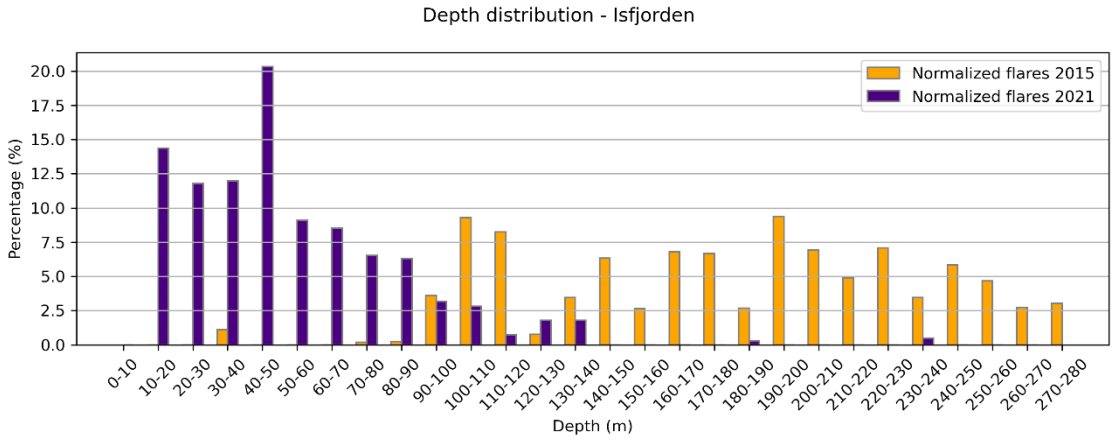

Figure 39. The bar chart compares the percentage of normalized flares from 2015 and 2021 in Isfjorden organized by depth ranges.

This hypothesis suggests that during the early spring-summer, the upper parts of the water column get warmer and stratified, causing an increase of the microbial activity in the shallow sediments, which would decompose the organic matter accumulated over the winter. In late summer or early autumn, with the water column mixing, there would be a temperature rise on the deeper parts of the fjords, resulting in a microbial activity increase that would start decomposing the organic matter in deeper sediments. However, the organic matter located in the shallow parts of the fjords would have already been decomposed by then, not manifesting any more flares.

This hypothesis for the microbial gas formation would explain why in June 2021, so many flares were detected in the shallow waters of Adventfjorden or Tempelfjorden, far away from any tectonic lineaments and unrelated to rich-organic source rocks. However, it does not explain

why there is such a difference in the number of gas flares within different geological units since its distribution should only depend on the input of organic matter in the fjord and the water temperature.

Similarly to hypothesis 1, it is necessary to take in-situ gas samples and analyze the carbon isotopic composition of methane (δ13C) to determine the gas genesis.

6.2.3. Hypothesis 3: Sub-sea permafrost

The third hypothesis that I suggest is sub-sea permafrost as a controlling factor of the gas detected in some parts of the fjords. In August 2015, a large number of flares were detected in a steep slope close to the southern coast of Isfjorden, in a depth range between 94 and 250 m. However, just a few flares were discovered there in June 2021, and all above 100 m depth (Figure 19). As argued in hypothesis 2, there is a significant seasonality in the fjords resulting from temperature changes in the water column (Skogseth et al., 2020). Therefore, I hypothesize that the temperature change could contribute to seasonal sub-sea permafrost degradation leading to captured or trapped gas release.

The drilling results from the borehole DH6 in Adventdalen indicate an increase in gas concentration directly beneath the permafrost, placed at approximately 120 m depth (Senger et al., 2017). As Roy et al., 2014 discussed, the gas detected in the water column could result from the gradual thinning and degradation of the near-shore permafrost layer. The fluids would migrate along the onshore impermeable permafrost and seep through to the seabed where the permafrost is absent.

One example supporting this hypothesis is the flare observation within Billefjorden, which is crossed by the Billefjorden fault zone and where there is a large pockmark cluster (Roy et al., 2015) (Figure 6). However, no gas flares were detected in the over 100 km of hydrographic profiles acquired during the cruise performed in August 2015 (Figure 19). The explanation I propose is that the deeper parts of the water column in the fjord are at sub-freeze temperatures all year round (Figure 40). This is a consequence of the restricted water inflow from the main trunk of Isfjorden, limited by the shallow sill in the mouth of the fjord. The low temperatures could cause a stable impermeable sub-sea permafrost layer that acts as a trap preventing the gas from escaping towards the surface (Figure 41). Roy et al., 2012 suggested a pockmark

formation mechanism associated with the permafrost thawing in the coastal areas, releasing large amounts of methane into the water column and the atmosphere. The cluster of pockmarks in Billefjorden could be the consequence of a massive overflow event of warm waters behind the sill, which increased the temperature of the inner part of the fjord destabilizing the permafrost layer and releasing the gas accumulated underneath.

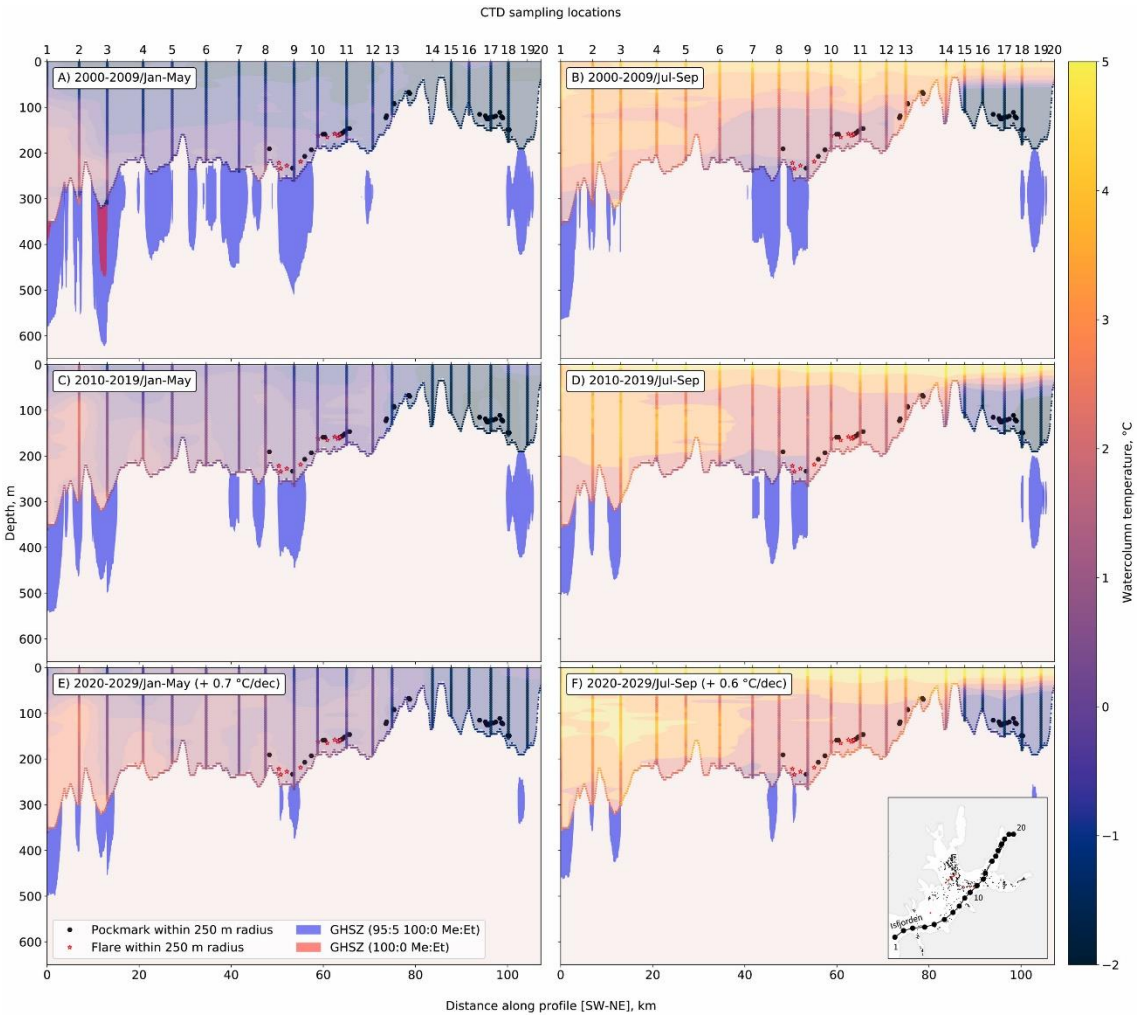

Figure 40. The figure shows the temporal GHSZ cross-sections along 20 CTD sited in Isfjorden. The water column temperature in Billefjorden is in permanently sub-freeze conditions. Figure published by Betlem et al., 2021.

An increased inflow of Atlantic Water results in a temperature rise in the water column from Isfjorden (Skogseth et al., 2020). This increment in temperature will negatively impact the permafrost extent, potentially releasing the gas trapped underneath. Methane release from beneath permafrost represents a significant uncertainty in the Arctic greenhouse gas budget (Hodson et al., 2020).

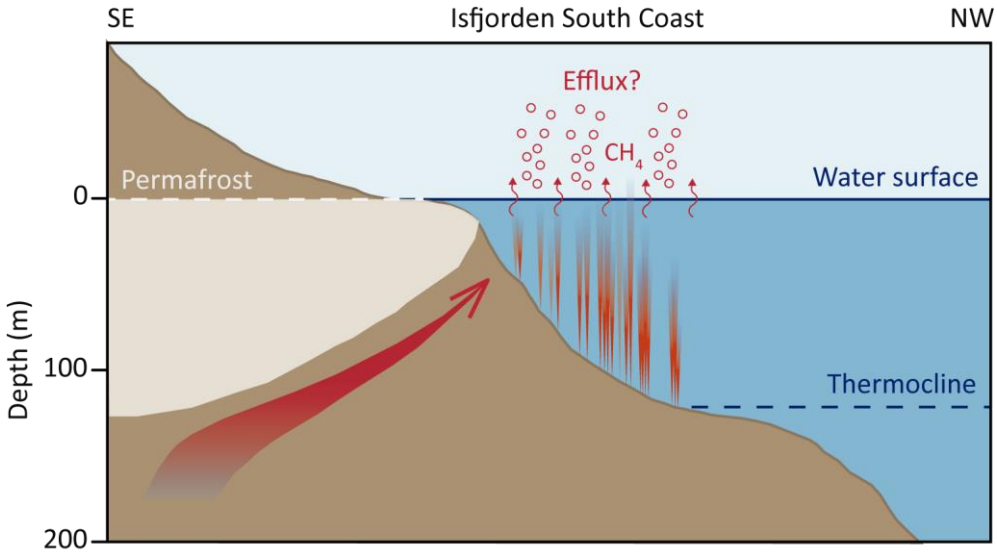

Figure 41. Conceptual model adapted from Roy et al., 2014. It represents a transect from the south coast of Isfjorden in which the gas flows below the impermeable permafrost layer until seeping into the water column as gas flares.

6.2.4. Hypothesis 4: Natural gas hydrates (NGH)

Another hypothesis that I suggest based on the observations of this work is that the gas detected in Isfjorden comes from NGH dissociation. The deepest parts of the fjords of Spitsbergen present favorable thermobaric conditions, which, together with a proven petroleum system, make it suitable conditions for the presence of NGH (Senger et al., 2017; Betlem et al., 2021). Betlem et al., 2021 modeled the GHSZ in Isfjorden, considering different parameters of gas composition. The results suggest that the GHSZ distribution is highly variable depending on different gas compositions. In the case of microbial gas, the area of occurrence for a GHSZ is minimal. However, the modeled distribution change for thermogenic gas (95:5 methane:ethane mixture) covering large areas in the main trunk of Isfjorden and the southern part of Nordfjorden. The modeled GHSZ for thermogenic gas covers multiple outcropping strata ranging in age from the Paleogene to Carboniferous, including the organic-rich sequences Agardhfjellet Formation and Botneheia Formation, increasing the likelihood of thermogenic NGH occurrence (Betlem et al., 2021) (Figure 42).

Most of the flares detected during the cruise in August 2015 are within the predicted GHSZ for thermogenic gas conditions (Figure 42). Moreover, there are high flares concentrations in the fjord's southern coast, close to the boundaries of the modeled GHSZ. Still, the 2021 dataset presents an opposite scenario with all flares, except for one found outside the potential GHSZ.

Nonetheless, it is necessary to remark that the ship track from the cruise in 2021 barely covered the GHSZ, as it was too deep for the multibeam, and consequently, it is not possible to discuss the flare relation with the GHSZ for this dataset.

In case that the seepage's temporal variability detected in the hydrographic datasets would be related to the presence of NGH, I hypothesize that it would result from temperature changes in the fjord. In early June, when the water is still cold in the deepest parts of the fjord, the NGHs are stable, not releasing any gas into the water column. However, a temperature increase in the deepwater layers by the end of the summer would influence the hydrate stability curve, causing NGH dissociation reflected as gas flares in the water column. Moreover, this phenomenon would be increased close to the GHSZ boundaries where the hydrates are more unstable, as is observed in the southern coast of Isfjorden.

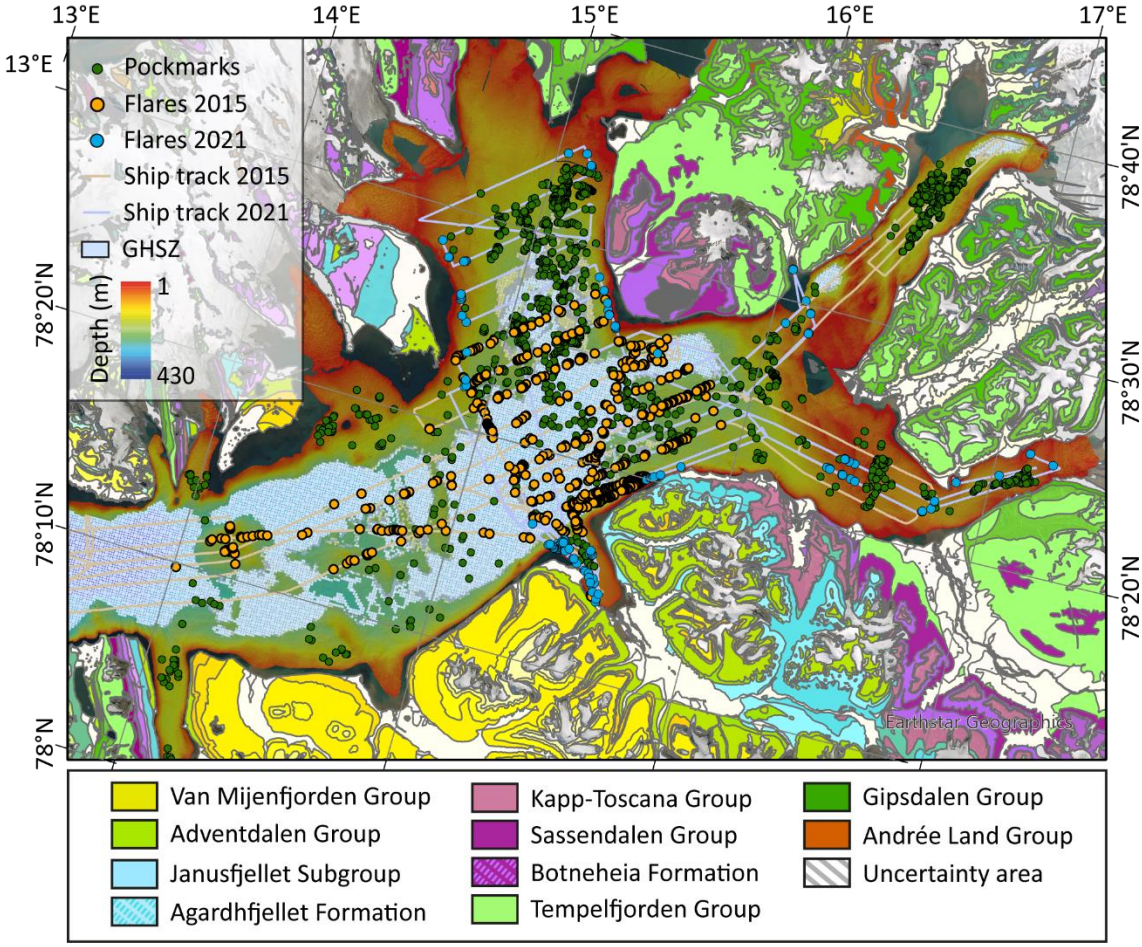

Figure 42. Bathymetric map of Isfjorden and the tributary fjords. In yellow are the flares interpretations along the transect lines of the 2015 dataset. In blue are the flares interpretation and the ship track from the 2021 dataset. In green is the pockmark distribution described by Roy et al., 2015. It is also presented the modeled GHSZ for thermogenic gas (Betlem et al., 2021). Onshore there are the geological formations outcropping (NPI). EPSG:32633 projection.

Faults could be key stratigraphic elements, providing near-vertical leakage pathways that allow gases to migrate to shallower depths where they could convert into hydrates (Figure 43). Furthermore, the dissociation of NGHs could result in fluid migration pathways opening up (Betlem et al., 2021). The pockmark distribution in Isfjorden can be linked with the presence of NGH since more than 600 pockmarks are located within the potential GHSZ (Figure 42), suggesting NGH dissociation as a potential mechanism for pockmark formation (Paull et al., 1999; Roy et al., 2015).

Due to its shallow physiographic conditions, the models do not predict any GHSZ in Van Mijenfjorden. Therefore, the gas seepage detected in that fjord has to be related to other processes.

Finding a BSR in the sediments would prove that NGHs are present in the fjords. According to the GHSZ modeled by Betlem et al., 2021, and assuming thermogenic gas composition, a BSR could have evolved in the deepest parts of Isfjorden. However, no BSR was found in the seismic profiles interpreted. An explanation for not detecting it could be related to the quality of the available seismic profiles interpreted. Notwithstanding, the presence of a BSR would require a long-term and stable NGH layer with free gas underneath. I hypothesize that if NGHs are present, they might exist in a disseminated form in the sediment as they are close to the boundary of the GHSZ, lacking a trapping effect to accumulate free gas below, and therefore, not showing a BSR.

I believe that the hypothesis of NGH controlling the gas seepage is unlikely to happen since temperature changes in the sediment are slower than in the water column, making it improbable to have such pronounced seasonal variability. Nevertheless, I suggest direct sampling as the best way to determine the NGH presence in the shallow waters of Spitsbergen.

Regardless of the gas source and composition, the widespread GHSZ provides a transient reservoir for both microbial and thermogenic methane (Betlem et al., 2021). The atmospheric and oceanic temperature increase could likely trigger the destabilization of potential gas hydrates and liberate vast quantities of methane to the atmospheric carbon pool, contributing as positive feedback to the Arctic amplification and global warming (Westbrook et al., 2009) (Figure 43). Therefore, it is necessary to gather more knowledge on their potential distribution and stability to assess the potential impact of large NGH destabilizations in the fjords.

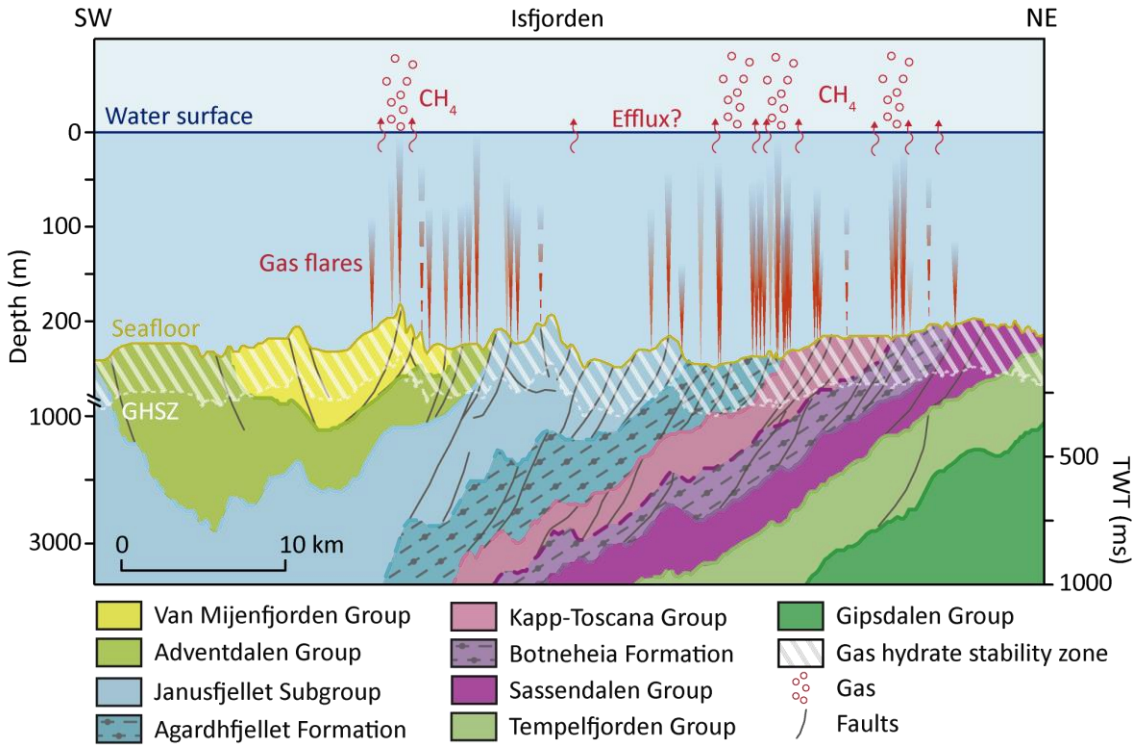

Figure 43. Conceptual model of the gas system across Isfjorden (Figure 16 for georeference). It presents the main stratigraphic groups outcropping in the fjord. The rich-organic units are the source of the thermogenic gas that migrates through the fault system (Roy et al., 2014, 2015) to the surface. There is also represented the modeled GHSZ (Betlem et al., 2021) and the gas flares interpreted in the dataset from 2015. The nature of the gas flares is pictured as continuous and pulsing. The potential efflux remains uncertain.

6.2.5. Hypothesis 5: Combination from different gas sources

Finally, based on our observations, I argue that the gas seepage in the fjords is a combination of different processes and sources. According to the results of the geostatistical analyses, gas flares, pockmarks and other fluid seepage features in Isfjorden are found within or close to organic-rich stratigraphic sequences outcropping in the fjord (Figure 35). This would make us incline for a thermogenic gas origin, migrating from the deep bedrock sources Agardhfjellet Formation and Botneheia Formation through fluid-flow systems up to the seafloor. However, the hydrographic and bathymetric data results also show clusters of gas flares and pockmarks in tributary fjords such as Tempelfjorden and Billefjorden far from the potential thermogenic gas source (Figure 42). Consequently, in these cases, I argue for an in-situ microbial gas source resulting from microbial activity in the organic-carbon-charged Holocene sediments that seeps via diffuse fluid flow through the sediments.

The different gas sources could also explain the temporal variability and differences in the characteristics of the gas seepage detected over the datasets from early June 2021 and late August 2015. As discussed in the previous hypotheses, we expect to find a stratified water column with warm surface water in June (late spring/early summer conditions) and a better-mixed water column in August (late summer/early autumn). On the one hand, in the early season, the superficial temperature increase could help degrade potential near-shore sub-sea permafrost releasing the methane concentrated beneath the impermeable frozen ground into the water column. Moreover, the temperature rise would increase the activity of the microbial communities found in the superficial sediments boosting the degradation of organic matter and methane formation. However, the deeper waters would remain cold and stable, not releasing any gas. On the other hand, in the late season, the temperature rise would reach the deeper parts of the fjords, causing a potential NGH destabilization and sub-sea permafrost degradation. Moreover, an increase in the salinity of the water from the fjords resulting from more inflow from the North Atlantic current (Skogseth et al., 2020) could shift the gas hydrate stability field, resulting in the destabilization of NGH and finally releasing large amounts of gas into the water column.

The pockmark distribution does not argue against any gas sources since they can be related to the seepage of methane-rich fluids originating either from microbial or thermogenic sources (Liira et al., 2019). Moreover, the reason why pockmarks have not developed over all of the active seepage sites could be due to the coarser nature of the seafloor sediments.

Regarding the differences in the gas flares properties observed in Isfjorden and Van Mijenfjorden, I suggest higher accumulations of shallow subsurface gas seeping to the seafloor in Isfjorden. The gas emissions in Isfjorden could potentially come from NGH destabilizations (Figure 43), while this scenario is improbable to be the case in Van Mijenfjorden since the modeling results do not predict GHSZ in the fjord.

To assess the origin of the gas is necessary to sample and analyze the carbon stable isotopic compositions (δ13C) and C_1:C_{2+} ratio in in-situ gas samples. Thermogenic gas would most likely come from the rich-organic formations and microbial gas from the in-situ methane production within the fjord sediments. In the case of sampling gas with different compositions, it would be necessary to study the sources in more detail. Different authors (Knies et al., 2004; Liira et al., 2019; Roy et al., 2019) suggest a flux of thermogenic gas from deep areas that is probably

microbially oxidated while rising from deep sources, adding a biogenic component to the mixture.

In any case, the shallow depths from the fjords facilitate a direct release of methane to the atmosphere, regardless of the gas source, because the ascending gas bubbles do not have time to dissolve in the water column completely (Figure 43). Because dissolved methane can be oxidized during the transport along the pycnocline (Damm et al., 2005), lower methane concentrations could be expected to reach the water surface in Van Mijenfjorden as water exchange with the shelf is restricted in Van Mijenfjorden. A stronger water column stratification could be established, trapping methane below. Nevertheless, methane concentrations have been described as exceeding the atmospheric equilibrium concentration in both Van Mijenfjorden and Isfjorden (Damm et al., 2005) and being permanently supersaturated in Adventfjorden and Tempelfjorden (Damm et al., 2021).

The methane's atmospheric input is particularly important in the Arctic regions such as Svalbard, a climate-sensitive area, where it would contribute to the atmospheric carbon pool, enhancing climate warming and contributing to the Arctic amplification. That is why it is necessary to further study the mechanisms of gas release and the gas fluxes at the ocean-atmosphere interface and assess how much methane enters the atmosphere.

7. CONCLUSIONS

In this work, I analyzed the spatio-temporal distribution and characteristics of gas flares in Isfjorden over August 2015 and June 2021, and in Van Mijenfjorden, the main fjords of western Spitsbergen. The comparison and assessment of the gas seepage with the geological setting and seabed morphologies have led to the following conclusions:

- A total of 796 flares have been interpreted and characterized in the 2015 dataset. In Isfjorden, 668 flares have been detected over 176.57 km^2, and in Van Mijenfjorden, 115 flares have been detected over 20.14 km^2. In 2021, 152 flares have been interpreted over 110 km^2 in the inner part of Isfjorden and tributary fjords.
- As postulated in the first research objective, the flare intensity, height, and time deflection have proved to be valuable parameters for characterizing the fjords' seepage distribution.
- Uneven ship tracks coverage over the bathymetric relief and outcropping stratigraphic units required normalization of the flare results to make them comparable over time and space.
- As defined in the second research objective, we described the gas flares distribution in the fjords. The analysis of the gas seepage over two different seasons in Isfjorden has proven to be spatially and temporally variable.
- Greater sub-surface methane accumulations might be the reason why the flares detected in Isfjorden are much larger than the ones detected in Van Mijenfjorden.
- Isfjorden's seafloor relief is characterized by parallel ridges and troughs in the NW-SE direction, manifesting large differences in backscatter intensity values. In Van Mijenfjorden, high backscatter values cover part of the western basin.
- The assessment of the third research objective has concluded that pockmarks and flares do not show a clear spatial correlation.
- The areas densely populated with pockmarks manifest low present-day seepage activity. Consequently, I suggest that some of the pockmarks interpreted by Roy et al., 2015 are paleopockmarks caused by a former fluid system that migrated along fault zones, doleritic intrusions and geological unconformities towards the surface.
- The pockmarks located far from the tectonic lineaments could be formed by diffuse fluid flow through the marine sediments or seepage of microbial gas formed in the shallow sediments.

- Following the sixth research objective, I identified the main stratigraphic horizons defining the geological groups and subgroups outcropping in the fjords based on seismic profiles. In Isfjorden, I defined the extent of the Mesozoic organic-rich source rocks (Agardhfjellet and Botneheia Formations) based on well holes and observations onshore.
- The flares detected in the 2015 dataset in Isfjorden were concentrated within Agardhfjellet Formation, Kapp Toscana Group and Botneheia Formation. The flares interpreted from the 2021 dataset were over Janusfjellet Subgroup and Kapp Toscana Group.
- As expected by the quality of the seismic profiles and the high velocity of the sound propagation, no BSR has been recognized in the seismic profiles.
- The observations of many gas flares in Isfjorden and Van Mijenfjorden have proved an active fluid flow system in the fjords. However, I could not prove the fourth research objective, which focused on relating the gas seepage to the presence of NGH.
- Five different hypotheses have been raised as an interpretation of the spatio-temporal variability of the gas seepage detected in the fjords:
    - Hypothesis 1: Following the fifth research objective of this work, I hypothesize that there is strong evidence that stratigraphy and lithology control the fluid flow migration from deep source rocks in Isfjorden.
    - Hypothesis 2: Microbial in-situ gas production in the Holocene sediments is the primary source of the gas seeping in the fjords.
    - Hypothesis 3: The flares detected in Isfjorden result from an inherent subsurface shallow gas accumulation and potential subsea permafrost destabilization.
    - Hypothesis 4: Near-shore NGH dissociation could cause the seepage detected in Isfjorden since most flares from 2015 are distributed within the modeled GHSZ.
    - Hypothesis 5: The gas seepage is a combination of microbial and thermogenic gas result from different sources triggered by a temperature-dependent system.
- I could not estimate the seventh research objective raised at the beginning of this work about the gas diffusion to the atmosphere. Nevertheless, I conclude that the gas seepage detected in the fjords could contribute to direct methane efflux, directly impacting a climate-sensitive area like the Svalbard archipelago, contributing to the atmospheric carbon pool, and enhancing the Arctic amplification.
- Finally, and despite the achievements of this work, more information is needed to better comprehend all the processes for conclusively assessing the origin and fate of methane in the near-shore settings of the fjords of western Spitsbergen.

8. FURTHER RESEARCH QUESTIONS

This study provides an insight into the fluid flow system of the main fjords of western Spitsbergen. Nonetheless, large uncertainties still exist, and further research should be conducted to evaluate if there is atmospheric methane diffusion (efflux) related to the seepage detected in the fjords. In case there is diffusion, it is essential to define the contribution of the methane seeping in the near-shore settings of Spitsbergen to the atmospheric carbon pool. This can be done by linking the 37 surface water samples taken during the GASGEM2021 cruise and further analyzed at the University of Bremen with the CO_2 and CH_4 atmospheric concentration measurements taken during the same cruise.

In addition, assess if there are analogous fluid flow systems in other fjords of the western Spitsbergen with a comparable geological setting. Further knowledge of the extent of Svalbard's petroleum system is needed to assess the energy resource potential and the possible impact on greenhouse gas emissions.

Besides, further monitoring of methane release is needed to quantify the magnitude of future emissions and their potential implications on the regional and global climate. Perform periodic hydrographic surveys to evaluate the extent of the gas seepage in the fjords. Also, sample in-situ gas seeping to define the gas source by analyzing the C_1:C_{2+} ratio and the isotopic methane composition (δ13C). In the case of a microbial source, it is crucial to define the potential formation of microbial gas in the upper part of the sediment and estimate their atmospheric input. Also, determine how does the fresh sediments input influence the microbial gas formation in the fjords. On the contrary, corroborating a thermogenic gas source, it would be essential to identify the active migration pathways.

In turn, more exploration related to the presence of natural gas hydrates is required in the fjords of Spitsbergen to define their area of occurrence. Potential for follow-up research might undertake two approaches - presented next:

- Indirect hydrate indicators: Take sediment samples to measure conductivity, pH, eH, CH_4 and SO_4^{-2} concentrations to assess the potential anaerobic methane oxidation (AMO) and potential NGH formation/dissociation. Moreover, measure the ^{18}O, ^{2}H (deuterium) and sulfate anomalies in pore water, which could relate to NGH destabilizations. Also, take water samples in different depths and analyze CH_4 and C_2H_6 concentrations to understand the gas source and hydrocarbon concentrations in the water column.

- Direct hydrate indicators: Interprete high-resolution seismic profiles looking for the existence of a BSR as a hydrate indicator. Moreover, take direct sediment samples looking for NGH.

In case that it proves the existence of NGH, it is vital to determine the spatial distribution and quantify the gas hydrates sitting in regions of enhanced warming, such as the shallow water environments in the Svalbard fjords. It is necessary to evaluate how much warming there will be, how much hydrate breakdown will result from that warming, how long it will take to destabilize the gas hydrates, and how much methane will be transferred to the atmosphere, acting as a positive feedback of the Arctic amplification and global warming.

9. ACKNOWLEDGEMENTS

This master thesis is the result of the tremendous effort from many people who supported and helped me through this ambitious and exciting project.

First, I would like to express my gratitude to my supervisors for their guidance and support throughout the development of this work. Special and sincere thanks to Peter for supervising and mentoring me during the months of my stay in Svalbard. I highly appreciate your patience in spending so many hours teaching and helping me with Python, your honesty in putting my feet on the ground and keeping my goals realistic, and constantly pushing me to learn and improve. I also want to thank Miriam for always being there to help and guide me during the thesis. I am very grateful to Kim for granting me the opportunity to go to UNIS and provide me with all the tools I needed to move forward. Also, to Gerhard, for welcoming me to your research group in Bremen and making me feel part of it. Finally, to Alexey, for your valuable comments when reviewing the thesis manuscript.

I truly appreciate the support from my friend Wilson, with whom we shared many hours in Germany and Svalbard during the development of our theses, and who helped me in the most challenging moments.

Also to Lukas Frank for joining the fieldwork and Lara Marschall for working side by side and helping with all the logistics related to the cruise.

I sincerely acknowledge the help and advice received from David Amblàs while preparing my first research cruise. Likewise, the support received from Srikumar Roy, who has always been willing to share his knowledge and experience with me, and Aleksandra Anna Smyrak-Sikora, for corroborating my seismic interpretations. Also, Martin Liira who, despite not being able to join the cruise, has always been willing to participate in the project since the beginning. Finally, to Andy Hodson and Eleanor Jones, for supporting and borrowing us crucial equipment needed for the fieldwork.

I also want to gratefully thank the captain of the Czech R/V Clione, Jan Pechar, and the best technician Jiri Štojdl, for your help and patience during the GASGEM cruise. Your essential assistance helped us make the fieldwork possible and acquire all the data we needed for the project.

I am deeply grateful to NORBIT Subsea for borrowing us one of their outstanding multibeam systems. Namely, Anna Dunaeva and Aleksandra Kruss, for believing in helping us and provided us with excellent equipment and training.

Finally, my parents have always encouraged and supported me in moving forward, despite being so far apart.

Mention that this thesis has received the support of the Research Council of Norway via the Arctic Field Grant 2021, and that part of the bathymetric information shown in the figures comes from data provided by the Norwegian Hydrographic Service and the Norwegian Mapping Authority.

Last but not least, sincere thanks to the University Centre in Svalbard for having me as a guest master student during my thesis and enabling me to get to know the Arctic of Svalbard first hand. Ultimately, acknowledge Saint Petersburg State University, Hamburg University, Bremen University and the Federal Ministry of Education and Research, project ”CATS synthesis: The Changing Arctic Transpolar System”, FKZ 03F0831A, and all the managers of the Master Program for Polar and Marine Sciences for the economic and academic support during these months.

10. REFERENCES

Abay, T. B., Karlsen, D. A., Lerch, B., Olaussen, S., Pedersen, J. H., & Backer-Owe, K. (2017). Migrated Petroleum in Outcropping Mesozoic Sedimentary Rocks in Spitsbergen: Organic Geochemical Characterization and Implications for Regional Exploration. Journal of Petroleum Geology, 40(1), 5–36. doi: 10.1111/jpg.12662

Abay, T. B., Karlsen, D. A., & Pedersen, J. H. (2014). Source Rocks at Svalbard : An Overview of Jurassic and Triassic Formations and Comparison with Offshore Barents Sea Time Equivalent Source Rock Formations. AAPG International Conference & Exhibition, 30372, #30372.

Archer, D. (2007), Methane hydrate stability and anthropogenic climate change, Biogeosciences, 4, 521–544, doi:10.5194/bg-4-521-2007.

Audsley, A., Bradwell, T., Howe, J., & Baxter, J. (2021). Spatial Relationships between Pockmarks and Sub-Seabed Gas in Fjordic Settings: Evidence from Loch Linnhe, West Scotland. Geosciences, 11(7), 283. doi: 10.3390/geosciences11070283

Bælum, K., & Braathen, A. (2012). Along-strike changes in fault array and rift basin geometry of the Carboniferous Billefjorden Trough, Svalbard, Norway. Tectonophysics, 546–547, 38–55. doi: 10.1016/j.tecto.2012.04.009

Betlem, P., Senger, K., & Hodson, A. (2019). 3D thermobaric modelling of the gas hydrate stability zone onshore central Spitsbergen, Arctic Norway. Marine and Petroleum Geology, 100(November 2018), 246–262. doi: 10.1016/j.marpetgeo.2018.10.050

Betlem, P., Roy, S., Birchall, T., Hodson, A., Noormets, R., Römer, M., Skogseth, R., & Senger, K. (2021). Modelling of the gas hydrate potential in Svalbard's fjords. Journal of Natural Gas Science and Engineering, 94(April), 104127. doi: 10.1016/j.jngse.2021.104127

Birchall, T., Jochmann, M., Betlem, P., Senger, K., Hodson, A., and Olaussen, S. (2021). Review Article: Permafrost Trapped Natural Gas in Svalbard, Norway, The Cryosphere Discuss. [preprint], https://doi.org/10.5194/tc-2021-226, in review.

Bjorøy, M., Hall, P. B., Ferriday, I. L., & Mørk, A. (2010). Triassic source rocks of the Barents Sea and Svalbard. Search and Discovery, 10219, 7pp.

Blinova, M., Faleide, J. I., Gabrielsen, R. H., & Mjelde, R. (2013). Analysis of structural trends of sub-sea-floor strata in the Isfjorden area of the West Spitsbergen Fold-and-Thrust Belt based on multichannel seismic. Journal of the Geological Society, 170(4), 657–668. doi: 10.1144/jgs2012-109

Blinova, M., Inge Faleide, J., Gabrielsen, R. H., & Mjelde, R. (2012). Seafloor expression and shallow structure of a fold-and-thrust system, Isfjorden, west Spitsbergen. Polar Research, 31(1), 11209. doi: 10.3402/polar.v31i0.11209

Bohrmann, G., & Torres, M. E. (2006). Gas hydrates in marine sediments. Marine Geochemistry, 481–512. doi: 10.1007/3-540-32144-6_14

Braathen, A., Bælum, K., Christiansen, H. H., Dahl, T., Eiken, O., Elvebakk, H., Hansen, F., Hanssen,

T. H., Jochmann, M., Johansen, T. A., Johnsen, H., Larsen, L., Lie, T., Mertes, J., Mørk, A., Mørk, M. B., Nemec, W., Olaussen, S., Oye, V., Vagle, K. (2012). The longyearbyen CO2 lab of svalbard, norway-initial assessment of the geological conditions for CO2 sequestration. Norsk Geologisk Tidsskrift, 92(4), 353–376.

Collett, T. S., A. H. Johnson, C. C. Knapp, and R. Boswell. (2009), Natural gas hydrates: A review, in Natural Gas Hydrates—Energy Resource Potential and Associated Geologic Hazards, edited by T. Collett et al., AAPG Mem., 89, 146–219, doi:10.1306/13201101M891602.

Cooper, A.K., Hart, P.E. (2003). High-resolution seismic-reflection investigation of the northern Gulf of Mexico gas-hydrate-stability zone. Mar. Petr. Geol. 19,1275–1293.

Dale, A. W., Van Cappellen, P., Aguilera, D. R., & Regnier, P. (2008). Methane efflux from marine sediments in passive and active margins: Estimations from bioenergetic reaction-transport simulations. Earth and Planetary Science Letters, 265(3–4), 329–344. doi: 10.1016/j.epsl.2007.09.026

Dallmann W.K. (1999). Lithostratigraphic lexicon of Svalbard. Tromsø: Norwegian Polar Institute.

Dallmann, W.K., Elvevold, S., Gerland, S., Hormes, A., Majka, J., Ottemöller, L., Pavlova, O., Sander, G., (2015). Geoscience Atlas of Svalbard. Norsk Polar Institutt.

Damm, E., Ericson, Y., & Falck, E. (2021). Waterside convection and stratification control methane spreading in supersaturated Arctic fjords (Spitsbergen). Continental Shelf Research, 224, 104473. doi: 10.1016/j.csr.2021.104473

Damm, E., Mackensen, A., Budéus, G., Faber, E., & Hanfland, C. (2005). Pathways of methane in seawater: Plume spreading in an Arctic shelf environment (SW-Spitsbergen). Continental Shelf Research, 25(12–13), 1453–1472. doi: 10.1016/j.csr.2005.03.003

Dickens, G. R. (2011). Down the rabbit hole: Toward appropriate discussion of methane release from gas hydrate systems during the Paleocene–Eocene thermal maximum and other past hyperthermal events. Clim. Past 7, 1139–1174.

Dunkley-Jones, T.D., Ridgwell, A., Lunt, D., Maslin, M., Schmidt, D. And Valdes, P. (2010). A Palaeogene perspective on climate sensitivity and methane hydrate instability. Philos. T. R. Soc. Lond., 368, 2395-2415

Eckerstorfer, M., & Christiansen, H. (2011). The “high arctic maritime snow climate” in Central Svalbard. Arctic, Antarctic, and Alpine Research, 43(1), 11–21. doi: 10.1657/1938-4246-43.1.11

Etiope, G. (2015). Gas Seepage Classification and Global Distribution. In Natural Gas Seepage. doi: 10.1007/978-3-319-14601-0_2

Forwick, M., Baeten, N. J., & Vorren, T. O. (2009). Pockmarks in Spitsbergen fjords. Norsk Geologisk Tidsskrift, 89(1–2), 65–77.

Forwick, M., & Vorren, T. O. (2009). Late Weichselian and Holocene sedimentary environments and ice rafting in Isfjorden, Spitsbergen. Palaeogeography, Palaeoclimatology, Palaeoecology, 280(1–2), 258–274. doi: 10.1016/j.palaeo.2009.06.026

Forwick, M., & Vorren, T. O. (2010). Stratigraphy and deglaciation of the Isfjorden area, Spitsbergen. Norsk Geologisk Tidsskrift, 90(4), 163–179.

Greinert, J., McGinnis, D. F., Naudts, L., Linke, P., & De Batist, M. (2010). Atmospheric methane flux from bubbling seeps: Spatially extrapolated quantification from a Black Sea shelf area. Journal of Geophysical Research: Oceans, 115(1), 1–18. doi: 10.1029/2009JC005381

Hald, M. and Korsun, S. (1997). Distribution of modern Arctic benthic foraminifera from fjords of Svalbard. Journal of Foraminiferal Research 27, 101–22.

Hald, M., Dahlgren, T., Olsen, T.-E. and Lebesbye, E. (2001). Late Holocene paleoceanography in Van Mijenfjorden, Svalbard. Polar Research 20, 23–35.

Harland, W.B. (1969). Contribution of Spitsbergen to Understanding of Tectonic Evolution of North Atlantic Region: Chapter 58: Arctic Regions.

Harland, W.B., Cutbill, J., Friend, P.F., Gobbett, D.J., Holliday, D., Maton, P., Parker, J., Wallis, R.H. (1974). The Billefjorden Fault Zone, Spitsbergen: The long history of a major tectonic lineament.

Henriksen, E., Bjørnseth, H. M., Hals, T. K., Heide, T., Kiryukhina, T., Kløvjan, O. S., Larssen, G. B., Ryseth, A. E., Rønning, K., Sollid, K., & Stoupakova, A. (2011). Chapter 17: Uplift and erosion of the greater Barents Sea: Impact on prospectivity and petroleum systems. Geological Society Memoir, 35(2004), 271–281. doi: 10.1144/M35.17

Hodson, A. J., Nowak, A., Hornum, M. T., Senger, K., Redeker, K., Christiansen, H. H., Jessen, S., Betlem, P., Thornton, S. F., Turchyn, A. V., Olaussen, S., & Marca, A. (2020). Sub-permafrost methane seepage from open-system pingos in Svalbard. Cryosphere, 14(11), 3829–3842. doi: 10.5194/tc-14-3829-2020

Hornbach, M. J., Ruppel, C., & Van Dover, C. L. (2007). Three-dimensional structure of fluid conduits sustaining an active deep marine cold seep. Geophysical Research Letters, 34(5). doi: 10.1029/2006GL028859

Hovland, M., Judd, A.G., Burke, R. A. (1993). The global flux of methane from shallow submarine sediments. Chemosphere, 00226020(3), 1–8.

Ingólfsson, Ó. (2011). Geological Society, London, Special Publications Fingerprints of Quaternary glaciations on Svalbard service Fingerprints of Quaternary glaciations on Svalbard. 15–31. doi: 10.1144/SP354.2

IPCC, 2013: Climate Change 2013: The Physical Science Basis. Contribution of Working Group I to the Fifth Assessment Report of the Intergovernmental Panel on Climate Change [Stocker, T.F., D. Qin, G.-K. Plattner, M. Tignor, S.K. Allen, J. Boschung, A. Nauels, Y. Xia, V. Bex and P.M. Midgley (eds.)]. Cambridge University Press, Cambridge, United Kingdom and New York, NY, USA, 1535 pp.

Isaksen, K., Nordli, Ø., Førland, E. J., Łupikasza, E., Eastwood, S. (2016). Recent warming on Spitsbergen—Influence of atmospheric circulation and sea ice cover. Journal of Geophysical Research Atmospheres, 3446–3464. doi: 10.1002/2016JD025606

Jakobsson, M., L. A. Mayer, B. Coakley, J. A. Dowdeswell, S. Forbes, B. Fridman, H. Hodnesdal, R.

Noormets, R. Pedersen, M. Rebesco, H.-W. Schenke, Y. Zarayskaya A, D. Accettella, A. Armstrong, R. M. Anderson, P. Bienhoff, A. Camerlenghi, I. Church, M. Edwards, J. V. Gardner, J. K. Hall, B. Hell, O. B. Hestvik, Y. Kristoffersen, C. Marcussen, R. Mohammad, D. Mosher, S. V. Nghiem, M. T. Pedrosa, P. G. Travaglini, and P. Weatherall. (2012). The International Bathymetric Chart of the Arctic Ocean (IBCAO) Version 3.0, Geophysical Research Letters, doi: 10.1029/2012GL052219

Judd, A., & Hovland, M. (2007). Seabed fluid flow: the impact on geology, biology, and the marine environment. Choice Reviews Online, 45(01), 45-0294-45–0294. doi: 10.5860/choice.45-0294

Knies, J., Damm, E., Gutt, J., Mann, U., & Pinturier, L. (2004). Near-surface hydrocarbon anomalies in shelf sediments off Spitsbergen: Evidences for past seepages. Geochemistry, Geophysics, Geosystems, 5(6). doi: 10.1029/2003GC000687

Koevoets, M.J., Abay, T.B., Hammer, Ø., Olaussen, S. (2016). High-resolution organic carbon–isotope stratigraphy of the middle Jurassic–lower cretaceous Agardhfjellet formation of central Spitsbergen, Svalbard. Palaeogeogr. Palaeoclimatol. Palaeoecol. 449, 266–274. http://dx.doi.org/10.1016/j.palaeo.2016.02.029.

Koevoets, M. J., Hammer, Ø., Olaussen, S., Senger, K., & Smelror, M. (2018). Integrating subsurface and outcrop data of the middle jurassic to lower cretaceous agardhfjellet formation in central spitsbergen. Norsk Geologisk Tidsskrift, 98(4), 1–34. doi: 10.17850/njg98-4-01

Koevoets, M. J., Hammer, Ø., & Little, C. T. S. (2019). Palaeoecology and palaeoenvironments of the Middle Jurassic to lowermost Cretaceous Agardhfjellet Formation (Bathonian–Ryazanian), Spitsbergen, Svalbard. Norwegian Journal of Geology, 99(1), 1–24. doi: 10.17850/njg99-1-02

Kretschmer, K., Biastoch, A., Rüpke, L., & Burwicz, E. (2015). Modeling the fate of methane hydrates under global warming. Global Biogeochemical Cycles, 29(5), 610–625. doi: 10.1002/2014GB005011

Kvenvolden, K.A. (1988). Methane hydrates and global climate. Global Biogeochemical Cycles 2: 221-229

Kvenvolden, K.A. (1993). Gas hydrates—geological perspective and global change. Rev. Geophys. 31, 173–187. https://doi.org/10.1029/93RG00268.

Kvenvolden, K.A. (1998). A primer on the geological occurrence of gas hydrate. Geol. Soc. Lond. Spec. Publ. 137 (1), 9–30. 01.02. http://dx.doi.org/10.1144/GSL.SP.1998.137.

Kvenvolden, K. A., Lorenson, T. D., & Reeburgh, W. S. (2001). Attention turns to naturally occurring methane seepage. Eos, 82(40), 457. doi: 10.1029/01EO00275

Kvenvolden, K. A., & Rogers, B. W. (2005). Gaia's breath - Global methane exhalations. Marine and Petroleum Geology, 22(4 SPEC. ISS.), 579–590. doi: 10.1016/j.marpetgeo.2004.08.004

Ligtenberg, J.H. (2005). Detection of fluid migration pathways in seismic data: implications for fault seal analysis. Basin Research 17, 141-153.

Liira, M., Noormets, R., Sepp, H., Kekišev, O., Maddison, M., & Olaussen, S. (2019). Sediment geochemical study of hydrocarbon seeps in Isfjorden and Mohnbukta: a comparison between western and eastern Spitsbergen, Svalbard. Arktos, 5(1), 49–62. doi: 10.1007/s41063-019-00067-7

Lowell, J. D. (1972). Spitsbergen Tertiary orogenic belt and Spitsbergen fracture zone. Geological Society of America Bulletin 83 (10), 3091-3101.

Maher, H.D., Craddock, H.D. & Maher, K.A. (1986). Kinematics of Tertiary structure in Upper Paleozoic and Mesozoic strata on Midterhuken, West Spitsbergen. Geological Society of America Bulletin 97, 1411-1421.

Maher, H.D. Jr. (2001). Manifestation of the High Arctic large igneous province in Svalbard. Journal of geology 109, 91-104.

Mau, S., Römer, M., Torres, M. E., Bussmann, I., Pape, T., Damm, E., Geprägs, P., Wintersteller, P., Hsu, C. W., Loher, M., & Bohrmann, G. (2017). Widespread methane seepage along the continental margin off Svalbard-from Bjørnøya to Kongsfjorden. Scientific Reports, 1–13. doi: 10.1038/srep42997

McGinnis, D. F., Greinert, J., Artemov, Y., Beaubien, S. E., & Wüest, A. (2006). Fate of rising methane bubbles in stratified waters: How much methane reaches the atmosphere? Journal of Geophysical Research: Oceans, 111(9), 1–15. doi: 10.1029/2005JC003183

Mienert, J., Vanneste, M., Bünz, S., Andreassen, K., Haflidason, H., & Sejrup, H. P. (2005). Ocean warming and gas hydrate stability on the mid-Norwegian margin at the Storegga Slide. Marine and Petroleum Geology, 22(1-2 SPEC. ISS.), 233–244. doi: 10.1016/j.marpetgeo.2004.10.018

Minshull, T. A., Marín-Moreno, H., Betlem, P., Bialas, J., Bünz, S., Burwicz, E., Cameselle, A. L., Cifci, G., Giustiniani, M., Hillman, J. I. T., Hölz, S., Hopper, J. R., Ion, G., León, R., Magalhaes, V., Makovsky, Y., Mata, M. P., Max, M. D., Nielsen, T., Vázquez, J. T. (2020). Hydrate occurrence in Europe: A review of available evidence. Marine and Petroleum Geology, 111(March 2019), 735–764. doi: 10.1016/j.marpetgeo.2019.08.014

Mørk, A. & Bjorøy, M. (1984). Mesozoic source rocks on Svalbard. Pp. 371-382 in Spencer, A.M. Et al. (eds.): Petroleum geology of the north European margin. Norwegian Petroleum Society, Graham & Trotman, London.

Nicolaisen, J.B., Elvebakk, G., Ahokas, J., Bojesen-Koefoed, J.A., Olaussen, S., Rinna, J., Skeie, J.E., Stemmerik, L. (2019). Characterization of upper Palaeozoic organic-rich units in Svalbard: Implications for the petroleum systems of the Norwegian Barents Shelf. J. Petrol. Geol. 42 (1), 59–78. http://dx.doi.org/10.1111/jpg.12724.

Nilsen, F., Cottier, F., Skogseth, R., & Mattsson, S. (2008). Fjord-shelf exchanges controlled by ice and brine production: The interannual variation of Atlantic Water in Isfjorden, Svalbard. Continental Shelf Research, 28(14), 1838–1853. doi: 10.1016/j.csr.2008.04.015

Nordli, Ø., Przybylak, R., Ogilvie, A. E. J., & Isaksen, K. (2014). Long-term temperature trends and variability on Spitsbergen: The extended Svalbard airport temperature series, 1898-2012. Polar Research, 33(1 SUPPL). doi: 10.3402/polar.v33.21349

Nøttvedt, A., Livbjerg, F., Midbøe, P.S., Rasmussen, E. (1993). Hydrocarbon Potential of the Central Spitsbergen Basin, vol. 2. Norwegian Petroleum Society Special Publications, pp. 333–361. https://doi.org/10.1016/B978-0-444-88943-0.50026-5.

Ogata, K., Senger, K., Braathen, A., Tveranger, J., & Olaussen, S. (2014). Fracture systems and mesoscale structural patterns in the siliciclastic Mesozoic reservoir-caprock succession of the Longyearbyen CO2 lab project: Implications for geological CO2 sequestration in central Spitsbergen, Svalbard. Norsk Geologisk Tidsskrift, 94(2–3), 121–154.

Ohm, S.E., Larsen, L., Olaussen, S., Senger, K., Birchall, T., Demchuk, T., Hodson, A., Johansen, I., Titlestad, G.O., Karlsen, D.A., Braathen, A. (2019). Discovery of shale gas in organic rich Jurassic successions, Adventdalen, Central Spitsbergen, Norway. Nor. J. Geol. 99 (2), http://dx.doi.org/10.17850/njg007.

Paech, H.-J., Koch, J. (2001). Coalification in post-Caledonian sediments on Spitsbergen. Geologisches Jahrbuch Reihe B 507–534.

Paull, C.K., R. Matsumoto, P. J. Wallace, and Shipboard Scientific Party. (1996), Proceedings of the Ocean Drilling Program, Initial Report, vol. 164, Ocean Drill. Program, College Station, Tex.

Paull, C.K., Ussler Iii,W., Borowski,W.S. (1999). Freshwater ice rafting: an additional mechanism for the formation of some high-latitude submarine pockmarks. Geo-Mar. Lett. 19, 164–168.

Roy, S., Senger, K., Noormets, R., & Hovland, M. (2012). Pockmarks in the fjords of western Svalbard and their implications on gas hydrate dissociation. EGU General Assembly 2012, 14, 8960. Retrieved from http://adsabs.harvard.edu/abs/2012EGUGA.14.8960R

Roy, S., Senger, K., Braathen, A., Noormets, R., Hovland, M., & Olaussen, S. (2014). Fluid migration pathways to seafloor seepage in inner isfjorden and Adventfjorden, Svalbard. Norsk Geologisk Tidsskrift, 94(2–3), 99–199.

Roy, S., Hovland, M., Noormets, R., & Olaussen, S. (2015). Seepage in Isfjorden and its tributary fjords, West Spitsbergen. Marine Geology, 363, 146–159. doi: 10.1016/j.margeo.2015.02.003

Roy, S., Hovland, M., & Braathen, A. (2016). Evidence of fluid seepage in Grønfjorden, Spitsbergen: Implications from an integrated acoustic study of seafloor morphology, marine sediments and tectonics. Marine Geology, 380, 67–78. doi: 10.1016/j.margeo.2016.07.002

Roy, S., Senger, K., Hovland, M., Römer, M., & Braathen, A. (2019). Geological controls on shallow gas distribution and seafloor seepage in an Arctic fjord of Marine and Petroleum Geology, 107(May), 237–254. doi: 10.1016/j.marpetgeo.2019.05.021 Spitsbergen, Norway.

Ruppel, C. (2011), Methane hydrates and contemporary climate change, Nat. Educ. Knowl., 3(10), 29. [Available at http://www.nature.com/scitable/knowledge/library/methane-hydrates-and-contemporary-climate-change-24314790.]

Ruppel, C. D., & Kessler, J. D. (2017). The interaction of climate change and methane hydrates.

Reviews of Geophysics, 55(1), 126–168. doi: 10.1002/2016RG000534

Sain, K., Rajesh, V., Satyavani, N., Subbarao, K. V., & Subrahmanyam, C. (2011). Gas-hydrate stability thickness map along the Indian continental margin. Marine and Petroleum Geology, 28(10), 1779–1786. doi: 10.1016/j.marpetgeo.2011.03.008

Salomatin, A.S., & Yusupov, V.I. (2011). Acoustic investigations of gas "flares" in the Sea of Okhotsk. Oceanology, 51(5), 857–865. doi: 10.1134/S0001437011050134

Schmale, O., J. Greinert, and G. Rehder (2005), Methane emission from high-intensity marine gas seeps in the Black Sea into the atmosphere, Geophys. Res. Lett., 32, L07609, doi:10.1029/2004GL021138.

Senger, K., Roy, S., Braathen, A., Buckley, S. J., Bælum, K., Gernigon, L., Mjelde, R., Noormets, R., Ogata, K., Olaussen, S., Planke, S., Ruud, B. O., & Tveranger, J. (2013). Geometries of doleritic intrusions in central Spitsbergen, Svalbard: an integrated study of an onshore-offshore magmatic province with implications for CO2 sequestration. 143–166.

Senger, K., Betlem, P., Liira, M., Roy, S., Midttømme, K., Wheeler, W., & Beka, T. (2017). Integrated thermo-baric modeling of the gas hydrate stability zone onshore Svalbard, Arctic Norway. Ninth International Conference on Gas Hydrates, 4.

Senger, K., Brugmans, P., Grundvåg, S. A., Jochmann, M., Nøttvedt, A., Olaussen, S., Skotte, A., & Smyrak-Sikora, A. (2019). Petroleum, coal and research drilling onshore svalbard: A historical perspective. Norsk Geologisk Tidsskrift, 99(3), 1–30. doi: 10.17850/njg99-3-1

Shakhova, N., Semiletov, I., Salyuk, A., Yusupov, V., Kosmach, D.Ö.G. (2010). Extensive Methane Venting to the Atmosphere from Sediments of the East Siberian Arctic Shelf. Scientific Reports, 4(March), 1246–1251.

Shindell, D. T., Faluvegi, G., Koch, D. M., Schmidt, G. a, Unger, N., & Bauer, S. E. (2009). Improved Attribution of Climate Forcing to Emissions. Scientific Reports, 326(x), 716–718.

Shipley, T.H., Houston, M.H. and Buffler, R.T. (1979). Seismic evidence for widespread possible gas hydrate horizons on continental slopes and rises. AAPG Bull., 63, 2204-2213

Skogseth, R., Olivier, L.L.A., Nilsen, F., Falck, E., Fraser, N., Tverberg, V., Ledang, A. B., Vader, A., Jonassen, M. O., Søreide, J., Cottier, F., Berge, J., Ivanov, B. V., & Falk-Petersen, S. (2020). Variability and decadal trends in the Isfjorden (Svalbard) ocean climate and circulation – An indicator for climate change in the European Arctic. Progress in Oceanography, 187, 102394. doi: 10.1016/j.pocean.2020.102394

Sloan, E.D. (1998). Clathrate Hydrate of Natural Gases. Marcel Dekker, New York.

Steel, R.J. and Worsley, D. (1984). Svalbard's post-Caledonian strata – an atlas of sedimentational patterns and palaeogeographic evolution. In: Spencer, A.M., Mørk, A., Nysæther, E., Songstad, P. and Spinnanger, Å. (Eds), Johnsen, O.S., Petroleum geology of the North European margin. Graham and Trotman, London, 109-135.

Teyssier, C., Kleinspehn, K., Pershing, J. (1995). Analysis of fault populations in western Spitsbergen: implications for deformation partitioning along transform margins. Geol. Soc. Am. Bull. 107, 68–82.

Tenkanen, H., & Heikinheimo, V. (2020). Department of Geosciences and Geography, University of Helsinki. https://autogis-site.readthedocs.io/en/latest/notebooks/L3/06_nearest-neighbor-faster.html

Vanneste, M., Guidard, S., Mienert, J. (2005). Bottom-simulating reflections and geothermal gradients across the western Svalbard margin. Terra Nova 17, 510–516.

Veloso, M., Greinert, J., Mienert, J., and De Batist, M. (2015). A New Methodology for Quantifying Bubble Flow Rates in Deep Water Using Splitbeam Echosounders: Examples from the A Rctic Offshore NW- Svalbard. Limnol. Oceanogr. Methods 13 (6), 267–287. doi:10.1002/lom3.10024

Westbrook, G.K., Thatcher, K.E., Rohling, E.J., Piotrowski, A.M., Pälike, H., Osborne, A.H., Nisbet, E.G., Minshull, T.A., Lanoisellé, M., James, R.H., Hühnerbach, V., Green, D., Fisher, R.E., Crocker, A.J., Chabert, A., Bolton, C., Beszczynska-Möller, A., Berndt, C., Aquilina, A. (2009). Escape of methane gas from the seabed along the West Spitsbergen continental margin. Geophys. Res. Lett. 36 (15), http://dx.doi.org/10.1029/2009GL039191.

Winkelmann, D. and Knies, J. (2005). Recent distribution and accumulation of organic carbon on the continental margin west off Spitsbergen. Geochemistry Geophysics Geosystems G3 doi:10.1029/2005GC000916.

Włodarska-Kowalczuk, M., Mazurkiewicz, M., Górska, B., Michel, L. N., Jankowska, E., Zaborska, A. (2019). Organic carbon origin, benthic faunal consumption and burial in sediments of northern Atlantic and Arctic fjords (60–81 N), J. Geophys. Res.-Biogeo.,124, 3737–3751.

Worsley, D., Aga, O.J. (1986). The Geological History of Svalbard. Statoil, Stavanger.

Worsley, D. (2008). The post-Caledonian development of Svalbard and the western Barents Sea.Polar Res. 27 (3), 298–317. http://dx.doi.org/10.1111/j.1751-8369.2008.00085.x.

APPENDIX 1. Raw data

Stratigraphic unit	Flares Isfjorden 2015			Flares Van Mijenfjorden 2015			Flares Isfjorden 2021		
	Total	%	Normalized (%)	Total	%	Normalized (%)	Total	%	Normalized (%)
Van Mijenfjorden Group	59	8,83	11,11	8	6,95	22,16	0	0,0	0,0
Adventdalen Group	24	3,59	9,85	26	22,61	15,84	0	0,0	0,0
Janusfjellet Sub Group	60	8,98	3,48	78	67,82	47,27	66	43,42	35,38
Agardhfjellet Formation	129	19,31	29,10	NaN	NaN	NaN	1	0,66	5,89
Kapp Toscana Group	307	45,96	25,64	0	0	0	22	14,47	13,89
Botneheia Formation	71	10,63	15,94	NaN	NaN	NaN	16	10,53	9,17
Sassendalen Group	18	2,69	4,87	3	2,61	15,48	0	0,0	0,0
Tempelfjorden Group	0	0,0	0,0	0	0	0	20	13,16	16,98
Gipsdalen Group	0	0,0	0,0	0	0	0	27	17,76	18,66

Table 2. Flare distribution within stratigraphic units.

Stratigraphic unit	Ship track Isfjorden 2015		Ship track Van Mijenfjorden 2015		Ship track Isfjorden 2021 (Total)		Ship track Isfjorden 2021 (<150 m)	
	Total	%	Total	%	Total	%	Total	%
Van Mijenfjorden Group	9437	5,21	8710	8,84	0	0	0	0
Adventdalen Group	4333	2,39	41599	42,21	0	0	0	0
Janusfjellet Sub Group	30662	16,92	39824	40,41	32879	23,21	21178	31,30
Agardhfjellet Formation	7880	4,35	NaN	NaN	7768	5,48	569	0,84
Kapp Toscana Group	21285	11,75	4677	4,75	30355	21,43	6763	9,99
Botneheia Formation	7917	4,37	NaN	NaN	23757	16,77	8627	12,75
Sassendalen Group	6567	3,62	3381	3,43	13404	9,46	3554	5,25
Tempelfjorden Group	40621	22,42	351	0,35	15755	11,12	9245	13,66
Gipsdalen Group	52467	28,96	0	0	17721	12,51	17721	26,19

Table 3. Ship track distribution within stratigraphic units.

Stratigraphic unit	Pockmarks Isfjorden			Faults Isfjorden			Area Isfjorden		Area Van Mijenfjorden	
	Total	%	Normalized (%)	Total	%	Normalized (%)	Total (km2)	%	Total (km2)	%
Van Mijenfjorden Group	18	1,44	1,37	80485	13,21	11,89	250,22	11,50	257,31	50,49
Adventdalen Group	69	5,54	6,17	45033	7,39	7,79	213,69	9,82	152,35	29,89
Janusfjellet Sub Group	83	6,66	3,97	161170	26,45	14,91	399,53	18,37	59,76	11,73
Agardhfjellet Formation	12	0,96	2,82	54814	8,99	24,98	81,09	3,73	NaN	NaN
Kapp Toscana Group	272	21,85	18,45	127485	20,92	16,73	281,57	12,95	11,70	2,29
Botneheia Formation	151	12,13	14,79	27819	4,56	5,27	194,98	8,96	NaN	NaN
Sassendalen Group	174	13,97	24,19	28041	4,60	7,54	137,42	6,32	26,18	5,4
Tempelfjorden Group	152	12,21	12,87	41421	6,79	6,79	225,55	10,37	2,27	0,45
Gipsdalen Group	314	25,22	15,35	43051	7,06	4,07	390,71	17,96	0	0

Table 4. Pockmarks and faults distribution within stratigraphic units. Also total area of each unit outcropping in the fjords.

Distance (km)	Flares Isfjorden 2015			Flares Isfjorden 2021			Pockmarks Isfjorden	
	Total	%	Normalized (%)	Total	%	Normalized (%)	Total	%
0-1	44	6,58	9,74	37	24,34	18,76	36	2,85
1-2	96	14,37	5,33	62	40,78	26,14	213	16,86
2-3	95	14,22	3,69	25	16,45	21,17	257	20,35
3-4	52	7,78	5,24	24	15,79	26,16	142	11,24
4-5	54	8,08	5,45	4	2,63	7,75	171	13,54
5-6	67	10,03	5,83	0	0,0	0,0	107	8,47
6-7	111	16,61	4,40	0	0,0	0,0	156	12,35
7-8	61	9,13	10,20	0	0,0	0,0	120	9,50
8-9	37	5,54	7,75	0	0,0	0,0	30	2,37
9-10	34	5,08	8,75	0	0,0	0,0	24	1,90
10-11	14	2,09	19,85	0	0,0	0,0	5	0,39
> 11	3	0,45	13,73	0	0,0	0,0	2	0,16

Table 5. Flare and pockmark distance distribution from the coastline.

	Ship track Isfjorden 2015		Ship track Isfjorden 2021 (Total)		Ship track Isfjorden 2021 (<150 m)	
Distance (km)	Total	%	Total	%	Total	%
0-1	8042	3,75	18645	13,16	18056	26,69
1-2	32065	14,96	26117	18,44	21716	32,09
2-3	45823	21,38	20649	14,58	10815	15,98
3-4	17673	8,25	21736	15,34	8400	12,41
4-5	17634	8,23	16691	11,78	4725	6,98
5-6	20443	9,54	11778	8,31	1437	2,12
6-7	44896	20,95	12666	8,94	1163	1,72
7-8	10647	4,97	8475	5,98	1000	1,48
8-9	8502	3,97	3580	2,53	345	0,51
9-10	6914	3,22	1211	0,85	0	0,0
10-11	1256	0,58	91	0,064	0	0,0
> 11	389	0,18	0	0,0	0	0,0

Table 6. Ship track distribution in 1 km distance bins from the coastline in Isfjorden.

	Flares Van Mijenfjorden 2015		Ship track Van Mijenfjorden 2015	
Distance (m)	Total	%	Total	%
0-500	0	0,0	438	0,44
5000-1000	0	0,0	2626	2,65
1000-1500	11	9,56	4719	4,77
1500-2000	6	5,22	3913	3,95
2000-2500	10	8,695	9699	9,79
2500-3000	27	23,48	8065	8,14
3000-3500	20	17,39	10196	10,29
3500-4000	2	1,74	4890	4,94
4000-4500	18	15,65	6307	6,37
4500-5000	13	11,30	41423	41,84
> 5500	8	6,95	6724	6,79

Table 7. Flares and ship track distribution in 500 m distance bins from the coastline in Van Mijenfjorden.

Table 8. Flare and pockmark distribution by depth (10 m bins).

	Flares Isfjorden 2015			Flares Van Mijenfjorden 2015			Flares Isfjorden 2021			Pockmarks	
Depth range (m)	Total	%	Normalized (%)	Total	%	Normalized (%)	Total	%	Normalized (%)	Total	%
0-10	0	0,0	0,0	0	0,0	0,0	0	0,0	0,0	0	0,0
10-20	0	0,0	0,0	0	0,0	0,0	7	4,76	14,38	0	0,0
20-30	0	0,0	0,0	0	0,0	0,0	9	6,12	11,78	0	0,0
30-40	2	0,29	1,09	8	7,14	27,66	15	10,20	11,98	0	0,0
40-50	0	0,0	0,0	0	0,0	0,0	22	14,96	20,33	4	0,31
50-60	0	0,0	0,0	0	0,0	0,0	13	8,84	9,11	23	1,76
60-70	0	0,0	0,0	2	1,78	5,33	23	15,64	8,51	33	2,53
70-80	1	0,14	0,18	6	5,35	22,66	19	12,92	6,52	49	3,76
80-90	1	0,14	0,22	8	7,14	11,92	18	12,24	6,29	62	4,76
90-100	8	1,17	3,59	7	6,25	10,33	9	6,12	3,17	34	2,61
100-110	24	3,52	9,29	52	46,43	13,72	4	2,72	2,82	48	3,68
110-120	17	2,49	8,24	29	25,89	8,35	1	0,68	0,74	45	3,45
120-130	3	0,44	0,77	NaN	NaN	NaN	3	2,04	1,79	44	3,38
130-140	12	1,76	3,45	NaN	NaN	NaN	2	1,36	1,78	55	4,22
140-150	37	5,43	6,32	NaN	NaN	NaN	0	0,0	0,0	117	8,98
150-160	53	7,78	2,66	NaN	NaN	NaN	0	0,0	0,0	155	11,90
160-170	32	4,69	6,81	NaN	NaN	NaN	0	0,0	0,0	59	4,53
170-180	55	8,07	6,68	NaN	NaN	NaN	0	0,0	0,0	85	6,53
180-190	68	9,98	2,66	NaN	NaN	NaN	1	0,68	0,28	91	6,99
190-200	73	10,72	9,37	NaN	NaN	NaN	0	0,0	0,0	113	8,68
200-210	44	6,46	6,91	NaN	NaN	NaN	0	0,0	0,0	92	7,06
210-220	39	5,73	4,88	NaN	NaN	NaN	0	0,0	0,0	60	4,61
220-230	71	10,42	7,09	NaN	NaN	NaN	0	0,0	0,0	22	1,69
230-240	31	4,55	3,46	NaN	NaN	NaN	1	0,68	0,47	30	2,30
240-250	44	6,46	5,82	NaN	NaN	NaN	0	0,0	0,0	22	1,69
250-260	46	6,75	4,68	NaN	NaN	NaN	0	0,0	0,0	30	2,30
260-270	11	1,61	2,72	NaN	NaN	NaN	0	0,0	0,0	26	1,99
270-280	9	1,32	3,05	NaN	NaN	NaN	0	0,0	0,0	3	0,23

Table 9. Ship track distribution by depth (10 m bins).

	Ship track Isfjorden 2015		Ship track Van Mijenfjorden 2015		Ship track Isfjorden 2021 (Total)		Ship track Isfjorden 2021 (<150 m)	
Depth range (m)	Total	%	Total	%	Total	%	Total	%
0-10	0	0,0	0	0,0	24	0,02	24	0,04
10-20	898	0,35	0	0,0	1333	0,96	1333	2,06
20-30	1401	0,54	421	0,44	2092	1,51	2092	3,23
30-40	2505	0,97	2763	2,88	3426	2,47	3426	5,29
40-50	2256	0,87	2009	2,09	2963	2,13	2963	4,57
50-60	26108	10,09	2351	2,45	3905	2,81	3905	6,03
60-70	14492	5,60	3582	3,73	7398	5,33	7398	11,43
70-80	7513	2,90	2529	2,63	7970	5,74	7970	12,31
80-90	6026	2,33	6412	6,68	7826	5,64	7826	12,09
90-100	3052	1,18	6471	6,75	7769	5,60	7769	11,99
100-110	3542	1,37	36200	37,75	3887	2,80	3887	6,00
110-120	2828	1,09	33154	34,57	3674	2,65	3674	5,67
120-130	5317	2,05	NaN	NaN	4582	3,30	4582	7,08
130-140	4757	1,84	NaN	NaN	3060	2,20	3060	4,73
140-150	8026	3,10	NaN	NaN	5883	4,24	4834	7,46
150-160	27296	10,55	NaN	NaN	7393	5,33	0	0,0
160-170	6439	2,49	NaN	NaN	6216	4,48	0	0,0
170-180	11291	4,37	NaN	NaN	8875	6,39	0	0,0
180-190	34996	13,53	NaN	NaN	9678	6,97	0	0,0
190-200	10685	4,13	NaN	NaN	9295	6,70	0	0,0
200-210	8735	3,38	NaN	NaN	6759	4,87	0	0,0
210-220	10959	4,24	NaN	NaN	5905	4,25	0	0,0
220-230	13735	5,31	NaN	NaN	7752	5,59	0	0,0
230-240	12275	4,75	NaN	NaN	5755	4,15	0	0,0
240-250	10363	4,01	NaN	NaN	1833	1,32	0	0,0
250-260	13483	5,21	NaN	NaN	3183	2,29	0	0,0
260-270	5537	2,14	NaN	NaN	289	0,21	0	0,0
270-280	4050	1,56	NaN	NaN	0	0,0	0	0,0

APPENDIX 2. Figures

Southern Isfjorden

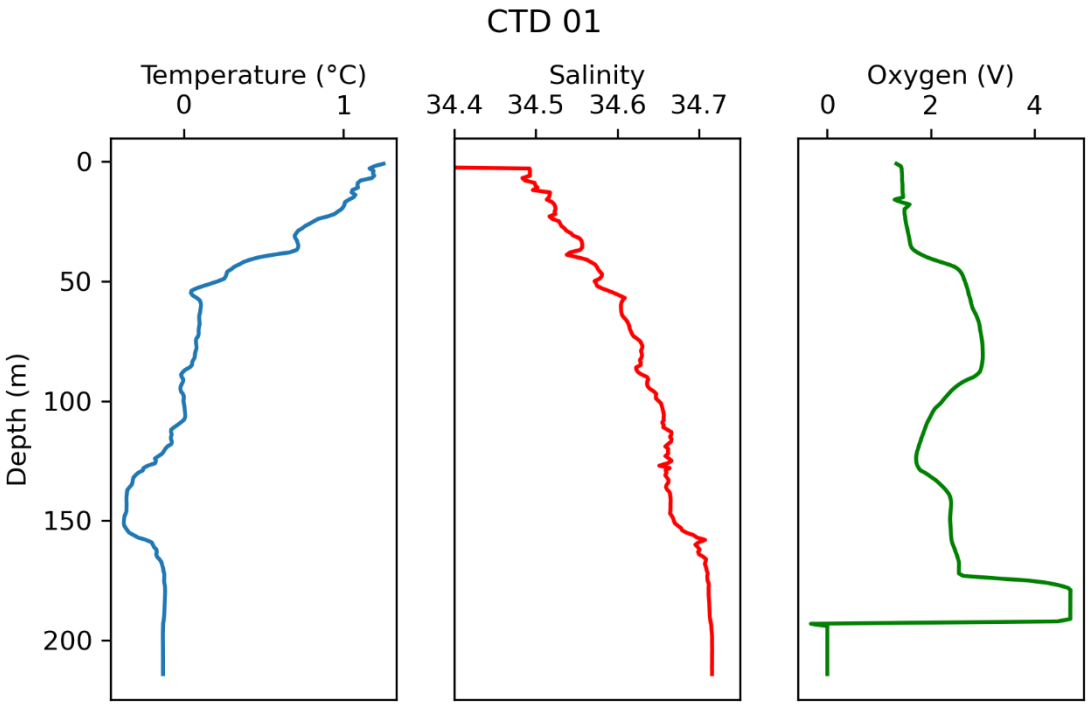

Figure appx2.1. Temperature, salinity and oxygen profiles for the CTD01 (Figure 20 for location).

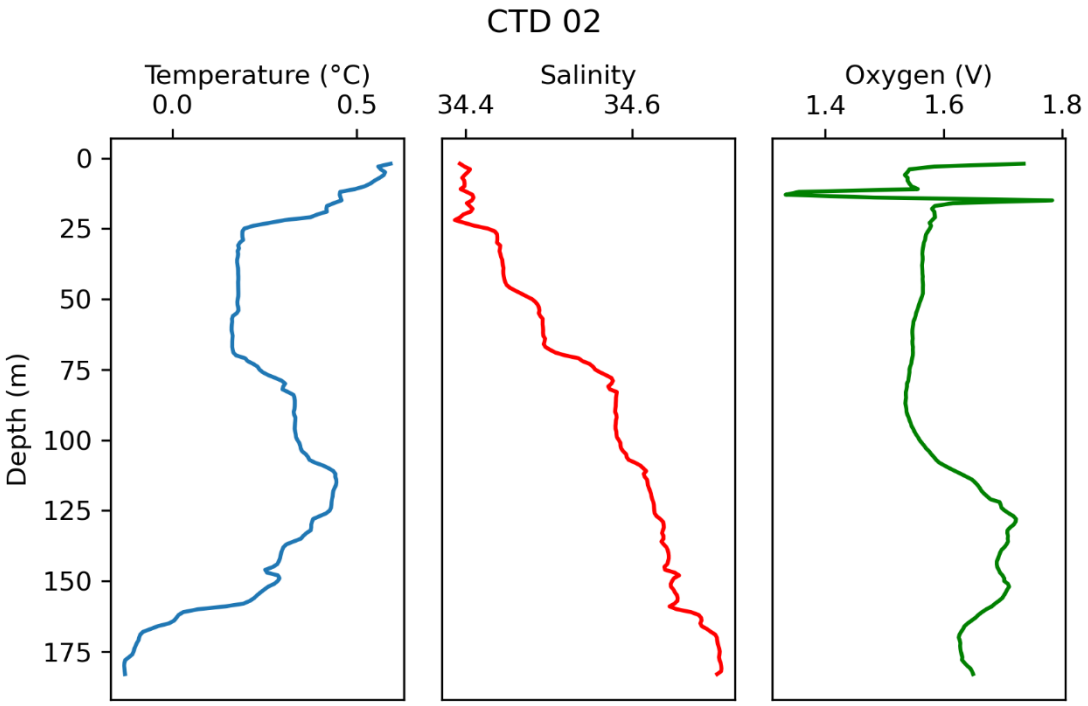

Figure appx2.2. Temperature, salinity and oxygen profiles for the CTD02 (Figure 20 for location).

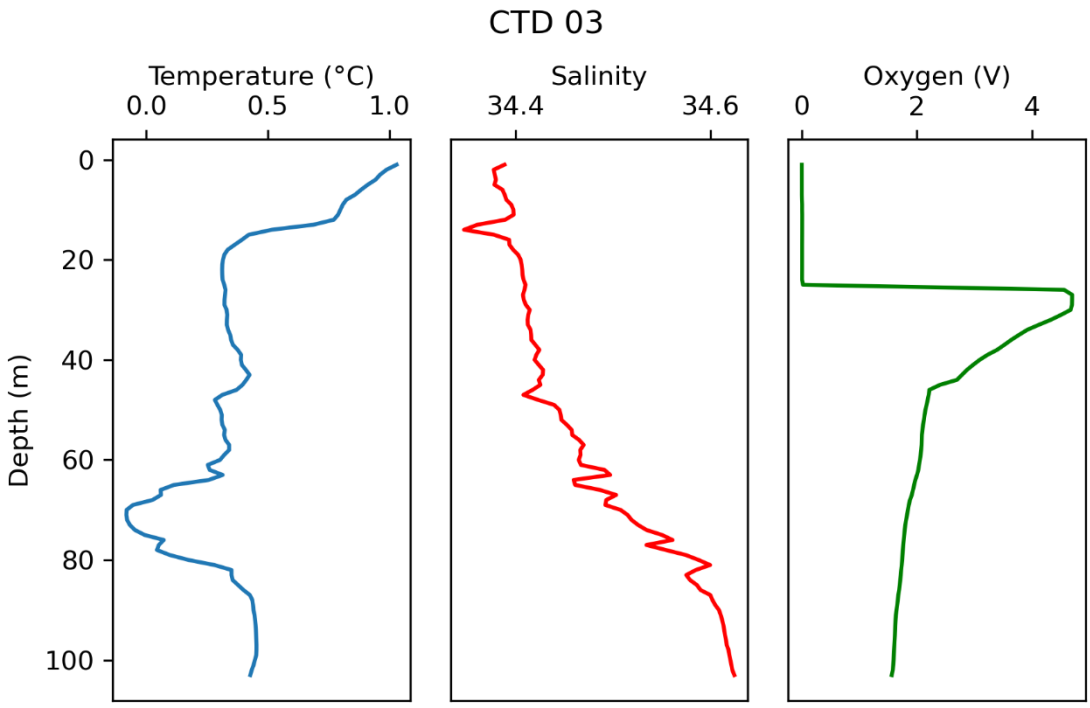

Figure appx2.3. Temperature, salinity and oxygen profiles for the CTD03 (Figure 20 for location).

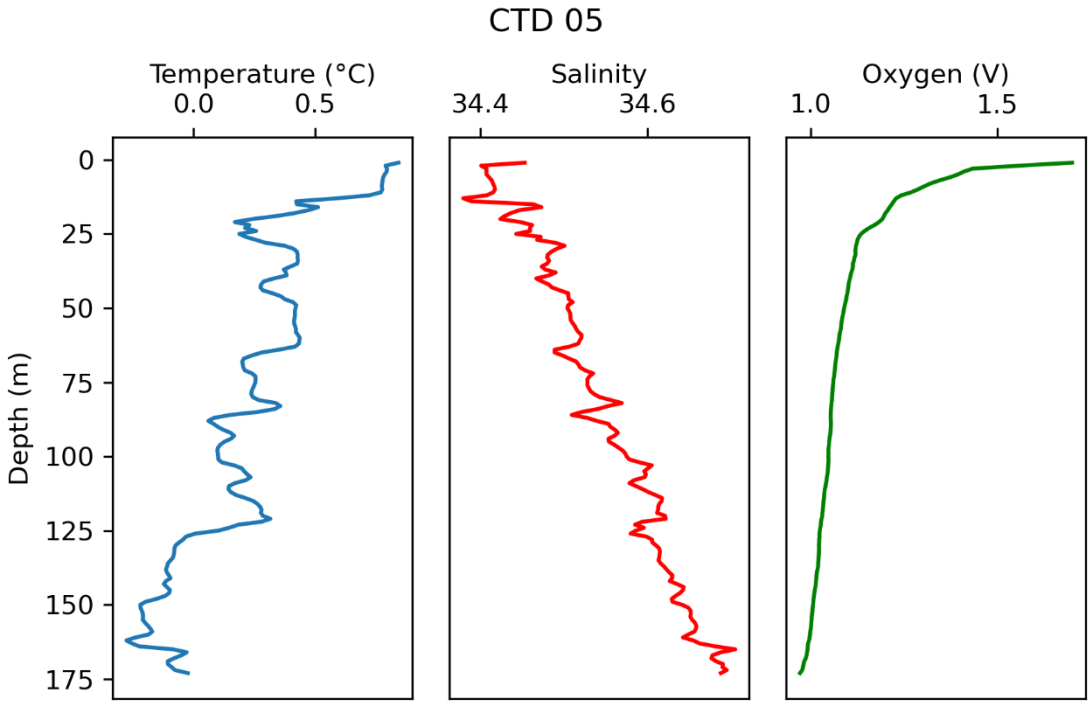

Figure appx2.4. Temperature, salinity and oxygen profiles for the CTD05 (Figure 20 for location).

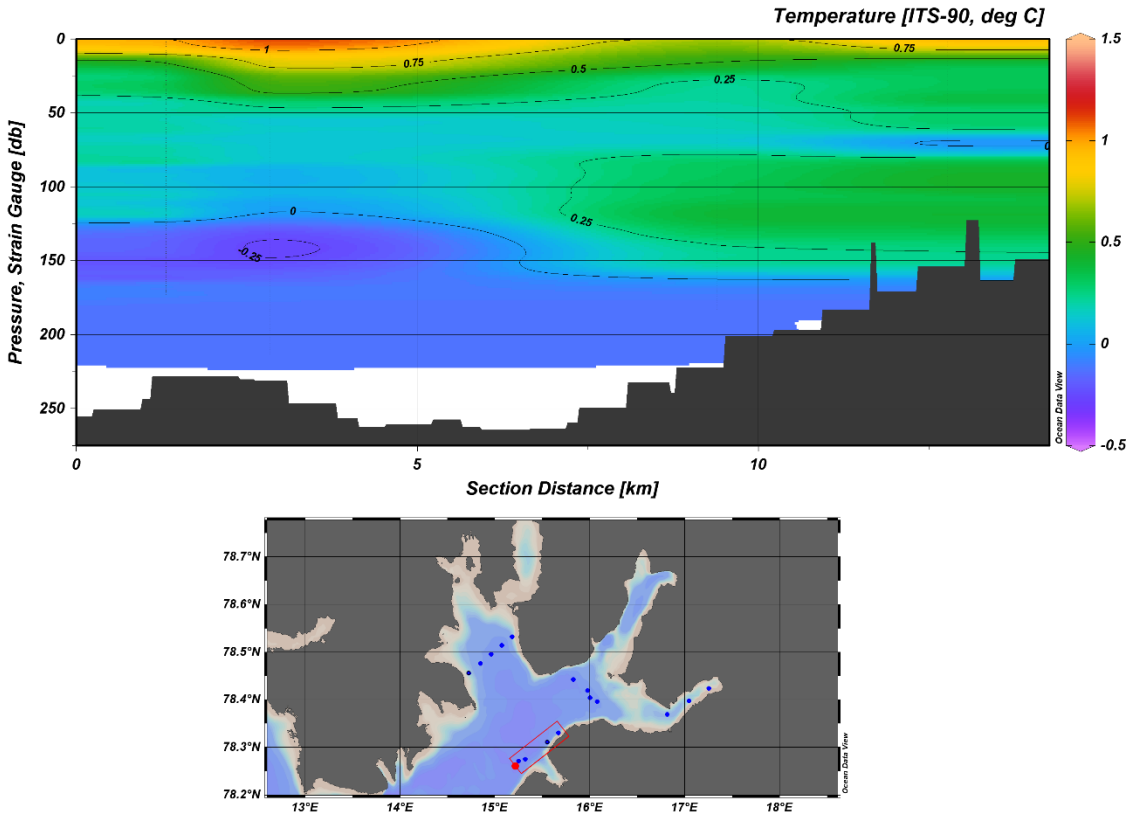

Figure appx2.5. Temperature profile from the southern Isfjorden transect.

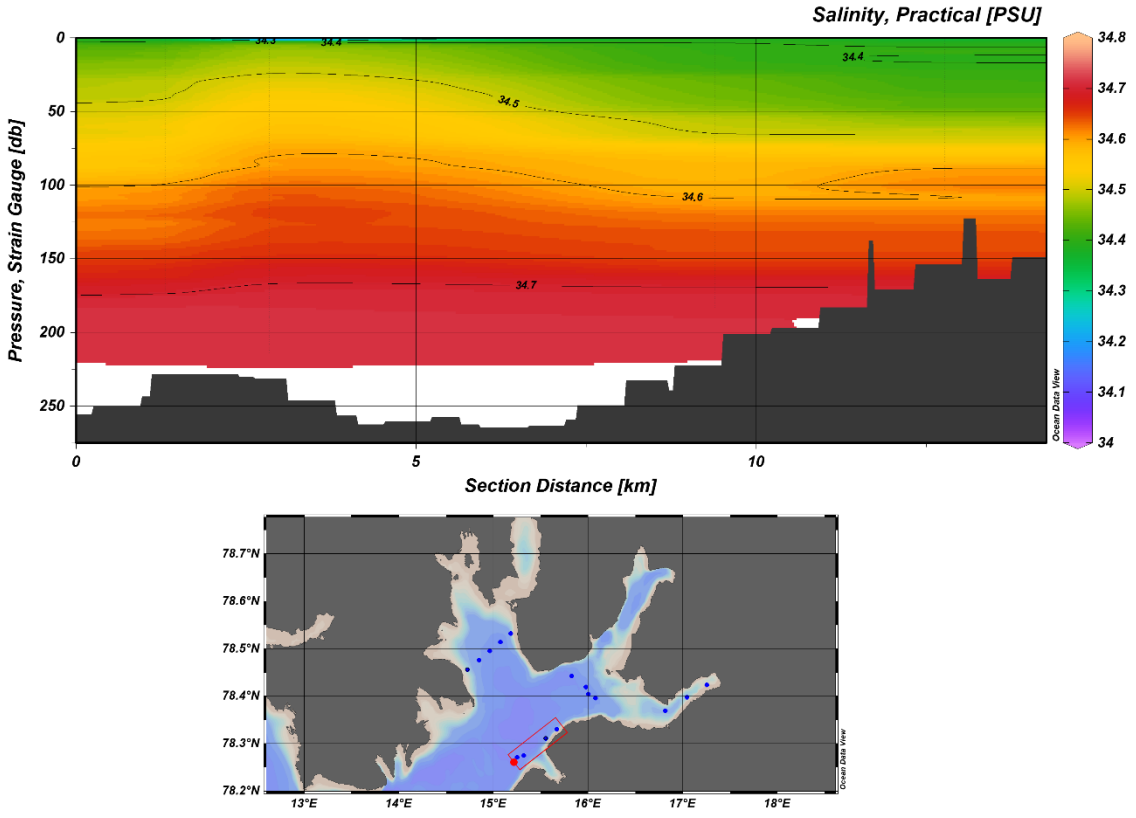

Figure appx2.6. Salinity profile from the southern Isfjorden transect.

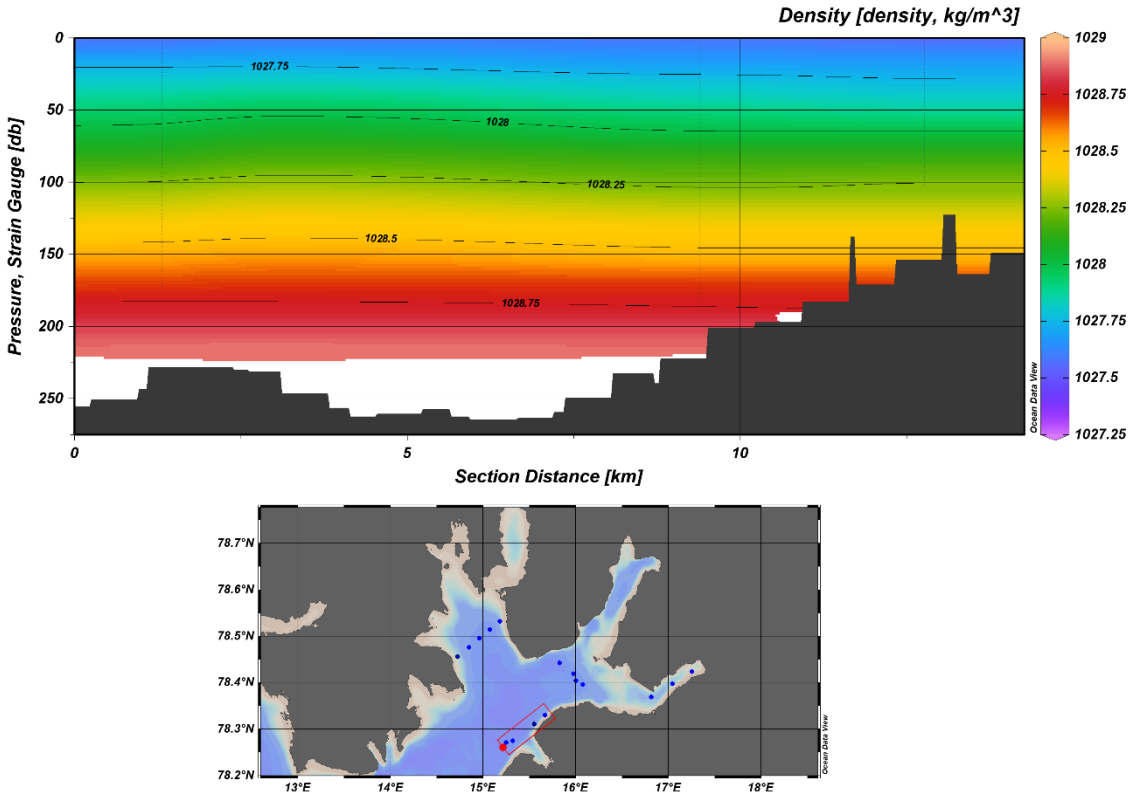

Figure appx2.7. Density profile from the southern Isfjorden transect.

Eastern Isfjorden

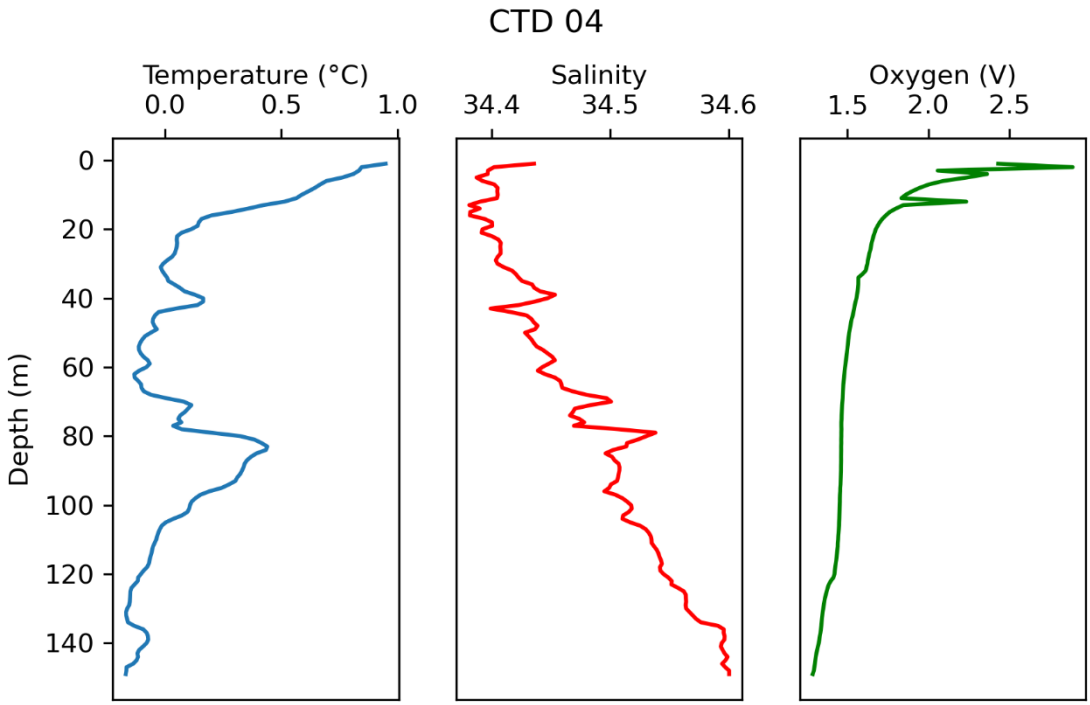

Figure appx2.8. Temperature, salinity and oxygen profiles for the CTD04 (Figure 20 for location).

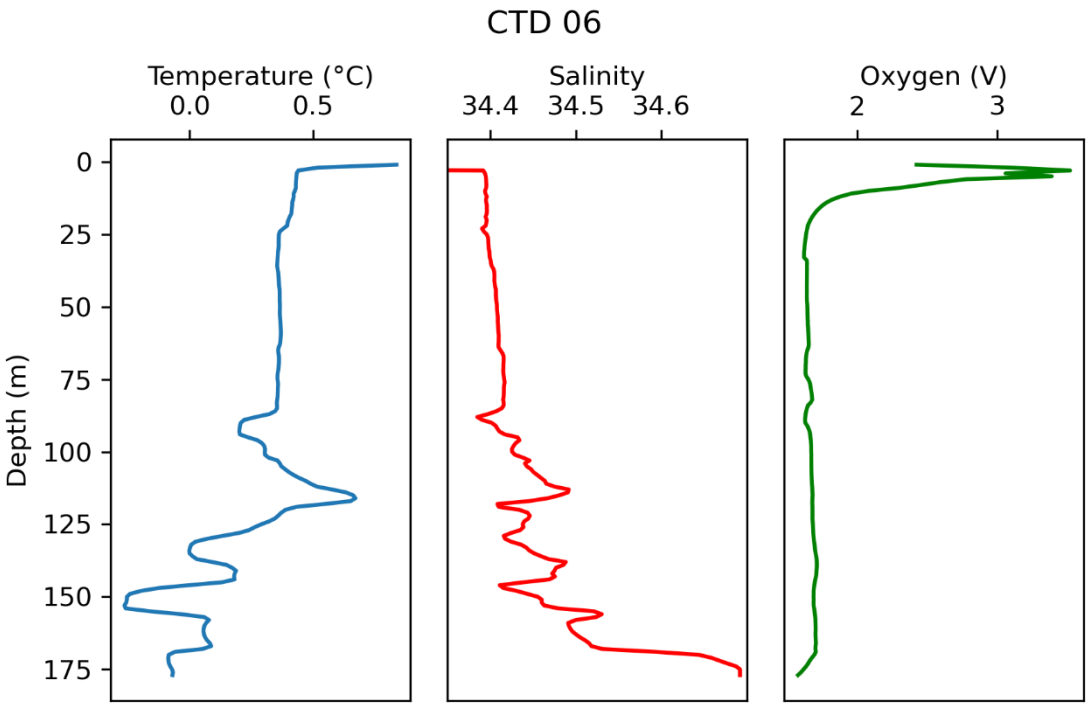

Figure appx2.9. Temperature, salinity and oxygen profiles for the CTD06 (Figure 20 for location).

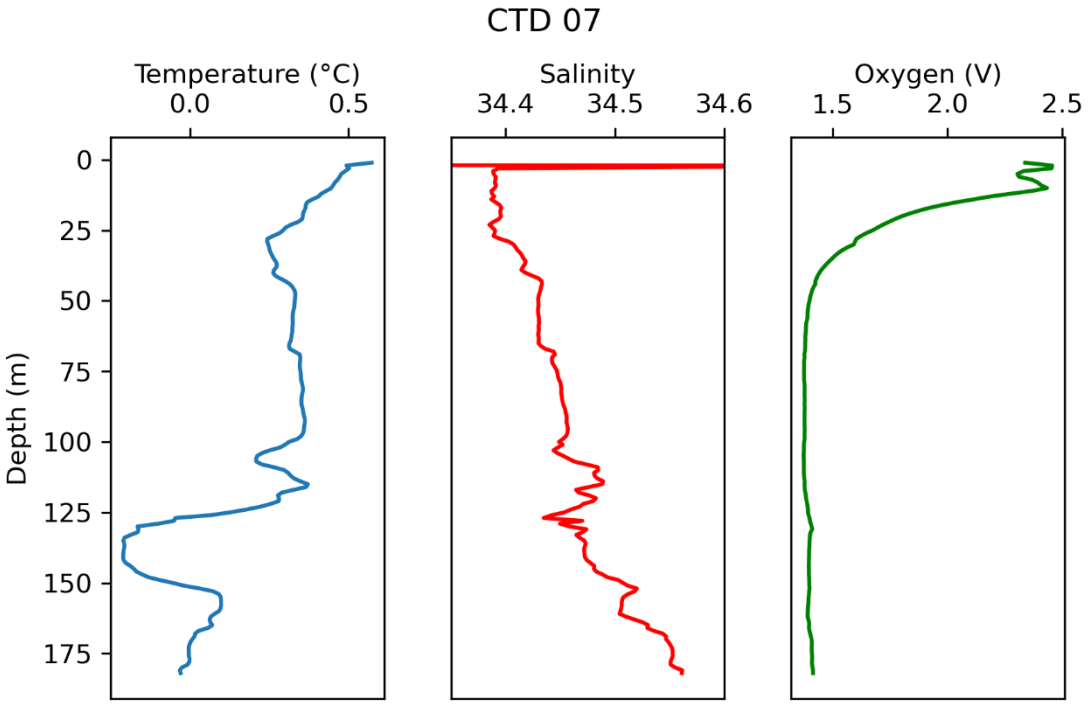

Figure appx2.10. Temperature, salinity and oxygen profiles for the CTD07 (Figure 20 for location).

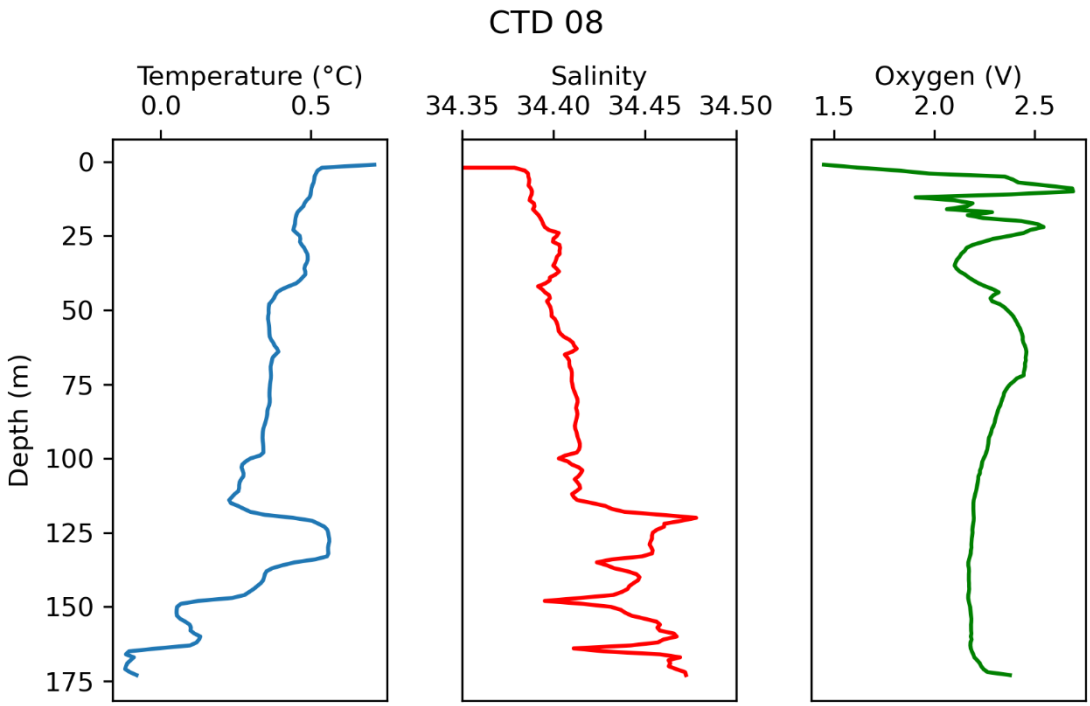

Figure appx2.11. Temperature, salinity and oxygen profiles for the CTD08 (Figure 20 for location).

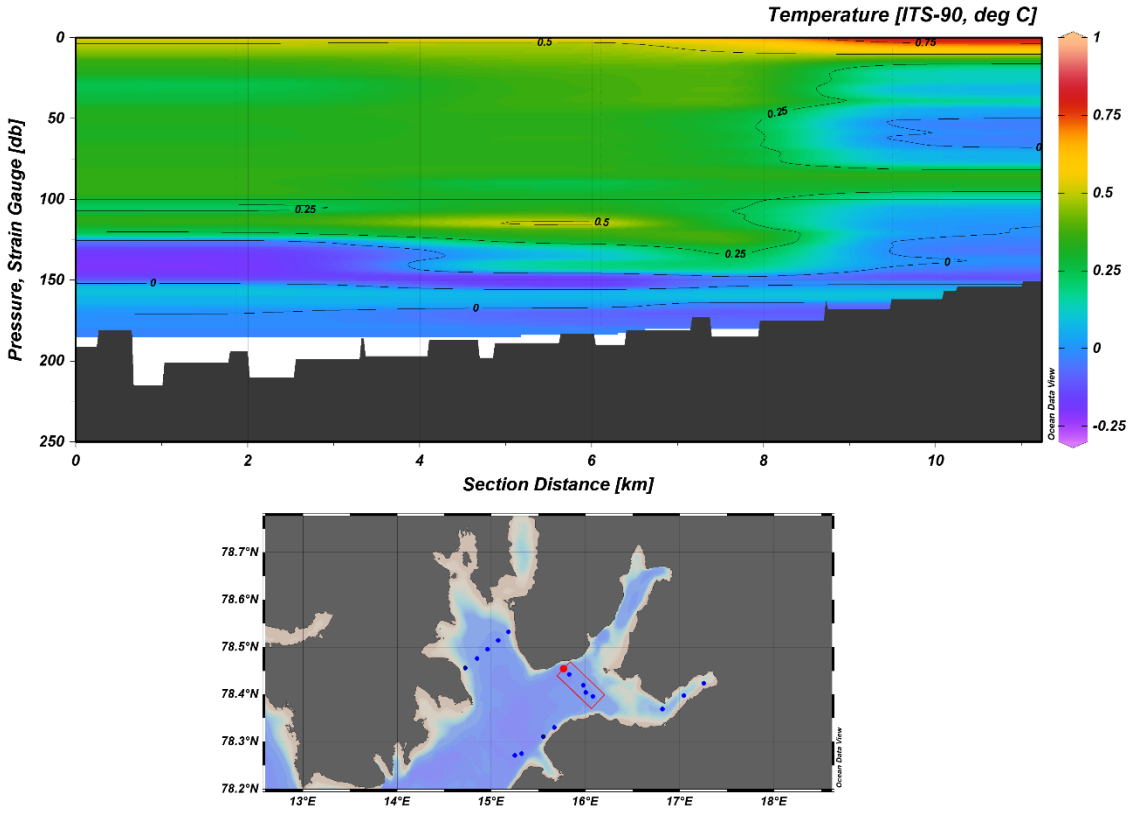

Figure appx2.12. Temperature profile from the eastern transect.

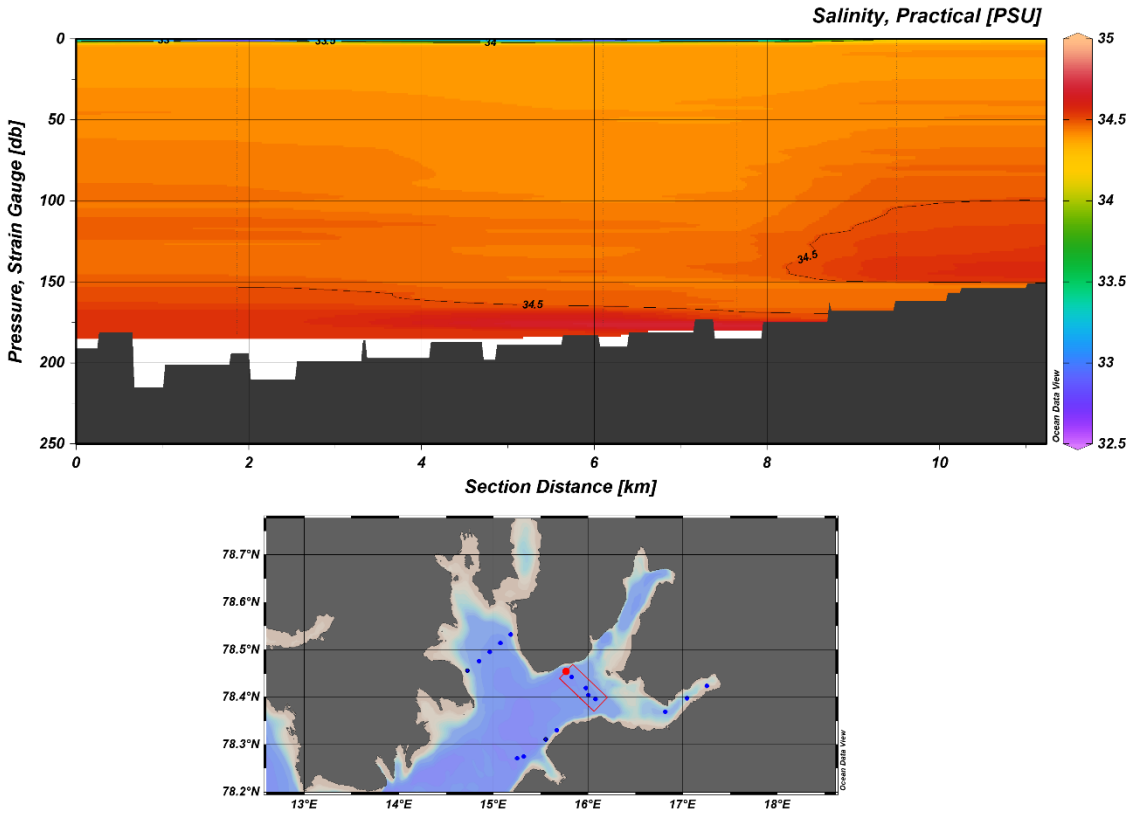

Figure appx2.13. Salinity profile from the eastern transect.

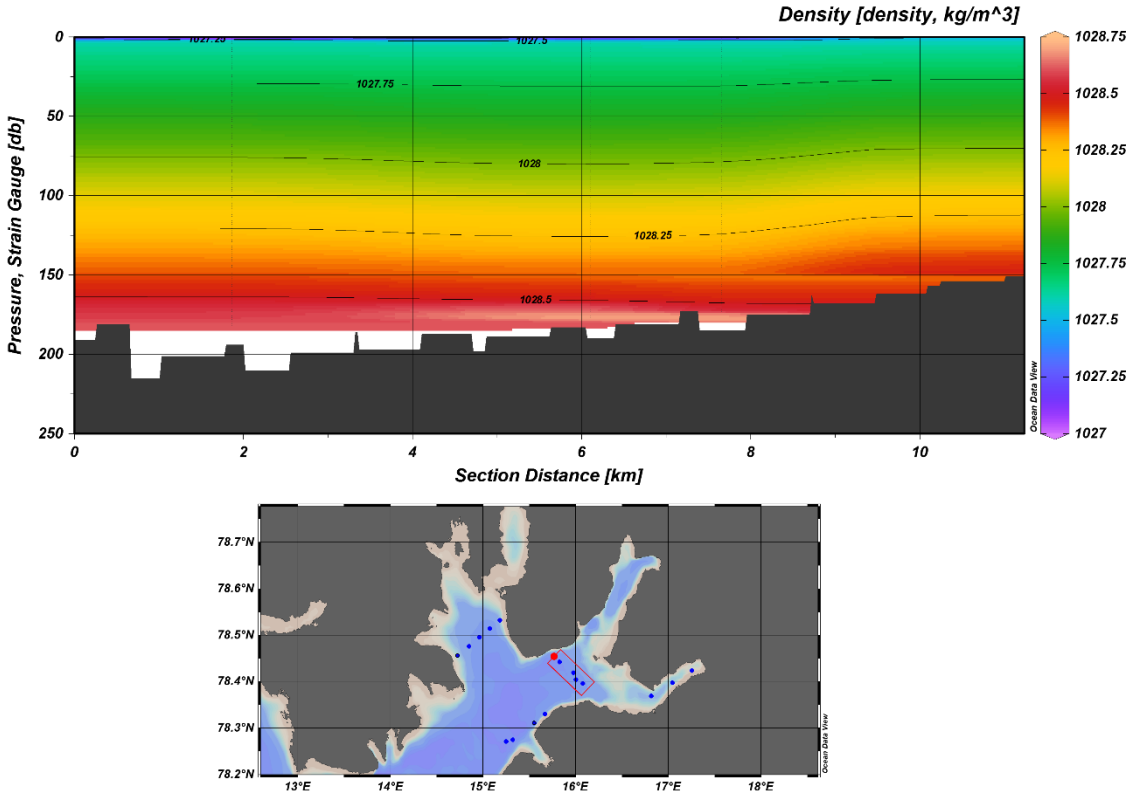

Figure appx2.14. Density profile from the eastern transect.

Tempelfjorden

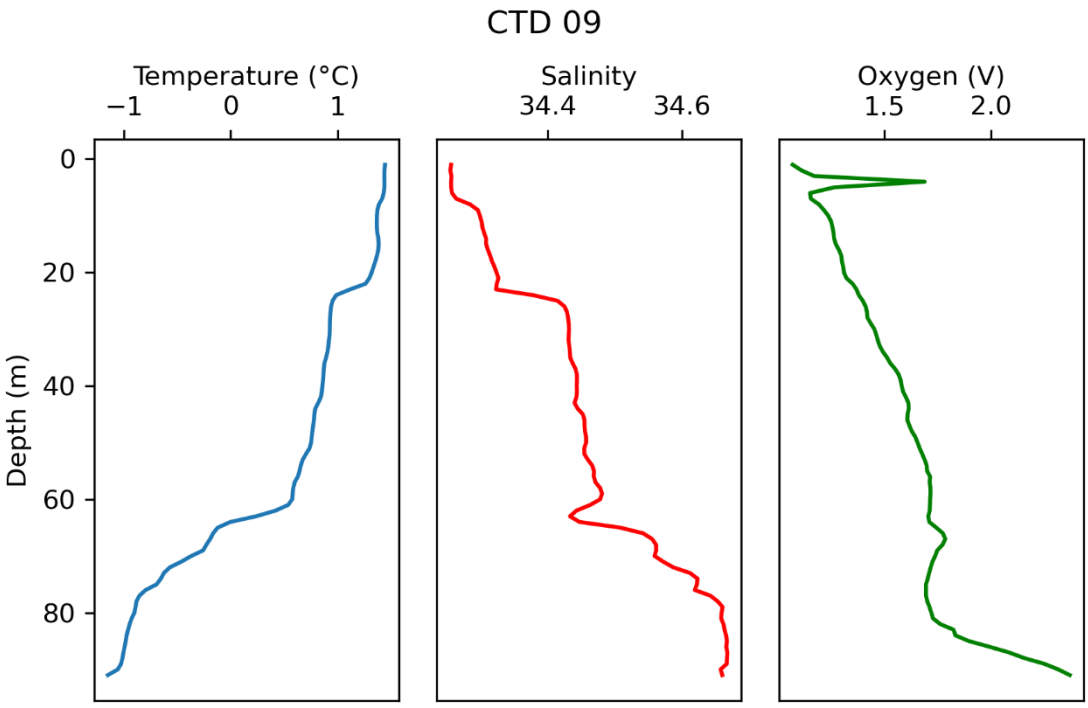

Figure appx2.15. Temperature, salinity and oxygen profiles for the CTD09 (Figure 20 for location).

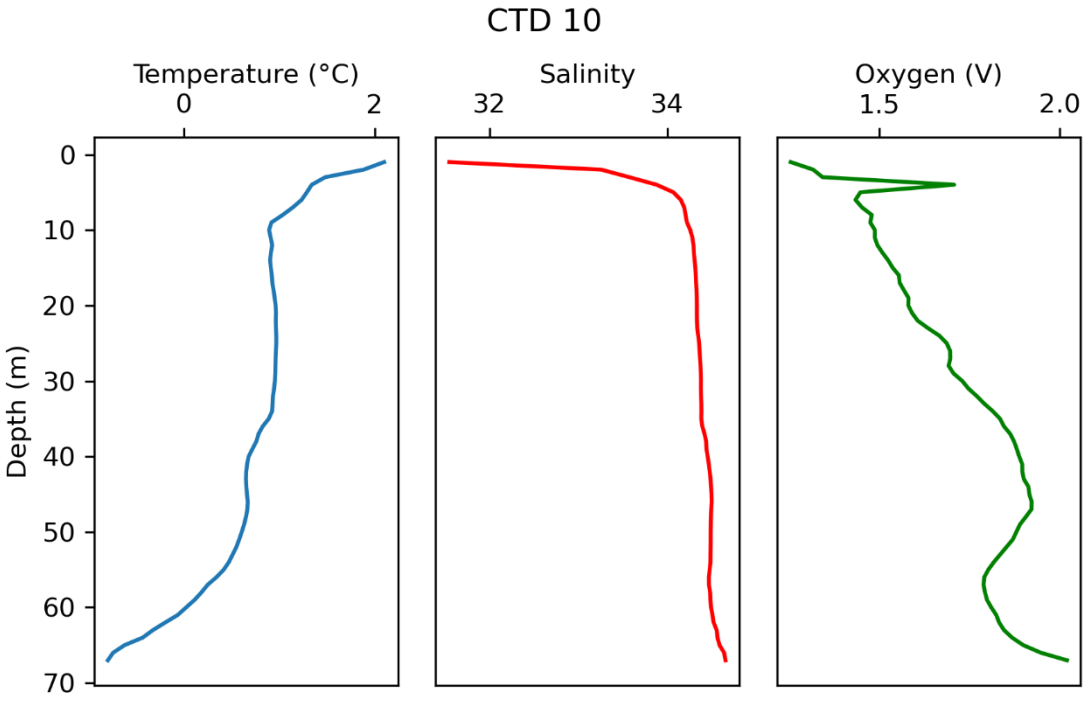

Figure appx2.16. Temperature, salinity and oxygen profiles for the CTD10 (Figure 20 for location).

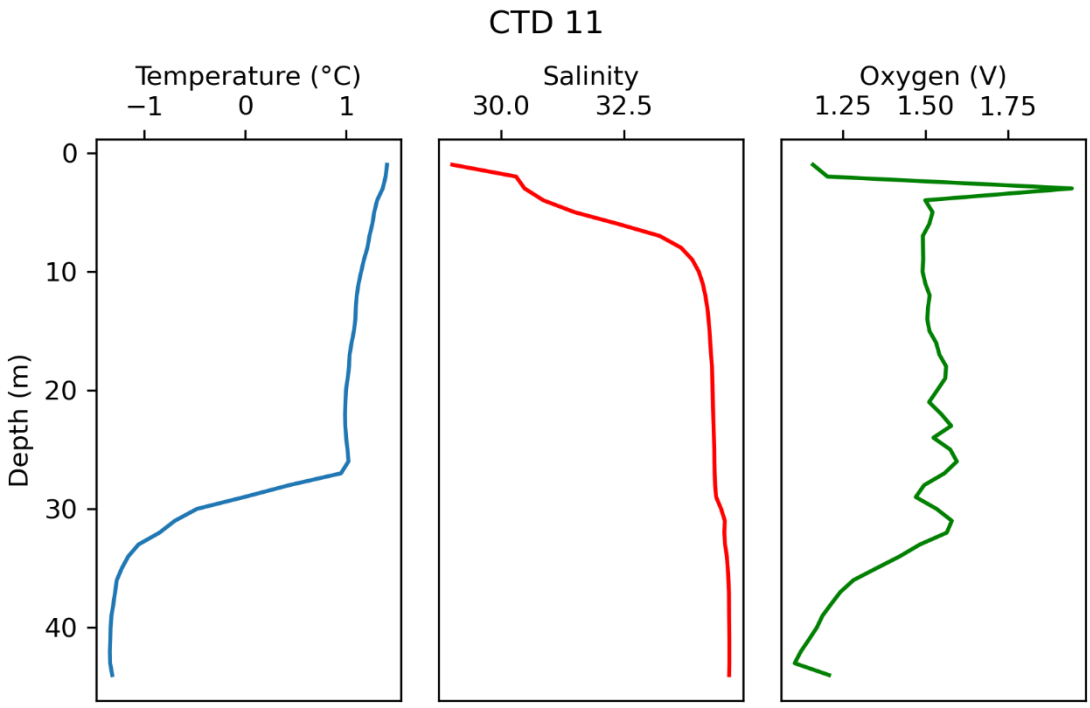

Figure appx2.17. Temperature, salinity and oxygen profiles for the CTD11 (Figure 20 for location).

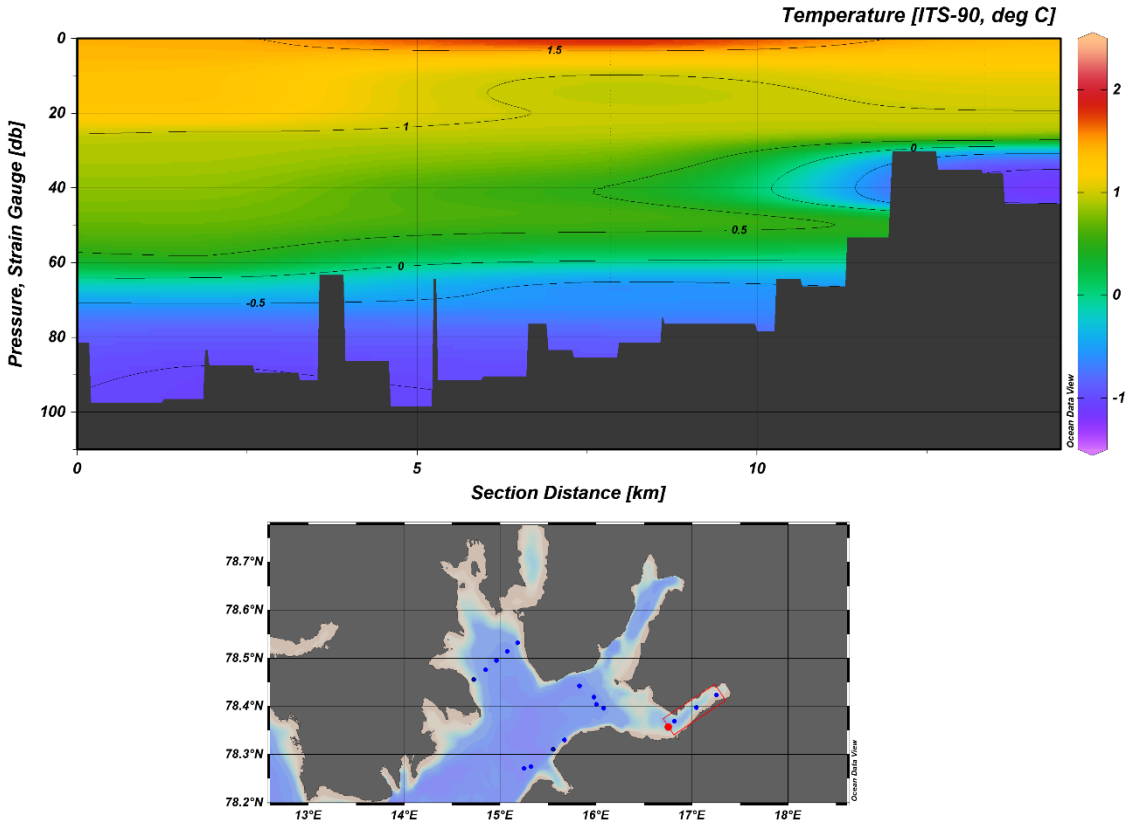

Figure appx2.18. Temperature profile from the transect in Tempelfjorden.

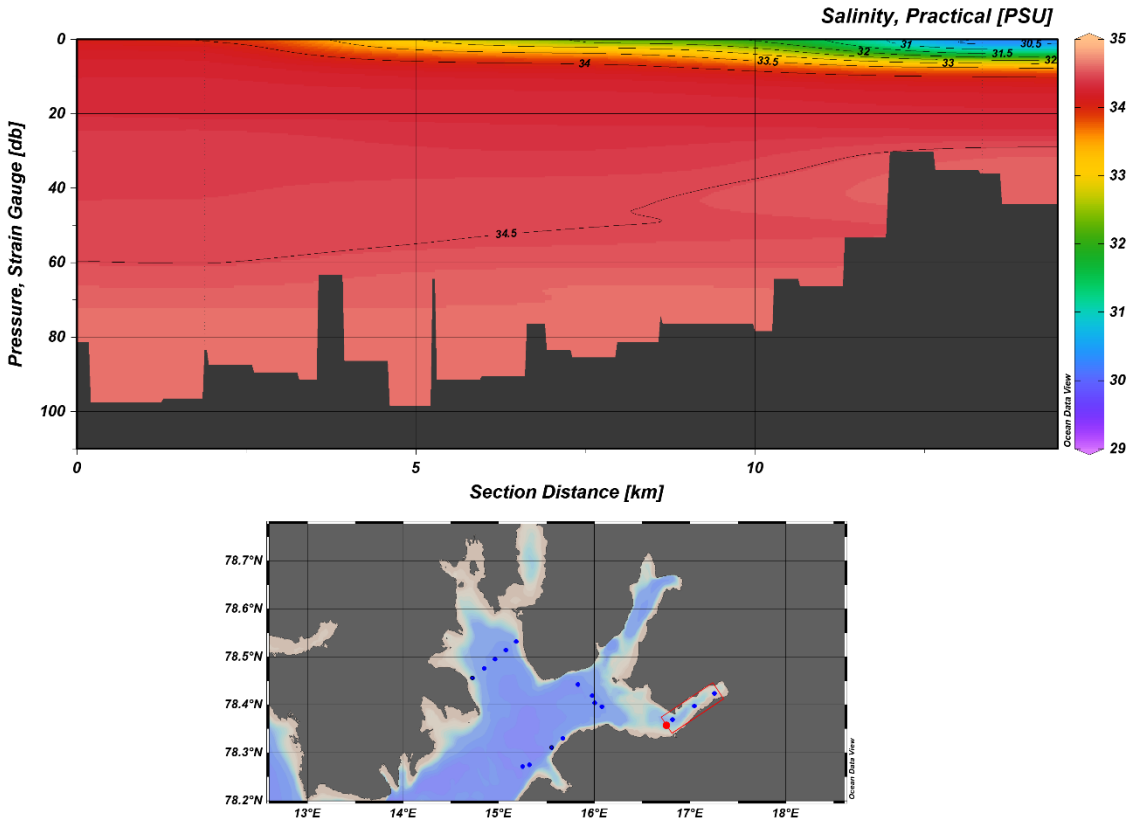

Figure appx2.19. Salinity profile from the transect in Tempelfjorden.

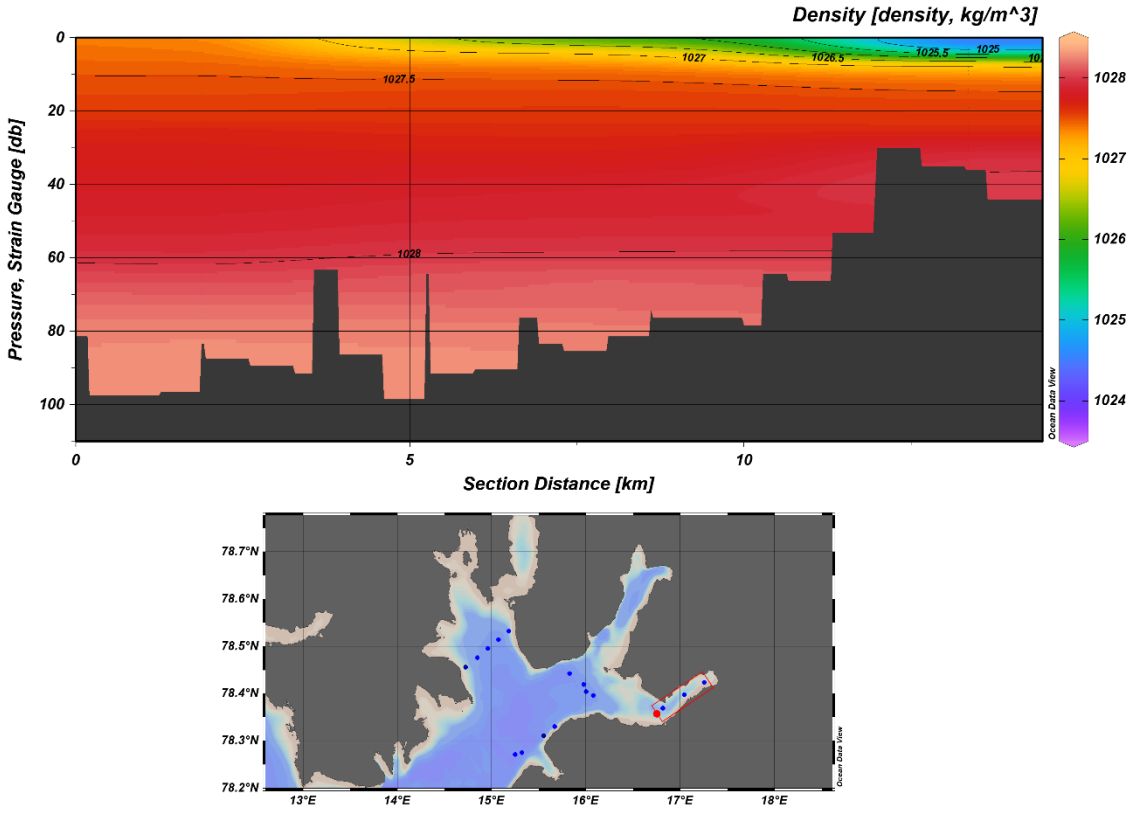

Figure appx2.20. Density profile from the transect in Tempelfjorden.

Nordfjorden

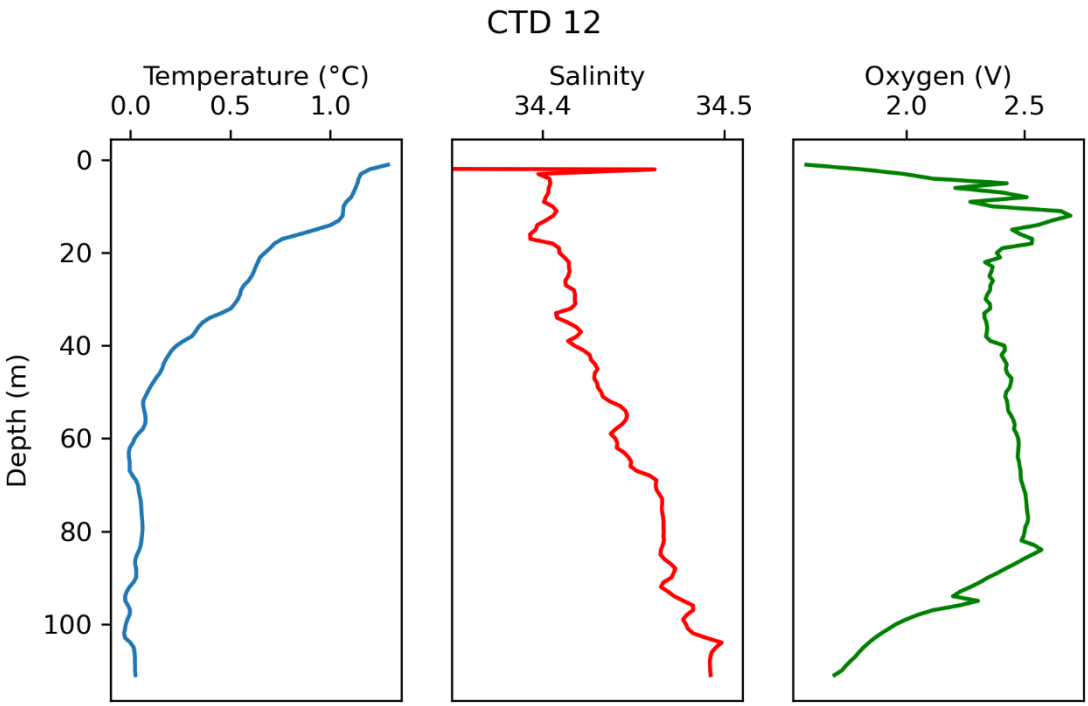

Figure appx2.21. Temperature, salinity and oxygen profiles for the CTD12 (Figure 20 for location).

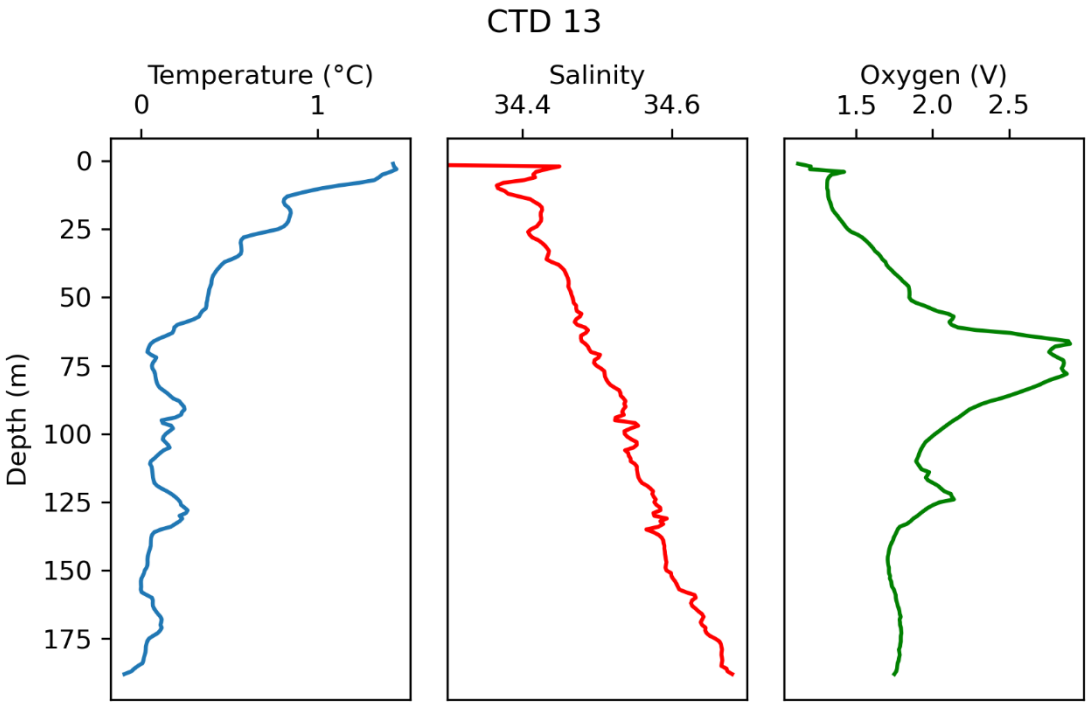

Figure appx2.22. Temperature, salinity and oxygen profiles for the CTD13 (Figure 20 for location).

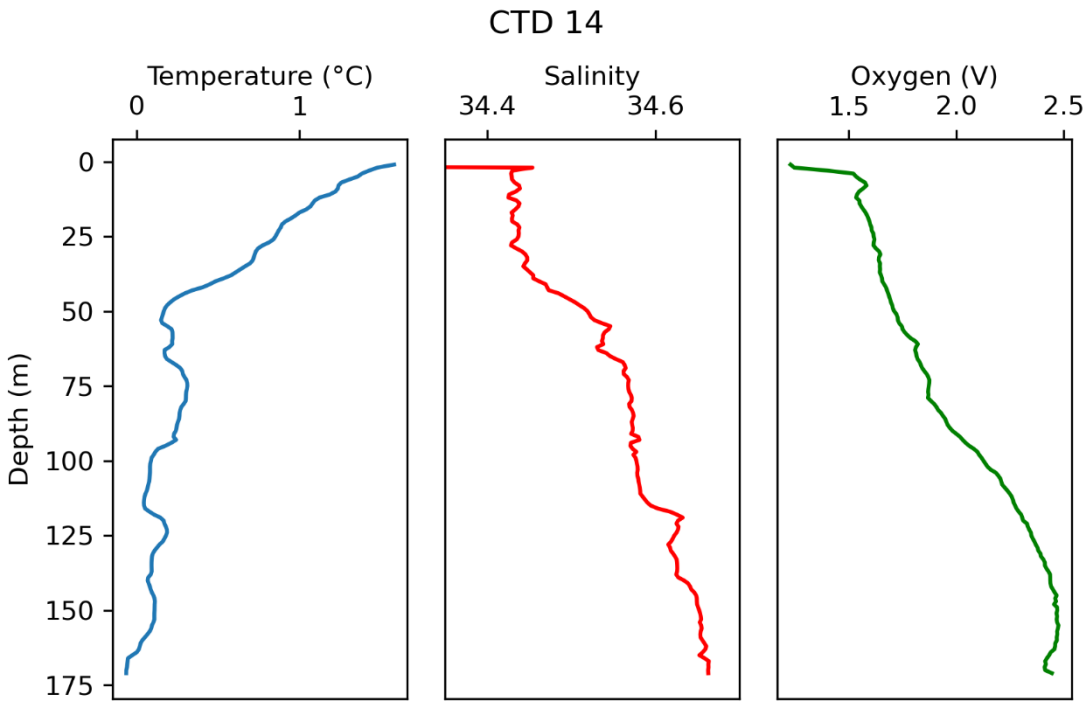

Figure appx2.23. Temperature, salinity and oxygen profiles for the CTD14 (Figure 20 for location).

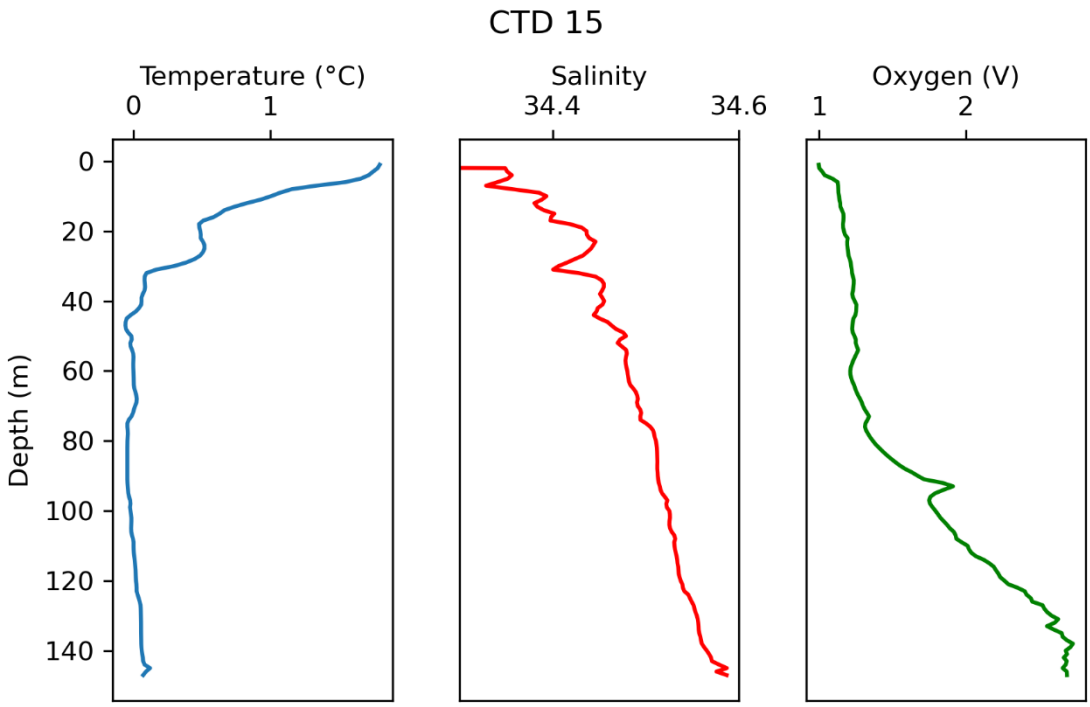

Figure appx2.24. Temperature, salinity and oxygen profiles for the CTD15 (Figure 20 for location).

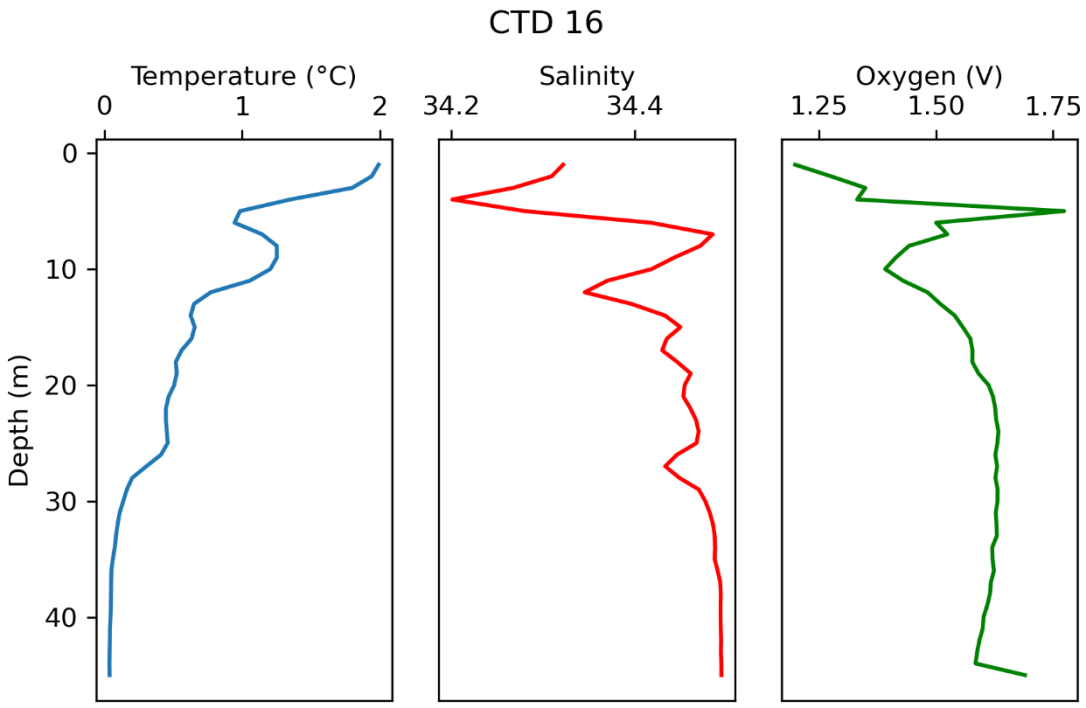

Figure appx2.25. Temperature, salinity and oxygen profiles for the CTD16 (Figure 20 for location).

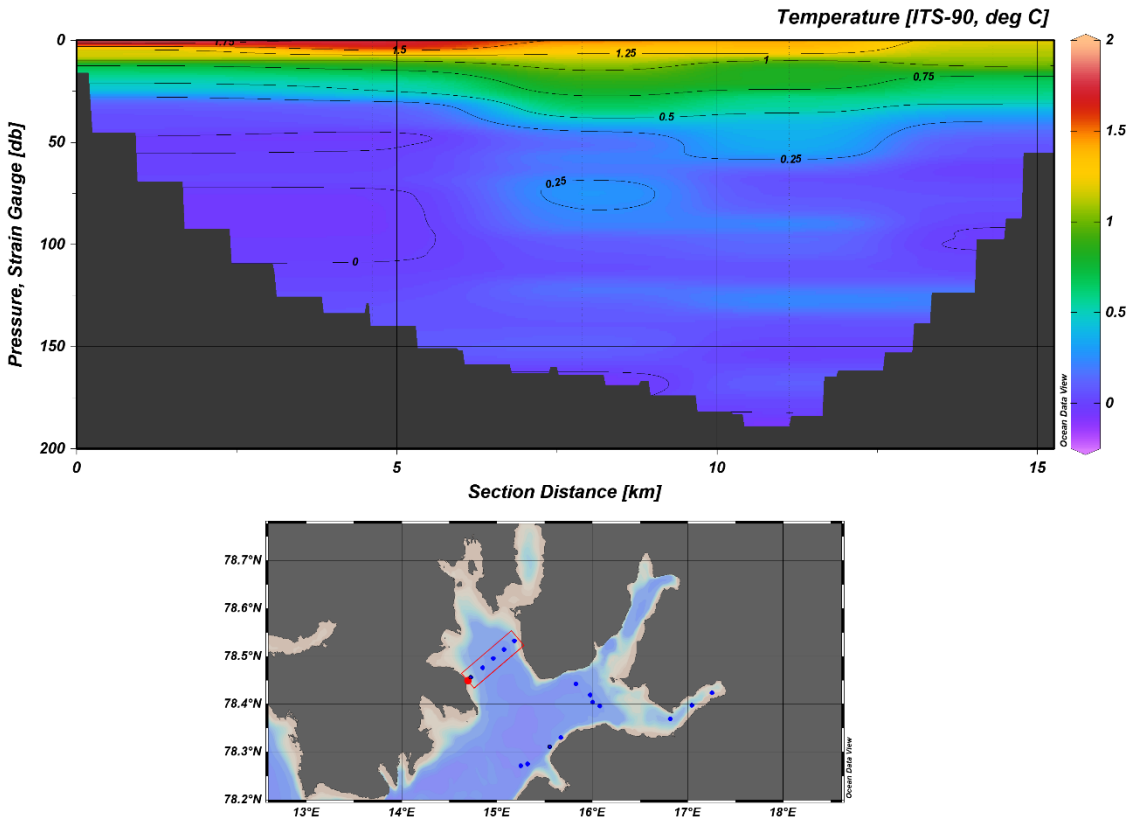

Figure appx2.26. Temperature profile from the transect in Nordfjorden.

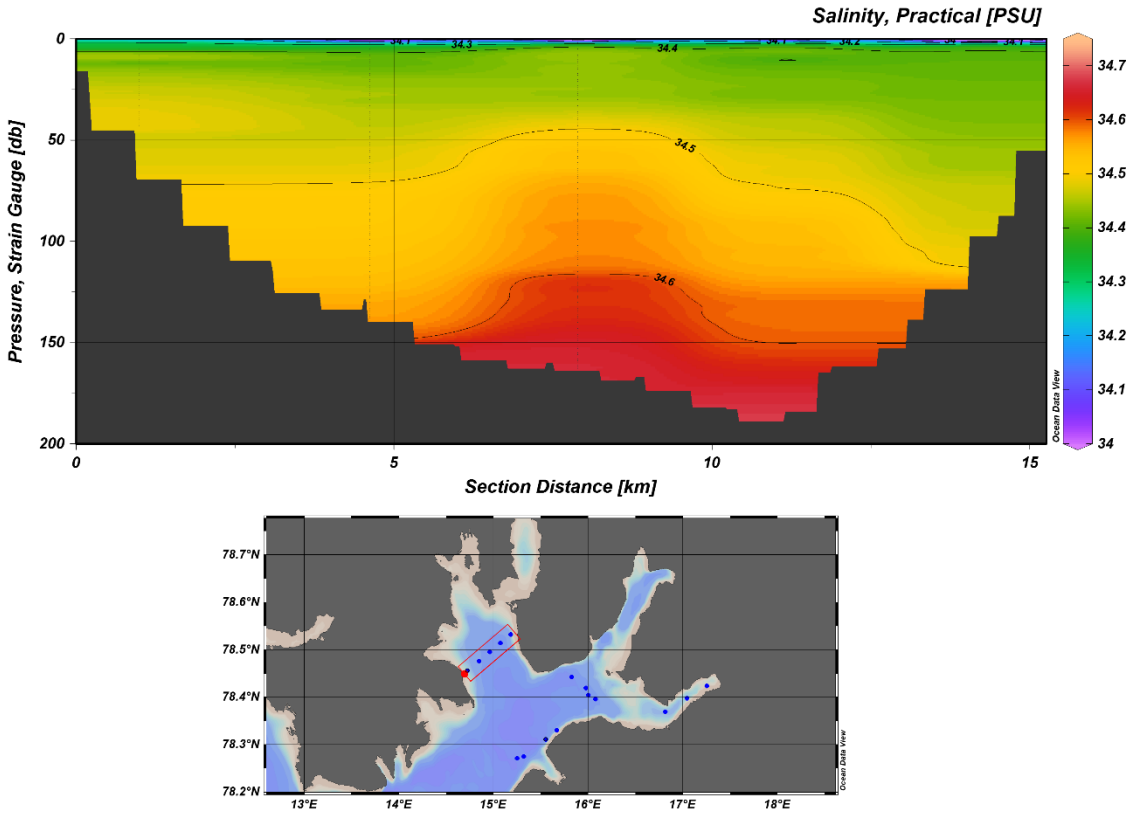

Figure appx2.27. Salinity profile from the transect in Nordfjorden.

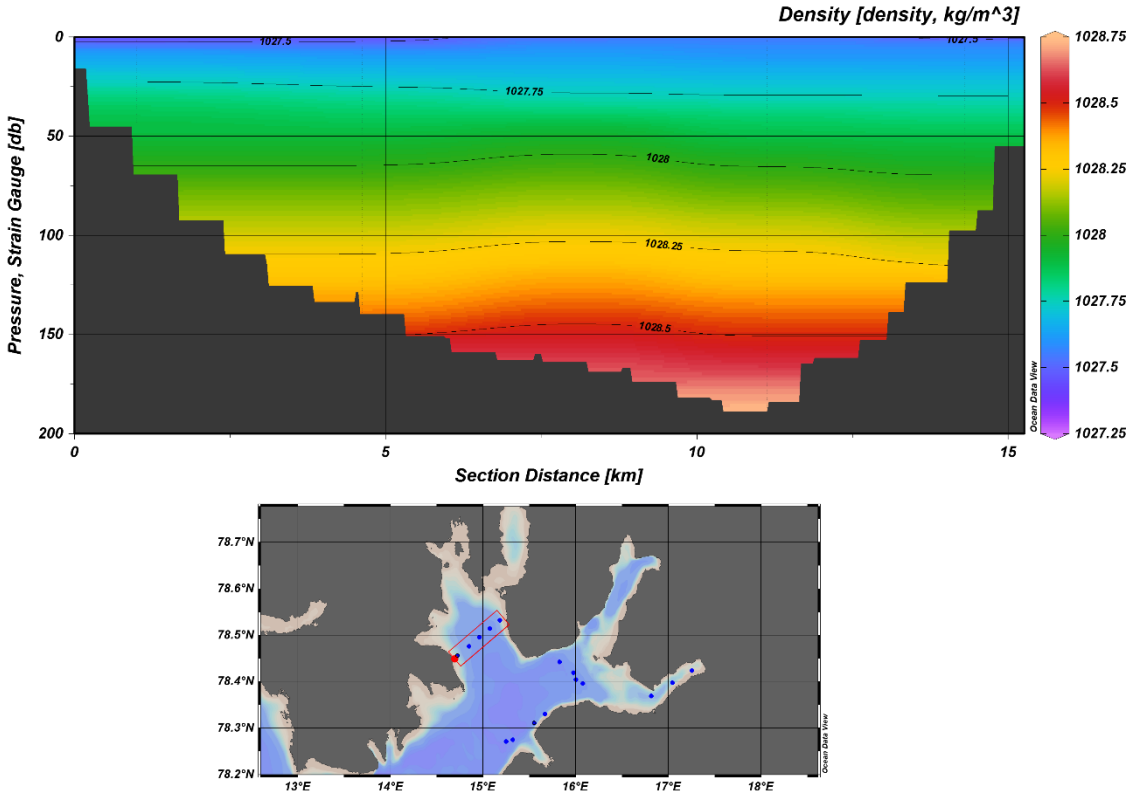

Figure appx2.28. Density profile from the transect in Nordfjorden.

Appendix 3. Python scripts

To perform the geostatistical analysis of the geospatial data, we have used JupyerLab v3.0.14, an open-source web-based user interface for data science.

Import packages

In [2]:
```
import pandas as pd
import geopandas as gpd
import matplotlib.pyplot as plt
import matplotlib.ticker as mticker
import cartopy
import cartopy.crs as ccrs
import shapefile
import csv
import osgeo.ogr, osgeo.osr
import numpy as np
import iris
import iris.iterate
import iris.plot as iplt
from shapely.geometry import Point, MultiPoint, shape, Polygon
from shapely.ops import nearest_points
from shapely import speedups
from shapely.ops import unary_union
from osgeo import ogr
from sys import argv
from sklearn.neighbors import BallTree
from matplotlib import cbook
from pathlib import Path
from cartopy.mpl.gridliner import LONGITUDE_FORMATTER, LATITUDE_FORMATTER
```

Define file path

Depending on the file-type, we will use pandas (pd) or geopandas (gpd) to import the file.

In [4]:
```
# Import CSV file
csv = pd.read_csv(r"Directory:\Folder\FileName.csv", sep ";")

# Import shapefiles
shapefile = gpd.read_file(r"Directory:\Folder\FileName.shp")
```

Coordinate conversion

The data needs to be fully georeferenced using the correct EPSG code in order to perform any geostatistical analysis. Consequently, we made a conversion to UTM 32633 coordinate reference system using the function .to_crs("epsg:32633").

In [ ]:
```
track   gpd.GeoDataFrame(
    track, geometry=gpd.points_from_xy(track.long,track.lat),crs = "epsg:4326")
track   track.to_crs("epsg:32633")
track["x"] = track.geometry.x
track["y"] = track.geometry.y
```

In [ ]:
```
track.to_file(r"Directory:\Folder\FileName.shp")
```

3.1. Nearest neighbour between two point datasets

We have to define a dataset of origin and a dataset of destination. We used the function .distance() and selected the destination point with the minimum distance from each point of origin for the calculation.

In [ ]:
```
# Step 1: Calculate the closest distance from the origin point (e.g. flare) to the end point (e.g

flare["distance"] = flare.geometry.apply(lambda row: min(pockmark.distance(row)))
```

In [ ]:
```
# Step 2: Binning data (e.g. flares) - divide (bin) the data into numeric ranges
```

In [ ]:
```
cut_labels_6 = ["0-2 km", "2-4 km", "4-6 km", "6-8 km" ,"8-10 km", "> 10 km"]
cut_bins    [0, 2000, 4000, 6000, 8000, 10000, 12000]
gdf['cut_ex1'] = pd.cut(gdf["distance"], bins=cut_bins, labels=cut_labels_6)
```

In [ ]:
```
flare["cut_flare"]
flare[(flare["cut_flare"] == "0-2 km")].count().iloc[-1]
```

In [ ]:
```
# Step 3: Calculate the % of data in each bin

stats    flare.groupby(by = "cut_flare").count()
stats["%"] = stats.distance/stats.distance.sum()*100
```

In [ ]:
```
# Step 4: Export in CSV file using the function .to_file()

stats.to_csv(r"Directory:\Folder\FileName.csv", index = False)
```

3.2. Nearest neighbour between a point and a line/polygon

Evaluate the shortest distance between flares and ship track to the coastline to understand their distribution in the fjord. To do so, we have used the union of the two functions .boundary.distance().

In [ ]:
```
# Step 1: Calculate the closest distance from the origin point (e.g. track points) to the line (e

track["distance"] = track.geometry.apply(lambda row: min(coast.boundary.distance(row)))
```

In [ ]:
```
# Repeat Steps 2, 3 and 4 from section 1.1.
```

3.3. Point in Polygon intersection

Calculate the % of flares and ship track that covered the different geological units outcropping in the fjords. I used the function .within() from geopandas to describe the points there are within a polygon.

In [ ]:
```
# Step 1: Define the file characteristics

# The geo_polygon files need to be previously converted to UTM.shp
geo_polygon = [file1, file2, file3, file4, file5, file6]

# Define the label of each polygon group
geo_label = ["Label 1", "Label 2", "Label 3", "Label 4", "Label 5", "Label 6"]
```

In [ ]:

```
def flares_in_polygon(file_points, file_polygon, geo_label, **kwargs):
    if "plot" in kwargs and kwargs["plot"]:
        fig, ax = plt.subplots()
        file_polygon.plot(ax=ax,  facecolor='gray')
        file_points.plot(ax=ax, color='blue', markersize 0.5)
        plt.tight_layout()
    file_points.within(file_polygon)
    speedups.enabled

    if file_points.crs !=file_polygon.crs:
        print("Your files do not have the same CRS, make sure to double check.")
        print(f"file_points crs = {file_points.crs}")
        print(f"file_polygon crs = {file_polygon.crs}")

    # Merge the polygons into a single multipolygon
    one_multipolygon = unary_union(file_polygon.geometry.values)
    one_multipolygon_series = gpd.GeoSeries(one_multipolygon)
    one_multipolygon_dataframe = gpd.GeoDataFrame(geometry    one_multipolygon_series)
    one_multipolygon_dataframe.crs   file_polygon.crs

    pip_mask = file_points.within(one_multipolygon_dataframe.at[0, "geometry"])
    pip_point_polygon = file_points.loc[pip_mask]

    # Create a figure with one subplot
    if "plot1" in kwargs and kwargs["plot1"]:
        fig, ax = plt.subplots()
        file_polygon.plot(ax=ax, facecolor='lightblue')
        pip_point_polygon.plot(ax=ax, color='gold', markersize=2)
        plt.tight_layout()

    # Add a column with classification
    if not hasattr(gdf,"geology"):
        file_points["geology"] = np.nan
    file_points.loc[pip_point_polygon.index.values,"geology"]  =  geo_label
    #finalresult = file_points[file_points.geology==(geo_label)]
    return file_points
```

In [ ]:

```
# Creating a loop has accelerated the calculation of the data

for i in range(len(geo_polygon)):
    gdf = flares_in_polygon(gdf, geo_polygon[i], geo_label[i], plot = True, plot1    True)
```

In [ ]:

```
gdf.geology.drop_duplicates()
```

In [ ]:

```
# Step 2: Create a new column with the % of points in each bin

groups = gdf.groupby("geology").count()
groups["%"] = groups.geometry/groups.geometry.sum()*100
```

In [ ]:

```
# Step 3: Export the file in CSV

groups.to_csv(r"Directory:\Folder\FileName.csv", index = True)
```

3.4. Data normalization and statistical calculations

3.4.1. Data normalization

Normalization of the flares with respect to the ship track and distance to the geological units.

In [ ]:

```
shiptrack["%"]
```

In [ ]:
```
normtrack = shiptrack["%"]/100
```

In [ ]:
```
flares["normalize"] = (flares["depth(m)"])/normtrack
```

In [ ]:
```
flares["normalize(%)"]  =  (flares["normalize"]/flares["normalize"].sum())*100
```

In [ ]:
```
# Export the file in CSV

flares.to_csv(r"Directory:\Folder\FileName.csv", index = True)
```

3.4.2. Statistical calculations

In [ ]:
```
# Furthest distance
np.max(flares["distance"])

# Closest closest distance
min(flares["distance"])

# Mean distance
np.mean(flares["distance"])

# Median distance
np.median(flares["distance"])

# Lower quartile caulculation
np.percentile(flares["distance"], 25)

# Higher quartile calculation
np.percentile(flares["distance"], 75)
```

3.5. Link coordinates with timestamp

The scripts below merge the track locations with the measurements of the methane analyzer.

In [ ]:
```
# Step 1: Change timezones and adding timestamp as the index

meth01["datetime"] = pd.to_datetime(meth01.SysTime, format    "%d/%m/%Y %H:%M:%S.%f", utc=True)

# Time in Longyearbyen time (-2 hours respect to UTC)
utc = pd.tseries.offsets.DateOffset(hours=-2) # this step transforms time to UTC from Europe/Oslo

# +2.49 min delay from the machine
timestamp_error  =  pd.tseries.offsets.DateOffset(minutes=-2,seconds=-49)

# -54 sec delay from the 25 m tube
fluidflow_delay = pd.tseries.offsets.DateOffset(seconds=-54)

meth01.datetime = meth01.datetime + utc + timestamp_error + fluidflow_delay

#The resulting time is in UTC
```

In [ ]:
```
# Step 2: Replace the initial index with the datetime stamp and drop NaN values

meth01.set_index("datetime", inplace=True)
meth01.dropna(inplace=True)
meth01
```

In [ ]:
```
test = meth01.copy() # Creates a time-offset dataframe and appends it to the original one
test.index = test.index + pd.tseries.offsets.DateOffset(days=5)
meth01 = meth01.append(test)
```

In [ ]:
```
# Step 3: Plot the methane data for a specified datetime interval

start   "2021-06-01 00:56:02.000"
stop = "2021-06-01 23:59:02.000"
meth01.loc[start:stop].plot(y="[CO2]_ppm")

#or, similarly:

meth01.loc["2021-06-01  00:56:02.000":"2021-06-01  23:59:02.000"].plot(y="[CO2]_ppm")
```

In [ ]:
```
#Step 4: Convert string column to datetime in track

track["datetime"] = pd.to_datetime(track["DateTimeS"], format = "%Y-%m-%dT%H:%M:%S.%f")

track["datetime"] = track.datetime.round("s")
track   track.drop_duplicates(subset="datetime", keep="first")
track.set_index("datetime", inplace True)
track   track.resample(f"1S").bfill(limit=1)
track.x = track.x.interpolate()
track.y = track.y.interpolate()
track.geometry = [Point(xy) for xy in zip(track.x,track.y)]
```

The following code down below rounds all track and methane measurement times to the second interval; this allows to compare them based on their timestamps.

In [ ]:
```
#Step 5: Round track and methane index datetimes to the second

meth01.index = meth01.index.round(freq="s")
```

In [ ]:
```
# Step 6: Plot all track points that have a corresponding timestamp in the meth01 index

track.loc[track.index.isin(meth01.index)].plot()
```

In [ ]:
```
meth01["geometry"]  =  track.loc[track.index.isin(meth01.index)].geometry.values
```

In [ ]:
```
for nr, i in enumerate(p.glob("**/*")):
    air = pd.read_csv(str(i),skiprows=1,skipinitialspace True)

    air["datetime"] = pd.to_datetime(air.SysTime, format = "%d/%m/%Y %H:%M:%S.%f", utc=True)
    utc = pd.tseries.offsets.DateOffset(hours=-2) # this step transforms time to UTC from Europe/
    timestamp_error = pd.tseries.offsets.DateOffset(minutes  2,seconds=-49)
    fluidflow_delay = pd.tseries.offsets.DateOffset(seconds 54)
    air.datetime = air.datetime + utc + timestamp_error + fluidflow_delay
    air.datetime = air.datetime.round("1s")
    air = air.drop_duplicates(subset="datetime")
    air.set_index("datetime", inplace=True)
    air.dropna(inplace=True)
    #print(air.head())
    if nr != 0:
        allair = allair.append(air)
        print(i, nr, len(air))
        del air
    else:
        allair = air.copy()
        print(i, nr, len(air))
        del air

allair = allair.drop_duplicates()
```

In [ ]:

```
allair = allair.loc[track.index.min():track.index.max()]
allair["geometry"] = track.loc[track.index.isin(allair.index)].geometry.values
allair_gdf = gpd.GeoDataFrame(
    allair, geometry=allair.geometry,crs = "epsg:32633")
allair_gdf["x"] = allair_gdf.geometry.x
allair_gdf["y"] = allair_gdf.geometry.y
allair_gdf.plot(kind="scatter",x "x", y="y",c="[CO2]_ppm")
```

In [ ]:

```
allair_gdf.plot(kind="scatter",x "x", y="y",c="[CO2]_ppm", vmin = 380, vmax=500)
```

In [ ]:

```
# Step 7: Plot the data using Cartopy

fig = plt.figure(figsize=(10,5))
#ax.stock_img()
ax = plt.axes(projection=ccrs.epsg(32633))
ax.coastlines(resolution="10m")
ax.set_title("Air CH4 concentration")

#ax.set_extent([14.5, 17.3, 78.2, 78.65], ccrs.Geodetic())

## Plot of the dataset
allair_gdf.plot(ax=ax,
                kind="scatter",
                x="x", y="y",c="[CH4]_ppm",
                #vmin = 400, vmax=500, #for CO2_ppm
                vmin = 1.935, vmax= 2, #for CH4_ppm
                cmap='OrRd')

## Plot map
gl = ax.gridlines(draw_labels = True,
                  dms = True,
                  x_inline=False, y_inline= False,
                  color= "gray", linewidth= 0.5)
gl.xlabels_top = False
gl.xlabels_bottom = True
gl.ylabels_left = True
gl.ylabels_right = False
gl.xlocator = mticker.FixedLocator([14, 15, 16, 17])
gl.ylocator = mticker.FixedLocator([78.2, 78.3, 78.4, 78.5, 78.6])
gl.xformatter = LONGITUDE_FORMATTER
gl.yformatter = LATITUDE_FORMATTER
gl.xlabel_style = {"size": 11, "color": "black"}
gl.ylabel_style = {"size": 11, "color": "black"}
gl.xaxis.set_major_formatter(cartopy.mpl.ticker.LongitudeFormatter([14, 15, 16, 17])
gl.yaxis.set_major_formatter(cartopy.mpl.ticker.LatitudeFormatter([78.3, 78.4, 78.5])

plt.tight_layout()

plt.savefig(r"Directory:\Folder\FigureName.png",  dpi=300)

plt.show()
```

3.6. Plots

3.6.1. Bar charts

In [ ]:

```
# Plot data - E.g. comparison of faults and normalized within geo units

barWidth   0.25

geoarea = geology["%"]
faults = normfaults["%"]
normfaults = normfaults["normalize(%)"]

# Set position of bar on X axis
br1 = np.arange(len(geoarea))
br2 = [x + barWidth for x in br1]
br3 = [x + barWidth for x in br2]

# Make the plot
plt.bar(br1, geoarea, color ='dimgrey', width = barWidth,
        edgecolor ='grey', label ='Outcrop area')
plt.bar(br2, faults, color ='firebrick', width = barWidth,
        edgecolor ='grey', label ='Faults')
plt.bar(br3, normfaults, color ='darkred', width = barWidth,
        edgecolor ='grey', label ='Normalized faults')

# Adding Xticks
plt.xlabel('Geological units')#, fontweight ='bold', fontsize = 11)
plt.ylabel('Percentage (%)')#, fontweight ='bold', fontsize = 11)
plt.xticks([r + barWidth for r in range(len(geoarea))],
        ["VM Gr.", "A Gr.", "J S.Gr.", "Ag Fm.", "KT Gr.", "B Fm.", "S Gr.", "T Gr.", "G Gr."])

plt.suptitle('Distribution of faults within the geological units - Isfjorden')
plt.size=(20,40)
plt.legend(loc='upper right')
plt.grid(axis='y')
plt.tight_layout()

plt.savefig(r"Directory:\Folder\FigureName.png", dpi=300)

plt.show()
```

3.6.2. CTD stations

In [ ]:

```
# Step 1: Create variables with user-friendly names

depth   data[:,2]
temp    data[:,3]
salt    data[:,6]
oxygen  = data[:,5]
del()
```

In [ ]:

```
# Step 2: Three-panel plot

fig2, (ax2, ax3, ax4) = plt.subplots(1,3,sharey=True)
#fig2.size=(20, 40)
fig2.suptitle('CTD 15', size=12, y=0.95)
# Temperature
ax2.plot(temp,depth)
ax2.set_ylabel('Depth (m)')
ax2.set_ylim(ax2.get_ylim()[::-1]) #this reverses the yaxis (i.e. deep at the bottom)
ax2.set_xlabel('Temperature (°C)')
ax2.xaxis.set_label_position('top')
ax2.xaxis.set_ticks_position('top')
ax2.set_xticks([-0.5, 0, 0.5])
ax2.set_xticklabels(["-0.5", "0", "0.5"])
#ax2.set_xticklabels(xtl)
# Salinity
ax3.plot(salt,depth,'r')
ax3.set_xlabel('Salinity')
ax3.xaxis.set_label_position('top')
ax3.xaxis.set_ticks_position('top')
ax3.set_xlim(34.3, 34.6)
ax3.set_xticks([34.4, 34.5, 34.6])
ax3.set_xtickslabels([34.25, 34.5, 34.75])
ax3.yaxis.set_visible(False) # This erases the y ticks
# Fluorescence
ax4.plot(oxygen,depth, 'g')
ax4.set_xlabel('Oxygen (V)')
ax4.xaxis.set_label_position('top')
ax4.xaxis.set_ticks_position('top')
ax4.set_xticks([0, 1, 2, 3, 4, 5])
ax4.yaxis.set_visible(False) # This erases the y ticks

plt.tight_layout()


plt.savefig(r"Directory:\Folder\FigureName.png",  dpi=300)
```

Statement on the thesis' originality

Herewith I, Nil Rodés i Llorens, declare that I wrote the thesis independently and did not use any other resources than those named in the bibliography, and, in particular, did not use any internet resources except for those named in the bibliography. The master thesis has not been used previously as part of an examination. The master thesis has not been previously published.

Bremen, 3rd of September 2021.